VO_2ナノ構造体創製による
ナノ巨大物性発現とその電気的制御

平成２６年６月

髙見　英史

VO_2ナノ構造体創製による
ナノ巨大物性発現とその電気的制御

博士（工学）論文提出先

大阪大学大学院基礎工学研究科

平成２６年６月

髙見　英史

Abstract

3d transition metal oxides show huge phase transition phenomena originating from the strong electron-electron interaction. These non-linear phenomena have been extensively studied due to their high potential for functional materials and devices which are superior to that of conventional semiconductors. Vanadium dioxide (VO_2) is the typical oxide materials because it shows huge metal-insulator transition (MIT) around room temperature. VO_2 has spatially inhomogeneous electronic states consisting of metallic phase and insulating one in a nanoscale, so that it is expected that the unusually huge and steep MIT occurs when the size of the VO_2 decreases to that of single electronic domain. Moreover, the novel interface function between nanoscale single electronic domains can be also expected in VO_2 nanostructures.

The purpose of this thesis is to realize huge phase transition phenomena originating from the physical properties of single electronic domain and electrical control of the non-linear phenomena towards the novel electronic devices by fabricating VO_2 nanostructures.

My achievements are as follows:

(1) I developed oxide nanofabrication process by using nanoimprint lithography as a next generation nanofabrication technique and succeeded in mass production of VO_2 nanowires with 30 nm width at minimum in $3\times3mm^2$ on the substrates, which facilitated the investigation into physical properties with wide range of size from micro to nano-scale and application to nanodevices.

(2) I observed multi-step MIT with resistivity change around 10^5 %/K by realizing one-dimensional alignment of electronic domain in VO_2 nanostructures. Moreover, I clarified that the large resistivity change originates from the MIT of single electronic domain by performing numerical simulation and demonstrated superiority of nanodevices to thin-film-based devices in energy consumption.

(3) In the one-dimensionally aligned electronic domain as mentioned above, I noticed Peltier cooling effect at the interface of electronic domain can be utilized. And actually, I realized electric switch from high temperature metallic phase to low temperature insulating one, which have seen as an impossible function for two terminal devices and demonstrated write-and-erase operation as a non-volatile memory devices in two-terminal devices for the first time.

CONTENTS

CHAPTER 1

General introduction

1.1 Scope of this study

3d transition metal oxides with strongly correlated electron system exhibit rich varieties of functionalities, such as superconductivity in cuprates [1], giant magneto resistance in manganites [2], or metal-insulator transition in vanadates [3]. These non-liner phenomena originating from the strong electron-electron or electron-phonon coupling will offer major breakthrough in materials science and engineering. For example, in conventional semiconductors, the device performance has been enhanced by decreasing the device size, but this enhancement encounters the limitation due to the leakage current which decreases the On/Off ratio[4]. However oxide materials as mentioned above have a full potential to realize the high On/Off ratio due to the above mentioned non-linear phenomena.

With the development of scanning probe microscopy technique, it was revealed that the strongly correlated oxide materials show spatially inhomogeneous electronic phase in the vicinity of their phase transition points.[5-7] The phase separation makes it difficult to utilize the full potential of the materials because the changes of their physical properties are averaged over the materials, which is a major obstacle to control their physical properties and to understand the mechanism of the phase transition itself.

The phase separations were observed not only in the thin film but also in the single crystal, thus the origin of the phase separation is not simply explained by the structural imperfection or the fluctuation of chemical composition, which indicate the important role of strong electron correlation in the transition metal oxides[8]. To investigate and control the physical properties of the phase-separated oxide materials, many researchers have been trying to accessing the single domain by fabricating the oxide nanostructures. Because the individual domain's behavior can be electrically manipulated and captured as multistep change of physical properties when the total number of domain in the nanostructure decreases.[9, 10]

Vanadium dioxide is one of the typical materials which shows a spatially inhomogeneous electronic states which consist of metallic and insulating domain at around its metal-insulator transition (MIT) temperature, 340 K.[7, 11] The drastic change of the physical properties at around room temperature makes the material very

attracting for technological application such as Mott FETs [12], memristors [13], and racetrack memories [14]. After Park *et al.* succeeded to synthesize VO_2 single crystal micro- or nano-beams using the vapor transport method,[15] investigation of single domain's behavior of VO_2 have been extensively reported.[16] However, the bottom-up method utilized to fabricate the VO_2 nanostructure have disadvantage for the application to next generation nanodevices, because the size, shape, position and growth direction of the nanobeams are difficult to control.[15] On the other hand, thin-film-based top-down methods such as photolithography, electron beam lithography, nanoimprint lithography are promising for device application and systematic investigation for size-effect of single domain's behavior. Among the lithography techniques, nanoimprint lithography has advantage in the controllability of the size and shape in a large area, which is suitable for systematic study and mass production of the nanodevices.[17]

The purpose of this thesis is to realize huge MIT by detecting single domain's behavior in confined nanospace and electrically control the huge MIT. To clarify the single domain's behavior, I fabricated VO_2 nanostructures by using nanoimprint lithography. The contents of the thesis are as follows. Chapter 2 briefly described experimental method employed in my work including pulsed laser deposition technique and nanoimprit technique. Chapter 3 describes the detailed fabrication condition and process for VO_2 nanostructures and investigation into relationship between domain geometry and transport properties by performing optical observation and electric measurement at same time. Chapter 4 discusses multistep metal-insulator transition observed in VO_2 nanostructure on Al_2O_3 (0001) single crystal substrates. Nearly two orders of magnitude change of resistivity was realized by extracting the MIT of a nano-scaled single domain. To confirm the origin of the observed large transition and the relationship between domain configuration and resistivity as a function of temperature, I performed numerical calculation based on a random resistor network model. Chapter 5 introduces my theoretical model to control the single domain's MIT by using local thermoelectric effect at metal and insulator domain boundary. This idea is experimenttaly realized as an electrical control of non-volatile and reversible MIT in VO_2 nanowires on Al_2O_3 (0001) substrates. The electrical control of reversible metal-to-insulator transition in VO_2 two-terminal devices was demonstrated for the first

time, which was achieved by using the Peltier effect at a domain's interface. Finally, Chapter 6 summarized these investigation from the view point of the electric control of MIT by manipulating the single domain's behavior in the VO_2 nanostructure.

1.2 Fundamental physical properties of vanadium dioxide

VO_2 undergoes first-order metal-insulator transition (MIT) at 340 K in atmospheric pressure [3]. Above the MIT temperature (T_{MI}), VO_2 takes metallic state with rutile crystal structure (R phase) while below the T_{MI}, it takes insulating state with monoclinic crystal structure (M1 phase) as shown in Fig. 1.1. During the transition, the drastic change in electrical [18], optical [19], mechanical [20], magnetic [21] and thermal [22] properties occur. In particular, the difference of electrical resistivity between metallic (R_M) and insulating (R_I) phase is reported to be $R_I / R_M = 10^5$ for single crystal [23] and $R_I / R_M = 10^3$-10^4 for typical thin films [24], where ΔR is the difference of the resistivity between the one in a metal region and the one in an insulator region. From the technological point of view, the drastic change of physical properties are attractive for possible application to electronic switching and data storage devices.

At low temperature in the M1 state, two V^{4+} ions forms a dimer and tilt along the c-axis of rutile phase with energy gap around 0.6 eV near the Fermi level.[25] Pouget *et al.* reported insulating M2 phase in which half of the vanadium ions are not dimerized but equally spaced along the c-axis of rutile phase.[21] From the view point of the single particle band theory, the M2 phase should be metal, then the existence of insulating M2 phase suggests the importance of electron-electron interaction.[7, 26]

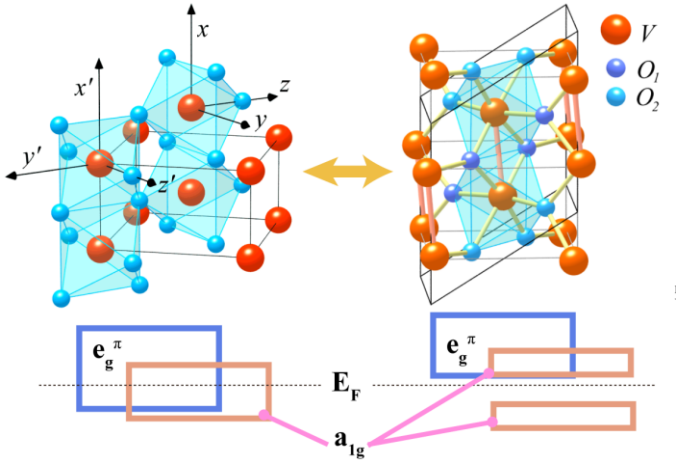

Fig 1.1 Crystal structures and corresponding energy level of VO_2 in the metallic (left) and insulating (right) phases. V-V dimers in the insulating phase are expressed by orange chains between vanadium ions.[27]

In 1967, Mitsuishi *et al*. revealed that VO_2 single crystals show mixed electronic phases consisting of metallic and insulating domain in the vicinity of the T_{MI} by using optical microscope.[28] Typical size of the domain was several or several tens of micrometers and the shape was triangle, square or parallegram with the interface inclined with respect to the crystal axis.[29] In the electric transport properties of VO_2 with the domain structure, discrete resistivity jump was observed, which suggest the important role of the domain's behavior in the electrical properties.[30, 31] However, systematic investigation into the role of domain was difficult because domain's shape, size and distribution are random and uncontrollable. To investigate the single domain's behavior Wu *et al.* synthesized single-crystal nanobeams using vapor transport method with a rectangular cross section originating from the preferential growth of VO_2 along c-axis of rutile phase.[15] Small size and a well-defined morphology of the nanobeams leads to uniaxial strain along the nanobeams, which form periodical structure consisting of metal and insulator domains with one-dimensional configuration. These nanoscale samples made it possible to explore the single domain's behavior in the electric transport properties.[16]

With the development of scanning probe microscopy technique, smaller electric domain was revealed in the VO_2 thin film samples fabricated on the oxide single crystal substrate by using sputtering [11], sol-gel [31], or pulsed laser deposition technique [7]. Kim *et al.* captured the nanoscale image of VO_2 surface during the MIT by using conductive atomic force microsopy technique, and found the domain has strong correlation with the location of the structural grain.[11] On the other hand, Qazilbash *et al.* combined structural and electronic nanoscale imaging of VO_2 by using near-field infrared microscopy and scanning x-ray nanoscale diffraction, and found the difference between the two image at same condition, which imply the origin of the domain cannot be fully attributed to the structural grain or defect. In the electric transport properties, multi-resistive states were observed when the sample size is reduced to micrometer scale, which was entirely different from the smooth transport curves measured in the bulk sample. Sharoni *et al.* reported thermally induced multistep MIT and these discrete transition behavior were captured as a percolation model. These multi-resistive states were also obtained by voltage or current sweep in the hysteresis region [33], which is

applicable to multitistates momory devices like memristors.[33] However, the resistivity change is still small considering the original resistivity change of VO_2 itself, thus fabricating narrower nanostructures are necessary to obtain larger On/Off ratio and high controllability of single domain's MIT.

1.3 References

[1] J. G. Bednorz, K. A. Muller, *Z. Phys. B* **64** (1986) 189

[2] Y. Tokura *et al.*, *J. Phys. Soc. Jpn.* **63** (1994) 3931

[3] F. J. Morin, *Phys. Rev. Lett.* **3** (1959) 34

[4] *The International Technology Roadmap for Semicunductor* (2012).

[5] L. W. Martin, Y. H. Chu, R. Ramesh, *Mater. Sce. Eng. R.* **68** (2010) 89

[6] E. Dagotto, *Science* **309** (2005) 257

[7] M. M. Qazilbash *et al.*, *Science* **318** (2007) 1750

[8] M. Fath *et al.*, *Science* **285** (1999) 1540

[9] Y. Yanagisawa, H. Tanaka, T. Kawai, L. Pellegrino, *Appl. Phys. Lett.* **89** (2006) 253121

[10] A. Sharoni, J. Ramírez, I. Schuller, *Phys. Rev. Lett.* **101** (2008) 026404

[11] J. Kim, C. Ko, A. Frenzel, S. Ramanathan, J. E. Hoffman, *Appl. Phys. Lett.* **96** (2010) 213106

[12] H. T. Kim *et al.*, *New J. Phys.* **6** (2004) 52

[13] S. H. Bae *et al.*, *Adv. Mater.* **25** (2013) 5098

[14] S. S. Parkin, M. Hayashi, L. Thomas, *Science* **320** (2008) 190

[15] J. Q. Wu *et al.*, *Nano Lett.* **6** (2006) 2313

[16] J. Wei, Z. H. Wang, W. Chen, D. H. Cobden, *Nat. Nanotechnol.* **4** (2009) 420

[17] S. Y. Chou, P. R. Krauss, P. J. Renstrom, *J. Vac. Sci. Technol. B* **14** (1996) 4129

[18] L. A. Ladd, W. Paul, *Solid State Commun.* **7** (1969) 425

[19] H. W. Verleur, A. S. Barker, C. N. Berglund, *Phys. Rev.* **172** (1968) 788

[20] N. Sepulveda, A. Rua, R. Cabrera, F. Fernandez, *Appl. Phys. Lett.* **92** (2008) 191913

[21] J. P. Pouget *et al.*, *Phys. Rev. B* **10** (1974) 1801

[22] C. N. Berglund, H. J. Guggenheim, *Phys. Rev.* **185** (1969) 1022

[23] Macchesn.Jb, Guggenhe.Hj, *J. Phys. Chem. Solids* **30** (1969) 225

[24] J. F. Denatale, P. J. Hood, A. B. Harker, *J. Appl. Phys.* **66** (1989) 5844

[25] J. B. Goodenough, *J. Solid State Chem.* **3** (1971) 490

[26] H. Takami, T. Kanki, S. Ueda, K. Kobayashi, H. Tanaka, *Phys. Rev. B* **85** (2012) 205111

[27] V. Eyert, *Ann. Phys.* **11** (2002) 650

[28] T. Mitsuish, *Jpn. J. Appl. Phys.* **6** (1967) 1060

[29] P. J. Fillingh, *J. Appl. Phys.* **38** (1967) 4823

[30] B. Fisher, *J. Phys. C: Solid State Phys.* **8** (1975) 2072

[31] B. Fisher, *J. Phys. C: Solid State Phys.* **9** (1976) 1201
[32] M. M. Qazilbash *et al.*, *Phys. Rev. B* **83** (2011) 165108
[33] L. Pellegrino *et al.*, *Adv. Mater.* **24** (2012) 292

CHAPTER 2

Experimental apparatus and nanofabrication technique

2.1 Pulsed laser deposition technique

In this study, the pulsed laser deposition (PLD) technique has been utilized to make transition metal oxide thin films. The PLD technique is one of the most effective techniques to fabricate materials as oxides which include several elements. Smith and Turner [1] first applied the technique to film formation in 1965 and the crystal growth techniques using PLD have been developed since the success of high-temperature superconductor film growth. Figure 2.1 shows the schematic illustration of laser ablation phenomena. The pulsed laser beam is focused on the target surface and an ablation is induced. The ablated atoms and ions are deposited on the substrate and crystallized on the substrate epitaxially, resulting in growth of single crystal thin film. PLD technique is the excellent film formation method for the selectivity in ambient atmospheres such as oxygen, nitrogen and so on. In addition, it is possible to make even films including several elements and high melting points in exact stoichiometry. The excess energy of ablated atoms and ions are also effective to make high quality films.

In my experiment, the base pressure of the chamber was maintaining to 10^{-4}-10^{-3} Pa. Oxygen gas is introduced into the PLD chamber during film growth. The pulsed laser (ArF eximer laser: wave length λ = 193 nm) was focused on target material through the quarts window with pulse frequency of 2 Hz. Thin film formation was carried out under the following conditions. The substrate is Al_2O_3 (0001) or TiO_2 (001) single crystal, substrate temperature (T_S), from 360℃ to 450℃; deposition rate, (1.6～16 Å/min), oxygen pressure (P_{O2}) is 1 Pa; film thickness, about 100 nm. Thickness and surface morphology were measured by atomic force microscopy (AFM) and scanning electron microscopy (SEM). Targets were pellets of single-phase V_2O_5 which were placed at the center of a vacuum chamber. The V_2O_5 targets were prepared by grounding V_2O_3 powder, followed by pressing at 80 kg/cm^2 and sintering at 410 °C. After the film formation, samples were cooled in oxygen atmosphere at 1 Pa.

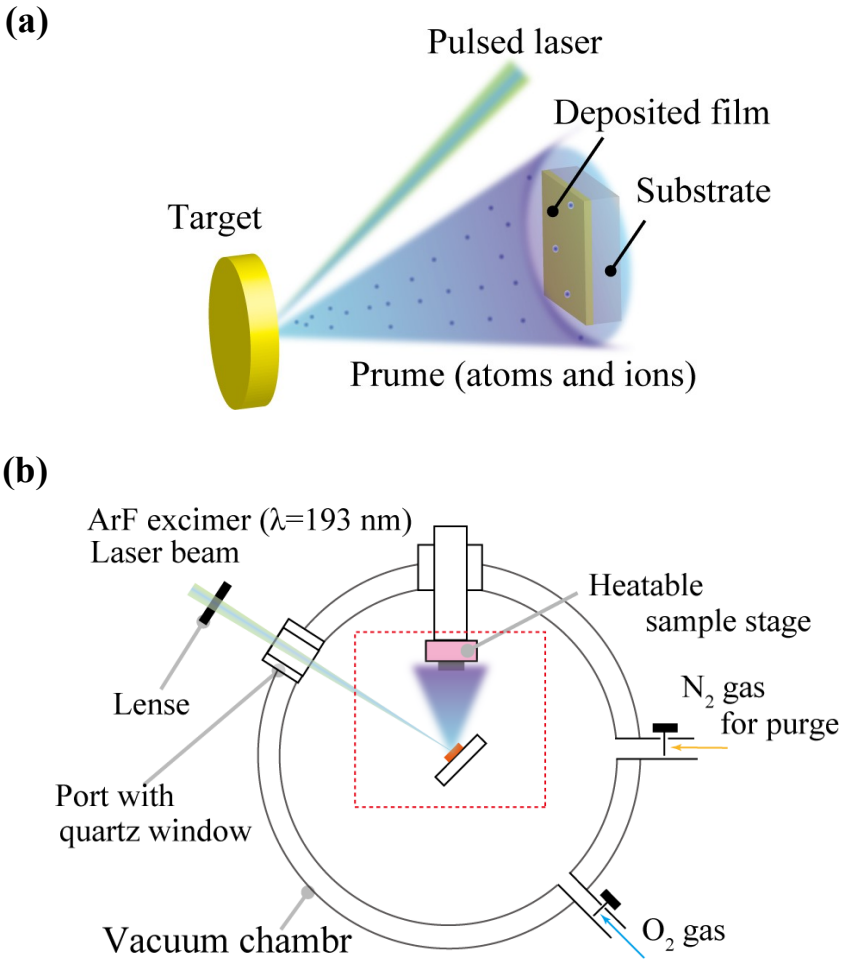

Fig 2.1 (a) Schematic illustration during the film formation using PLD technique. (b) Schematic illustration of PLD chamber and fabrication method.

2.2 Nanoimprint Lithography

To fabricate the VO_2 nanostructures, two kinds of approach have been employed. One is a top-down approach like photolithography [2], and the other is a bottom-up approach like vapor transport method [3]. In the former case, minimum size achieved by the standard photolithography technique is around several micrometers which is much higher than the size of the single electronic phase expected from the image captured by using the scanning probe microscopy technique (<100nm). In the latter case, minimum

size achieved by the vapor transport method is several tens or hundreds of nanometers, but the size, shape and position is uncontrollable, which is a major obstacle for systematic investigation in size and device application.

Nanoimprint lithography(NIL) is a nonconventional lithographic method which is able to fabricate the nanostructures with a high controllability of size, shape an position in a large area. The achievable size ranges from macroscale to nanosclae, which enables systematic investigation into the role of electronic phase of VO_2 in various structural size. The NIL is categorized into three types, microcontact printing (or soft lithograpy), thermal-NIL, and ultraviolet (UV)-NIL. G. M. Whitesides *et al.* first reported microcontact printing technique in 1993,[4] and thermal-NIL was developed by S. Y. Chou *et al.* in 1995.[5] UV-NIL, which was used in my research, was developed by J. Haisma *et al.* in 1996.[6] UV-NIL is the most excellent technique among the three techniques in terms of resolution, throughput, and alignment. Figure 2.2 shows schematic illustration of the process for UV-UIL.

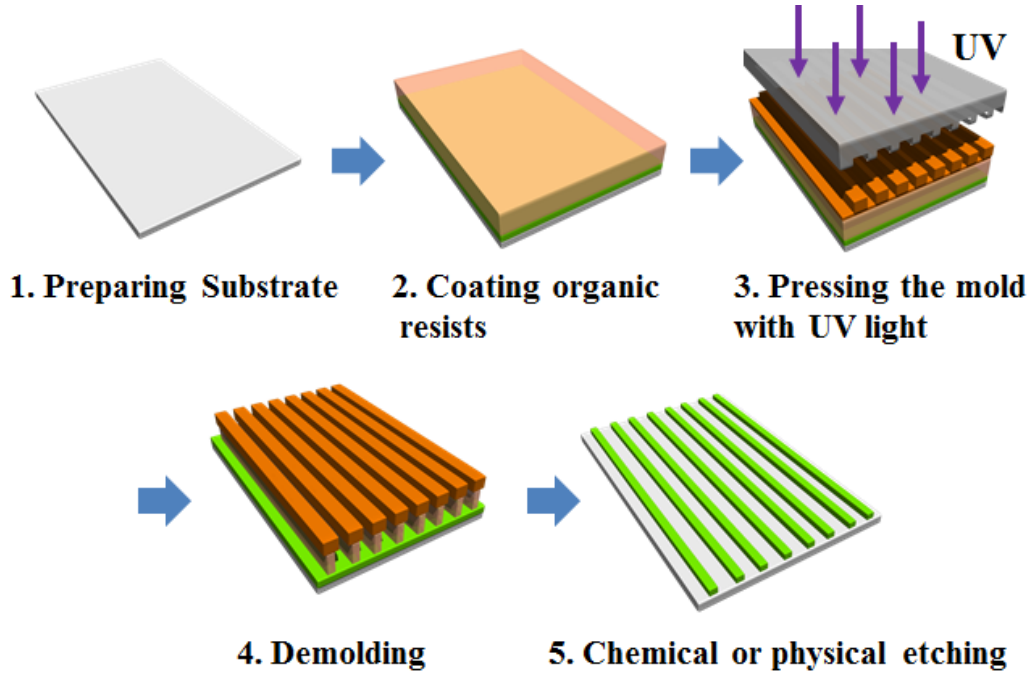

Fig. 2.2 Schematic illustration for UV Nanoimprint lithography

In the UV-NIL , high liquidity UV curable polymer resist is spin-coated on substrate. And then, the mold which has nanoscale patterns on the surface is put on UV curable resist, and pressed at low pressure (under 0.1 MPa) with exposure of UV light. Finally,

the mold is removed (demolding) and polymer nanostructures are patterned on the substrate. The first stage of the NIL process is the molding of thin polymer film which is compressed between the mold and substrate, and the viscous polymer is forced to flow into the cavities of the mold. So polymer rheology issues should be taken into account when optimizing the pressing process. To achieve a reasonable process time and yield, molding materials with low viscosities are used. For high aspect ratio structures, demolding becomes a critical step in the replication process. In this process, adhesions or imperfections of the walls tend to occur due to the high friction between mold and polymer during the demolding. To reduce friction forces, anti-adhesion layers especially self-assembled monolayer on the mold is employed. After the molding process, to transfer the patterns of the organic resist to under layer materials (VO_2 in this study), Reactive ion etching (RIE) is utilized. To exactly transfer the nanopatterns, the residual height of polymer after the pressing process has to be reduced to an extent that RIE does not change significantly the shape of initial structures.

2.3 Characterization techniques

2.3.1 X-ray diffraction measurements

In this experiment, the Cu-Kα line (λ = 1.54056 Å) was used for the measurement of 2θ-θ scan. An X-ray diffraction apparatus (RINT-2000, Rigaku, Japan) was used to confirm the crystal structure of vanadium oxide thin films.

2.3.2 Electrical transport measurement with optical observation

I used source measure unit (2635A, Keithley, USA) and variable-temperature-controlled stage with a peltier element (LTS120, Linkam, UK) combined with optical microscope image (VH-Z500R, KEYENCE, Japan) to measure temperature dependence of electrical and optical properties at the same time. Figure 2.3(a) shows the whole experimental system. Sample was mounted on a glass substrate and heated up and cooled down on a peltier-controlled stage as shown in Fig.

2.3(b). Temperature was swept from 7 to 97 °C with the stability and accuracy of 0.1 K. The chamber was covered not to be affected by the temperature fluctuation in the atmosphere as shown in Fig. 2.3(c). I also used Physical Properties Measurement System (PPMS, Quantum Design, USA) to measure temperature dependence of resistivity at small temperature steps around 10 mK by use of a four probe method. The lead line is ultrasonically bonded onto the electrode pad of the sample.

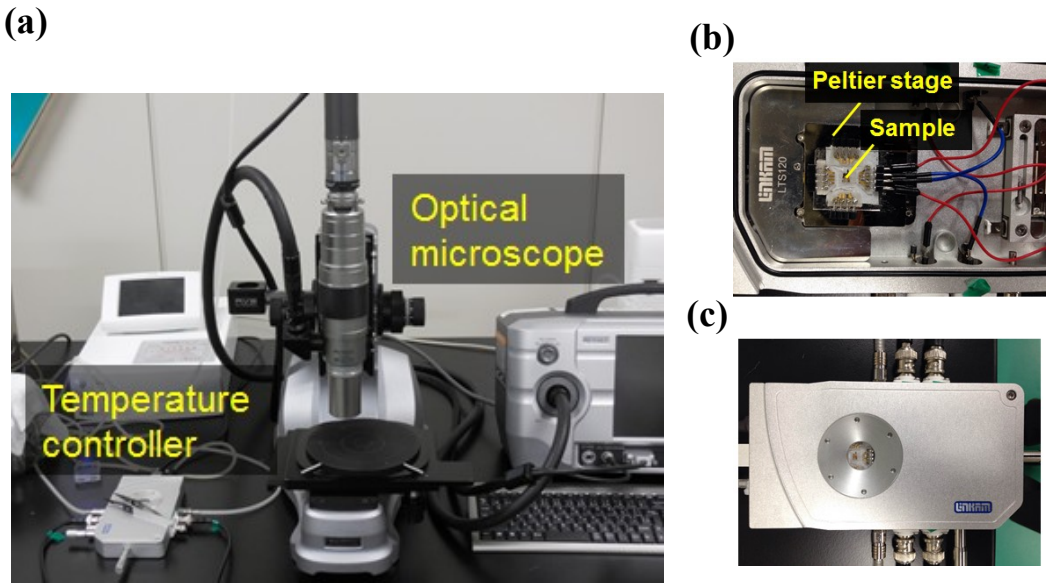

Fig. 2.3 Experimental system to measure the electrical transport properties and optical observation at the same time (a) Whole measurement system (b) Sample installation onto the Peltier stage (c) Covered chamber during the measurement

2.4 References

[1] H. M. Smith, A. F. Turner, *Appl. Opt.* **4** (1965) 147

[2] A. Sharoni, J. G. Ramirez, I. K. Schuller, *Phys. Rev. Lett.* **101** (2008) 026404

[3] J. Wu *et al*., *Nano Lett.* **6** (2006) 2313

[4] A. Kumar, G. M. Whitesides, *Appl. Phys. Lett.* **63** (1993) 2002

[5] S. Y. Chou, P. R. Krauss, P. J. Renstrom, *J. Vac. Sci. Technol. B* **14** (1996) 4129

[6] J. Haisma, M. Verheijen, K. vandenHeuvel, J. vandenBerg, *J. Vac. Sci. Technol. B* **14** (1996) 4124

CHAPTER 3

Tuning metal-insulator transition by one dimensional alignment of giant electronic domains in artificially size-controlled epitaxial VO_2 wires

I achieved to control spatial dimensionality of disordered configurations of giant electronic domains in systematically size-changed VO_2 wires on TiO_2 (001) substrates. One-dimensional alignment of the domains appears in wires narrower than 15 μm width, while two-dimensional configurations were observed for larger ones. The rearrangement of domains from two to one dimension causes modification of electronic properties.

3.1 Introduction

VO_2 has attractive electronic properties, showing orders-of-magnitude changes in resistivity at its MIT at around 340 K.[1] These changes are accompanied by structural deformation between the low-temperature monoclinic insulating phase and the high-temperature rutile metallic phase.[2] When focusing on the nano-spatial area near the MIT, the VO_2 system exhibits mixed electronic phases consisting of metallic and insulating states.[3] Electronic inhomogeneity plays an important role in the conductive properties of such materials. In fact, in confined spaces with comparable size to the domains, individual domain behavior is observed as first-order resistive jumps due to electronic avalanches.[4] This nano-spatial conduction character yields aspects different from those observed in typical film samples and results in important electronic properties to realization of application such as phase-change memories [5] and Mott field-effect transistors [6]. Most reports have investigated nano- to mesoscopic domain structures in VO_2 beams in the presence of elastic interactions [7] and have dealt with quasi-one-dimensional (1D) domains forming longitudinal metal/insulator phase alignment, which are highly sensitive to bending [8] and uniaxial stress.[9] Recently, giant metallic domains on the microscale were discovered in VO_2 thin films on TiO_2 (001) substrates, and their multiple avalanches resulted in extremely large MIT even in films several tens of micrometers in size.[10] Transition efficiency, dR/dT, was reported to be enhanced to up to a hundred times larger than that of conventional VO_2 film on Al_2O_3 (006) substrate, and its behavior was revealed to be dominated by a random 2D percolative conduction mechanism. Visible electronic avalanches on the microscale are expected to support the breakthrough of a physical relation between domain configuration and electronic properties.

In this chapter, I demonstrate artificial and systematic dimensional control of metal-insulator domain alignment from 2D to 1D and elucidate the correlation between dimensionality and electronic properties using thin-film-based VO_2 wires on TiO_2 (001) substrate. Typically, a vapor transport method [11] is used to prepare VO_2 wires. Although this is a convenient method for the synthesis of nano-wires as small as around 10 nm in width,[12] there are some problematic issues concerning systematic and artificial control of their positioning and ordering within large areas. A nanoimprint-based top-down process, however, overcomes this problem because it can produce a large number of artificially designed structures from several nanometers to micrometers scale with good fidelity of size and shape.[13] I applied a nanoimprint lithography technique to fabricate nano- to micro-sized VO_2 wires and obtained high controllability of size, shape, and position over a large area.[14] The VO_2 wires prepared in this study allowed systematic investigation into the dependence of spatial dimensionality on wire width for disordered configurations of giant metal and insulator domains in VO_2 films on TiO_2 (001) substrates, and were forced to align one dimensionally.

3.2 Experimental

Figure 3.1 shows a schematic illustration of the fabrication process in VO_2 nanostructures. As a first step, 60 nm-thick VO_2 thin films were prepared on Al_2O_3 (006) and TiO_2 (001) substrates with 10 mm × 10 mm in size by a pulsed laser deposition technique (ArF excimer laser: λ = 193 nm) under oxygen pressure at 1 Pa and a substrate temperature of 360 °C. Concerning the ultraviolet nanoimprint lithography (UV-NIL) process, two types of resists were coated on the prepared thin films. Initially, a bottom layer (NXR3032, Nanonex, USA) was spin-coated at 3000 rpm for 20 seconds and then baked at 110 °C for 10 min. A top layer (NXR2030, Nanonex, USA) was then spin-coated at 3000 rpm for 7 seconds on the bottom resist. The thicknesses of the bottom and top resists were 600 nm and 200 nm, respectively (see Step 2 in Fig. 3.1). Nano-wire patterns with various line widths ranging from 60 nm to 10 μm and a quartz mold depth of 200 nm were printed to the top resist on the

sample at 50 bar of pressure and exposure to UV light for 3 minutes at room temperature using a nanoimprinter (Eitre 3, Obducat Technology AB, Sweden) (Step 3). The same geometry of the mold was copied to the top resist. After demolding, the residual top resist was removed by reactive ion etching (RIE) using a CF_4 gas source at a working pressure of 2 Pa and RF power of 50 W for 2 min. The bottom layer was easily removed using an O_2 plasma with RIE under the same conditions while the top layer resisted the O_2 plasma. The etching rate for the NXR2030 resist (the top layer) was approximately 50 nm/min in a CF_4 plasma and 15 nm/min in an O_2 plasma in a longitudinal direction, while that for the NRX3032 resist (the bottom layer) was approximately 200 nm/min in an O_2 plasma, which is over 10 times faster than the etching rate for the NXR2030 resist. The different etching rate in a longitudinal direction affects the side etching rate and produces mushroom-like structures (Step 4), which enabled us to make narrower mask patterns compared with the original mold patterns [15]. These narrow patterns of the bottom layer were transferred to the VO_2 layer using CF_4 plasma (Step 5). To effect removal of the residual resists, samples were immersed into 1-methylpyrrolidone at 90 ºC for 1 hour (Step 6). After being subjected to ultrasonic vibration for 1 min in acetone to remove the 1-methylpyrrolidone and completely remove the residual resist (Step 6), I obtained VO_2 nanostructures which were smaller than the original patterns. Figure 3.2 shows a field emission scanning electron microscopy (FESEM) image of the VO_2 epitaxial nano-wires on Al_2O_3 (006) single crystal substrates. One can see the nanowires with three types of width, which are 450 nm, 700 nm and 1200 nm, respectively, over a large area in the order of 100 μm × 100 μm, and clear-edged shapes of VO_2 nano-wires in the inset figure of the rectangular SEM image. The height of the VO_2 wires was 60 nm, which was the same height as the initial VO_2 thin films prepared (see inset of Fig. 3.2 showing an AFM image).

VO_2 epitaxial nano-wires whose widths are systematically controlled from 30 nm to 30 μm were obtained. My original technique enabled fabrication of 30 nm-width wires by precisely controlling the process conditions (See Fig. 3.3, for the detailed method and XRD result).

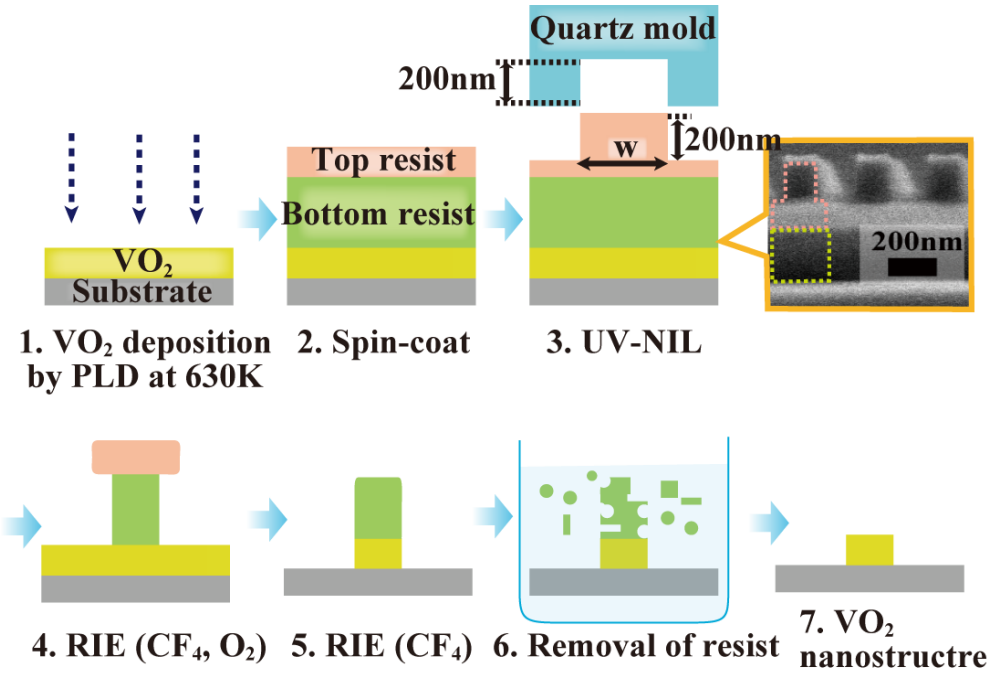

Fig. 3.1 Schematic illustration of the VO_2 nanostructure fabrication process

3.3 Results and Discussion

Figure 3.3(a) shows SEM images of each process in the selective ion etching of the bi-layer resists. Selective etching of the bi-layer resists using different etching rates overcomes the size limitations of nanoimprint molds, especially for narrow widths of less than roughly 100 nm. This effect is known as undercutting.[15] The selective etching produces a mushroom-like configuration, as shown in the cross-sectional SEM image of a bi-layer resist in the center panel of Figure 3.3(a). The width of the bottom resist lines (w_{BR}) is dependent on the initial line width of the mold (w_M), the side etching rate of the bottom resist (γ), and the etching time (t). That is, w_{BR} can be roughly represented as $w_{BR} = w_M - 2\gamma t$ until the bottom resist disappears. Eventually, the widths of the VO_2 nano-wires are determined by the widths of the bottom resist lines. In this experiment, I used mold lines of 60 nm in width ($w_M = 60$ nm), performed the selective side etching for 3 min, and finally obtained VO_2 lines that were 30 nm wide, as shown in the right panel of Figure 3.3(a). The obtained side etching rate γ was 5 nm/min.

Figure 3.3(b) shows XRD patterns of VO_2 on Al_2O_3 (006) substrates before (gray

line) and after (orange line) the nanoimprint process. Due to the large patterning area (2 × 3 mm) of the VO_2 lines, XRD (X-ray diffraction: Rigaku RINT2000) results were acquired using the same manner as for bulk materials. The peak at $2\theta = 41.7°$ indicates reflection from a (006) sapphire substrate and the peak at $2\theta = 40.0°$ corresponds to reflection from the (020) peak of VO_2. Only (020) and (040) peaks were observed, indicating that the VO_2 lines were well oriented in the *b*-axis direction, with the absence of other orientations even after the nanoimprint process. This technique is advantageous in the range of achievable size as well as the minimum size of the nanostructures as shown in Fig. 3.4. The w_{max} (w_{min}) is the maximum (minimum) size of the structure reported in the each literature.

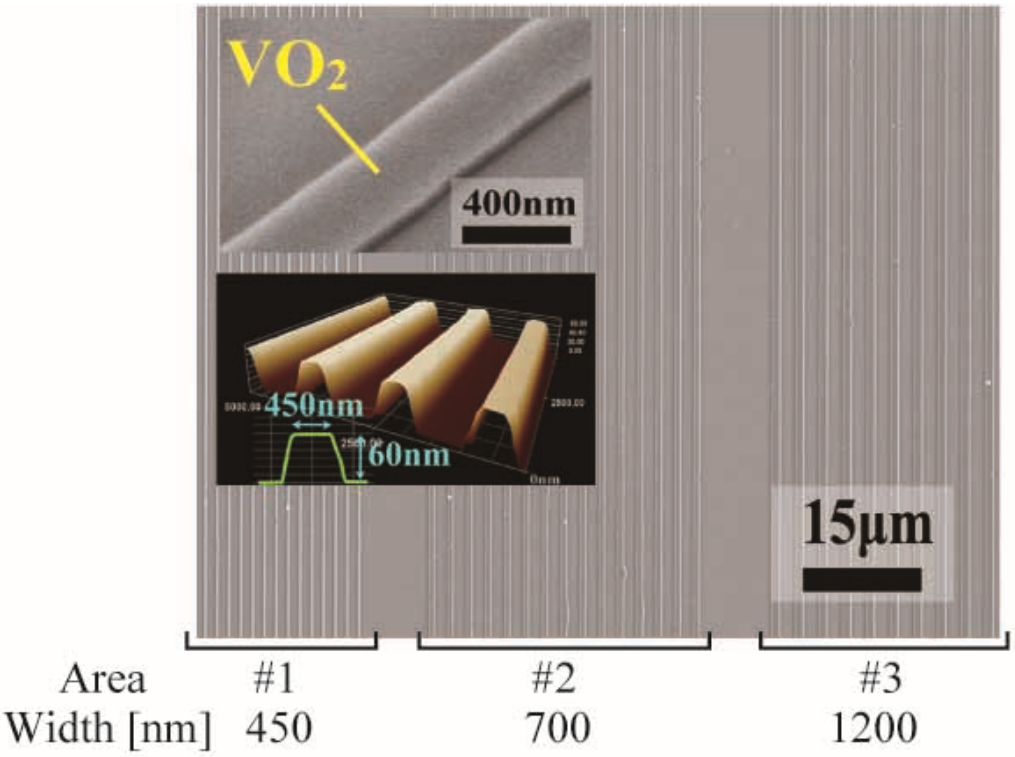

FIG. 3.2 Top-down SEM image of VO_2 nanowires fabricated by using the nanoimprint lithography process in a wide area. Upper inset shows a 50 °C-tilted and magnified SEM image of a nanowire showing a rectangular beam structure. Lower inset shows an AFM image.

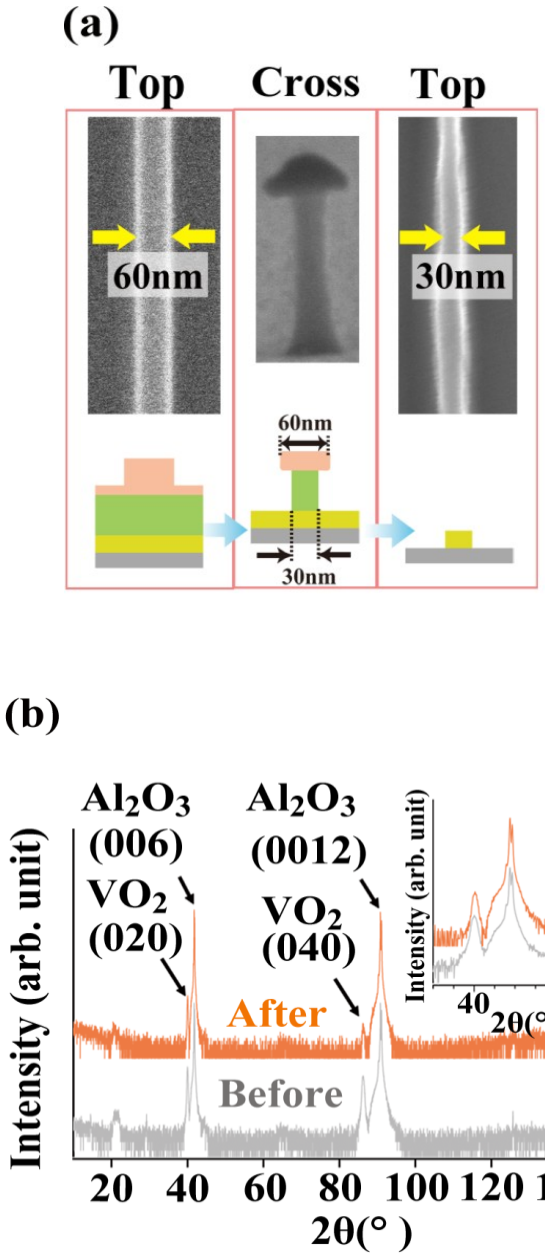

Fig. 3.3 (a) SEM images of each process in the selective ion etching of the bi-layer resists.(b) XRD patterns of VO_2 on Al_2O_3 (006) substrates before (gray line) and after (orange line) the nanoimprint process.

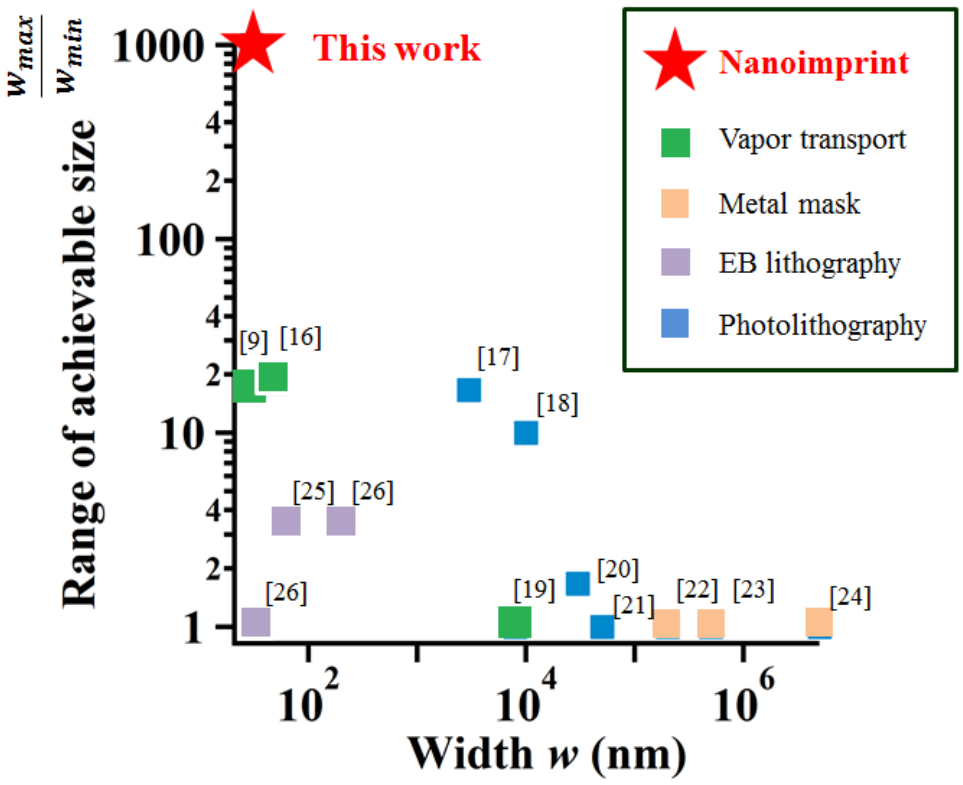

Fig. 3.4 Scattering plot as a function of range of achievable size (vertical axis) and minimum width (horizontal axis) for typical nanofabrication techniques used to fabricate VO_2 nanostructures.

In terms of dimensional control of domain configuration as a function of sample size, micro-sized domains are advantageous for an initial experiment because their domain configurations can be easily observed using an optical microscope. It is possible to recognize metallic and insulating domains by examining differences in reflectance in the optical region.[28] Thus, I observed individual domain behavior as a function of temperature in VO_2 wires of various widths prepared on TiO_2 (001) substrates using the present nano-fabrication technique. Metal-insulator domain configurations across the metal-insulator transition temperature were investigated as a function of wire width. Dimensionality of the metal-insulator domain configuration and its borderline were also investigated as a function of wire width. I estimated the spatial fraction of metal domain phase (P values) of the VO_2 wires by direct observation using an optical microscope.

As a typical example, metal-insulator domain configurations in wires with widths

of 30 and 1 μm are shown in Fig. 3.5. Figure 3.5(a) shows a schematic illustration of a 30-μm-wide film and Fig. 3.5(b) shows the corresponding optical microscope images at temperatres ranging from 17 to 40 °C in a 30 × 30 μm region. Initially, the VO_2 domains were in completely insulating states at 17 °C, which corresponds to $P = 0$. With increasing temperature to around 28 °C, dark metallic domains appeared randomly in a 2D plane from the insulating states ($P = 0.50$). At 29 °C, I visually identified a metallic path connected between both ends indicated by the virtual electrodes shown in Fig. 3.5(b) ($P = 0.59$). This critical P is defined as P_C (critical occupation probability [29]). The P_C values estimated in visual from optical images fall within the range of about 0.5 to 0.65 in my research as shown in the error bar of the P_C values in the 30-μm-wide wires in Fig. 3.6. The P_C is a good index for an evaluation of the dimensionality and is approximately 0.59 in the universal 2D site-percolation models.[29] The P value observed at 29 °C in this study is in good agreement with this value. Finally, a metallic phase covered the whole area at 40 °C ($P = 1.0$). In contrast, 1D alignment of domains was clearly observed for the 1-μm-wide VO_2 wires (Fig. 3.5(c)). Figure 3.5(d) shows optical microscope images of the 1-μm-wide wires at temperatures from 17 to 50 °C in an 8 × 8 μm region. Obviously, Pc is 1 in the 1D configuration. It was apparent that each domain was forced to be confined by the wire width and thus one-dimensionally aligned. Therefore, the connection of a metallic path between electrodes was limited only when $P = 1.0$, as observable in the image taken at 50 °C in Fig. 3.5(d).

To accurately discuss the dimensionality of the metal-insulator domain configuration and its borderline, I estimated the P_C values of VO_2 wires with various widths by direct observation using an optical microscope. Figure 3.6 shows the dependence of P_C value on VO_2 wire width. The averaged P_C values of wires over 15 μm in width, evaluated from 10 different areas, were 0.55 to 0.6, approximately corresponding to the 2D percolation system. Domain configuration approached 1D with decreasing width, and the borderline between 1D and 2D appeared clearly at around 15 μm. This width is almost comparable with metallic domain sizes reported for VO_2 thin films on TiO_2 (001) substrates.[10] Additionally, the error bar of the standard deviation, estimated from 10 different areas, decreased with width. Eventually, the metal-insulator domain configuration became perfectly 1D without any dependence on area.

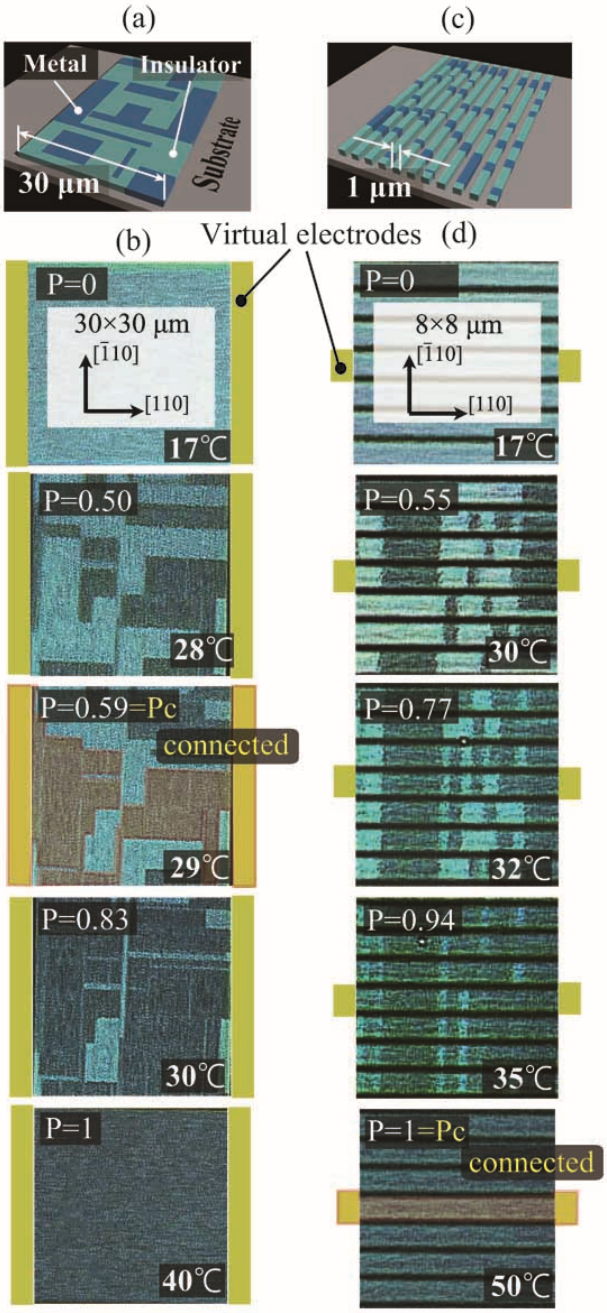

Fig. 3.5 (a) Schematic illustration of a 30-μm-wide VO_2 wire on TiO_2 (001) substrate. (b) Optical microscope images of a 30 × 30 μm region showing a 30-μm-wide wire at temperatures from 17 to 40 °C. Two virtual electrodes are shown at the left and right edges of the images. (c) Schematic illustration of 1-μm-wide wires. (d) Optical microscope images of a 8 × 8 μm region showing a 1-μm-wide wire at temperatures from 17 to 50 °C. Two virtual electrodes are shown at the left and right edges of the center wire of the images.

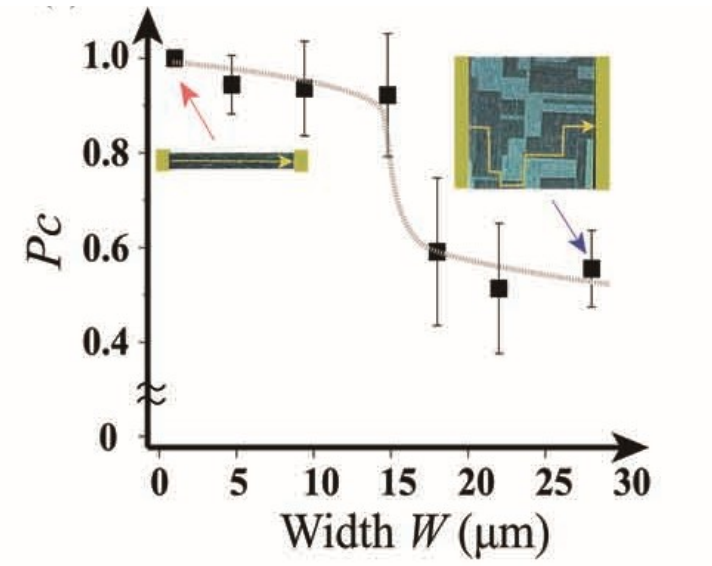

Fig. 3.6 *Pc* value vs width for the VO_2 wires. The value of *Pc* was about 0.59 in the case of wires 28 μm in width, indicating that the system is two-dimensional, whereas the value of 1 in the case of wires 1 μm in width indicates that the system is one-dimensional.

In their electronic properties, Wires having 1D domain alignment exhibited a much higher and clearer discrete drop in resistivity than the 2D thin film, as shown in Fig. 3.7(a). Moreover, the transition temperature of the 1D wires apparently shifted to a higher temperature. Thus, their electronic properties were tunable by variation of dimensionality. The conductivity observed in the 2D thin film followed the percolation model, expressed as: [27]

$$\sigma_{2D} = \sigma_0 (P - P_C)^t \tag{3.1}$$

where P and $1–P$ are the occupation probability of the metallic and the insulating domains at a certain temperature, respectively, and t is the critical exponent. In the case of the 2D site percolation model, P_C and t are known to be approximately 0.59 [31] and 1.4 [30], respectively. In addition, the value of σ_0 can be estimated from the metallic state in the high temperature region, that is, by substituting $P = 1$ and $\sigma_{2D} = 100$ ohm^{-1} cm^{-1} for the experimental value at 370 K, which is 348 ohm^{-1} cm^{-1}. Fig. 3.7(b) shows experimental and theoretically estimated conductivities vs metallic fraction P for both 2D film and 1D wires. In the case of 2D film, the blue solid line calculated using Eq. 3.1 and the above-mentioned values fit well to the plotted blue dots derived from the

experimental conductivity and P estimated from the optical images of the 50 × 50 μm^2 thin film taken at varied temperatures (See Fig. 3.8 for the temperature dependence of resistivity and optical microscope images). Thus, the conductive behavior observed in the present VO_2 thin films is in good agreement with the calculations based on the 2D percolation model. The conductive behavior of the 1D wires, on the other hand, satisfies the 1D serial resistance model expressed as follows:

$$\frac{1}{\sigma_{1D}} = \frac{P}{\sigma_M} + \frac{1-P}{\sigma_I} \tag{3.2}$$

where σ_M and σ_I are the conductivity of metallic and insulator states estimated from the experimental data in the Fig. 3.7(a), 65.8 and 0.171 ohm^{-1} cm^{-1}, respectively. The plotted red dots which relate σ with P fit well to the curve calculated using Eq. 3.2.

Thus, variation of domain configuration from 2D to 1D strongly affects conductive behavior, also changing from 2D to 1D. This control of electronic behavior through the rearrangement of domains offers the potential for development of oxide electronics with strongly correlated electrons.

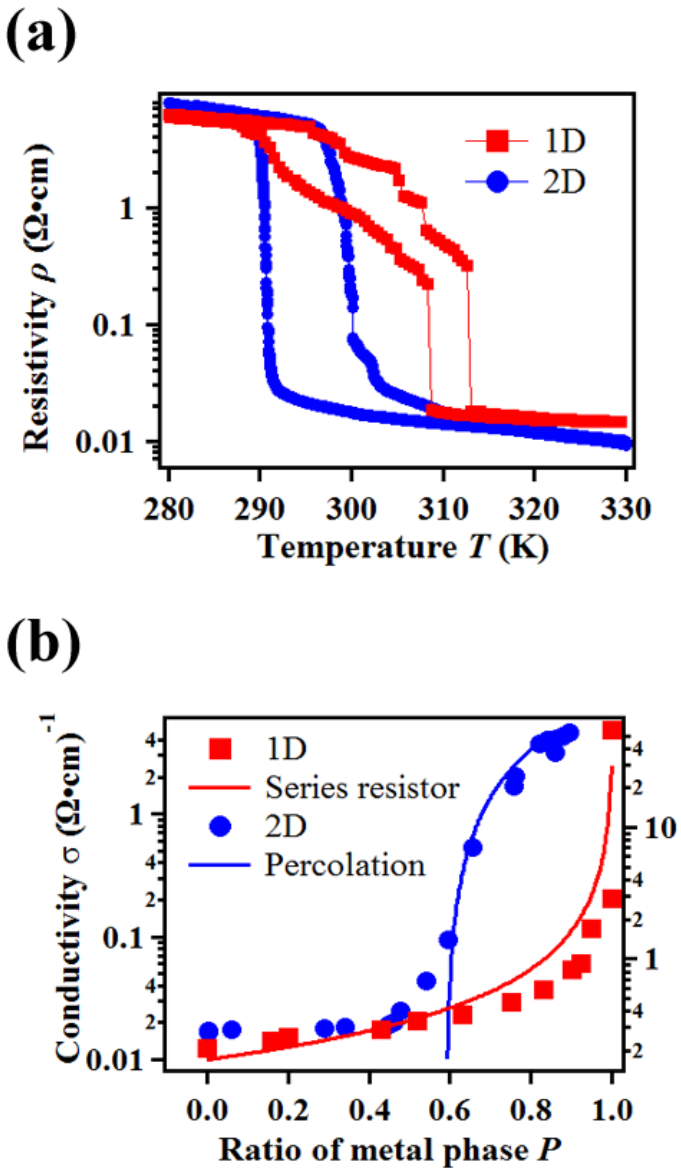

FIG. 3.7 (a) Temperature dependence of resistivity for both 1D (red square) and 2D (blue circle) domain configurations. (b) Conductivity vs ratio of metal phase for 1D (red square) and 2D (blue circle) domain configurations. Red lines show expected results calculated from a 1D serial resistance model, while the blue one shows expected results calculated from a 2D percolation model.

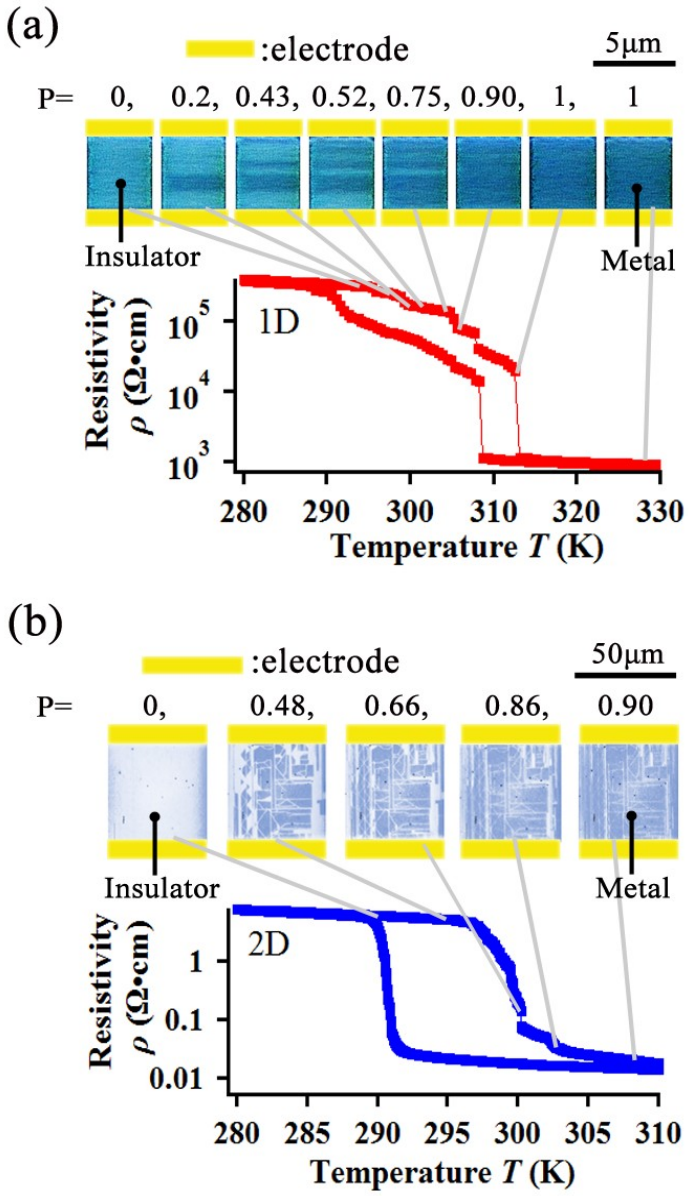

Fig. 3.8 Temperature dependence of resistivity and corresponding optical microscope images at several temperatures for (a) one-dimensional and (b) two-dimensional domain configurations. The ratios of metal domains, *P*, were estimated from the optical microscope images and are shown above the respective images. It was clearly observed that digitized insulator-metal transitions occurred for both types of samples and resistivity jumps corresponded to the generation of a new metallic domain. In the 1D sample, the largest insulator-metal transition occurred at the final transition, as expected from serial resistance model, which was not realized in the 2D sample.

3.4 Conclusion

I fabricated VO_2 nano-to-micro wires with well-positioned alignment over a wide area by a nanoimprint lithography (NIL) technique, and investigated the dependence of spatial dimensionality on wire width for disordered configurations of metal and insulator domains in VO_2 wires on TiO_2 (001) substrates. Domains with 1D alignment were realized in wires with narrower width than the threshold width of 15 μm, which was the average size of the domains. Moreover, variation of dimensionality in the domain configuration caused modification of the electronic properties. The concept of dimensional control of domain configuration through precise size control of thin films will provide new strategies for creation of unique electronic functionalities in materials with coexisting different electronic phases.

3.5 References

[1] F. J. Morin, *Phys. Rev. Lett.* **3** (1959) 34

[2] J. B. Goodenough, *J. Solid State Chem.* **3** (1971) 490

[3] M. M. Qazilbash *et al.*, *Science* **318** (2007) 1750

[4] A. Sharoni, J. Ramírez, I. Schuller, *Phys. Rev. Lett.* **101** (2008) 026404

[5] S. Meister, D. T. Schoen, M. A. Topinka, A. M. Minor, Y. Cui, *Nano Lett.* **8** (2008) 4562

[6] S. Hormoz, S. Ramanathan, *Solid-State Electron.* **54** (2010) 654

[7] A. Tselev *et al.*, *Nano Lett.* **10** (2010) 2003

[8] J. Cao *et al.*, *Nat. Nanotechnol.* **4** (2009) 732

[9] J. Q. Wu *et al.*, *Nano Lett.* **6** (2006) 2313

[10] K. Kawatani, H. Takami, T. Kanki, H. Tanaka, *Appl. Phys. Lett.* **100** (2012) 173112

[11] P. D. Yang *et al.*, *Adv. Func. Mater.* **12** (2002) 323

[12] P. Yang, R. Yan, M. Fardy, *Nano Lett.* **10** (2010) 1529

[13] A. N. Hattori, A. Ono, H. Tanaka, *Nanotechnology* **22** (2011) 415301

[14] S. Y. Chou, P. R. Krauss, P. J. Renstrom, *J. Vac. Sci. Technol. B* **14** (1996) 4129

[15] N.-G. Cha *et al.*, *Nanotechnology* **20** (2009) 395301

[16] J. Wei, Z.Wang, W. Chen, H. Cobden*, Nat. Nanotechnol.* 4 (2009) 420

[17] L. Pellegrino *et al., Adv. Mater*. **24** (2012) 2929

[18] Y. Lee *et al., Appl. Phys. Lett*. **92** (2008) 162903

[19] A. Tselev *et al., Nano Lett*. **10** (2010) 4409

[20] N. Manca *et al., Adv. Mater*. **25** (2013) 6430

[21] T. Kanki, K, Kawatani, H. Takami, H. Tanaka, *Appl. Phys. Lett.* **101** (2012) 243118

[22] J. Duchene, M. Terraillon, P. Pailly, G. Adam, *Appl. Phys. Lett.* **19** (1971) 115

[23] J. Kim, C, Ko, A, Frenzel, S. Ramanathan, J. E. Hofman, *Appl. Phys. Lett.* **96** (2010) 213106

[24] T. Driscoll, H. T. Kim, B. B. Chae, M. D. Ventra, D. N. Basov, *Appl. Phys. Lett.* **95** (2009) 043503

[25] E. U. Donev, J. I. Ziegler, R. F. Haglund Jr., L. C. Feldman, *J. Opt. A* **11** (2009) 125002

[26] M. J. Lee et *al.*, *Adv. Mater.* **19** (2007) 3919

[27] M. J. Dicken et *al.*, *Opt. Express* **17** (2009) 18330

[28] P. Jin, G. Xu, M. Tazawa, K. Yoshimura, *Jpn. J. Appl. Phys.* **41** (2002) 278

[29] M. Isichenko, *Rev. Mod. Phys.* **64** (1992) 961
[30] B. Watson, P. Leath, *Phys. Rev. B* **9** (1974) 4893
[31] R. M. Ziff, S. R. Finch, V. S. Adamchik, *Phys. Rev. Lett.* **79** (1997) 3447

CHAPTER 4

Multistep metal-insulator transition in VO_2 nanowires on Al_2O_3 (0001) substrates by controlling nanoscale electronic domain

I observed temperature- and voltage-induced multistep MIT in VO_2 nanowires fabricated on Al_2O_3 (0001) substrates. The nanowires with 200 nm width shows multistep MIT which include nearly two-order of resistivty change at 0.5 K temperature step. These multstep resistivity jumps can be understood as a transition of single electronic domain whose size is estimated to be around 70 - 100nm from numerical calculation. I found the temperature-induced isotropic cunductive behavior becomes similar to the voltage-induced anisotropic one with decreasing the width of nanowires.

4.1 Introduction

VO_2, a typical material for strongly correlated transition metal oxides, shows first order MIT at 340K accompanied by a resistivity change over 5 orders of magnitude.[1, 2] From the nanoscopic point of view, VO_2 shows mixed electronic phases consisting of metallic and insulating states around the MIT temperature.[3] Because the electronic inhomogeneity plays an important role in the underlying physics of such materials, many researchers are trying to understand the role of these electronic domains in the MIT.[3, 4] With reducing the geometry of the materials down to comparable size to the domains, individual domain behavior is observed as multistep resistive jumps.[4, 5] So it is very important to realize and investigate the multistep MIT from the view point of fundamental physics of spatially inhomogeneous domain system and technological application such as memristive [6, 7] or switching devices [8, 9].

Recently, the relationship between domain configuration and conductive properties are unveiled by optical observation of micro-sized large domains in VO_2 on TiO_2 (001) substrates,[5, 10] and these results shows that the multistep MIT can be structurally or electrically controlled through domain arrangement.[11, 12] To apply the multistep MIT for nanodevice and to investigate the fundamental physics of nanoelectronic domains observed by Qazilbash *et al*.,[3] realization of multistep MIT in VO_2 on Al_2O_3 substrates are very attracting. Sharoni *et al*.[4] reported the temperature-induced multistep MIT in VO_2 microstructures on Al_2O_3 substrates by reducing the electrode gap to several hundreds of nanometers. Judging from the small resistance change observed in their report, single domain size seems to be less than 100 nm. So it is very important to

reduce the samples size down to the comparable size of single domain of VO_2 on Al_2O_3 (0001) substrates to investigate single domain behavior.

In this chapter, I measured the resistivity of VO_2 nanowires on Al_2O_3 (0001) substrates as a function of temperature and voltage, and observed multistep metal-insulator transition (MIT) for both cases. I discuss about the multistep MIT from a view point of single domain's transition in the nanowires

4.2 Experimental

VO_2 epitaxial nanowires were fabricated on Al_2O_3 (0001) single crystal substrates by using nanoimprint lithography. Detailed process for device preparation is described in the chapter 3. Figure 4.1(a) shows a typical false-colored SEM images of the VO_2 nanowire (green) with Ti/Au (yellow) electrodes fabricated on Al_2O_3 (0001) substrates. Width of the wire is 200 nm and electrode gap is 400 nm, which are measured from the SEM image and the thickness is 50 nm measured by using atomic force microscope. I used source measure unit (2635A, Keithley, USA) and a temperature-controlled stage (LTS120, Linkam, UK) to measure temperature dependence of electric resistance.

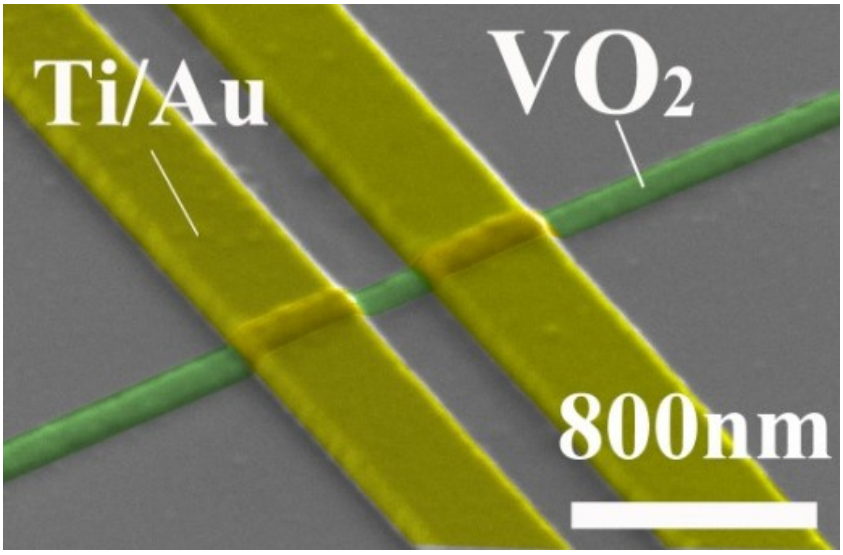

FIG. 4.1 (a) False color SEM picture of VO_2 nanowires (green) with Ti/Au (yellow) electrodes fabricated on Al_2O_3 (0001) substrate by using nanoimprint lithography. Width of the wire is 200 nm and electrode gap is 400 nm and the thickness is 50 nm.

4.3 Result and Discussion

Figure 4.2 shows a temperature dependence of resistivity (RT) for VO_2 nanowire (red square with line) comparing with the result of conventional thin film (gray circle with line). The nanowire exhibited multistep MIT with discrete change of resistivity near the MIT temperature while the thin film sample shows continuous change of resistivity at all measured temperature. Nearly two orders of resistivity change at single temperature step (0.5 K) was much higher than the value previously reported by Sharoni *et al*.[4] In order to investigate the origin of the observed large transition and relationship between domain configuration and resistivity as a function of temperature, I performed numerical simulation based on random resistor network model.[13] Here, I supposed a $n \times m$ matrix (n = 1 - 20, m = 2 - 30) where each one of elements represent metal or insulator domain. I gave each domain the transition temperature (Tc) which is randomly set with a probability (f) following Gaussian distribution,[14, 15]

$$f(Tc) = \frac{1}{\sqrt{2\pi\sigma^2}} \exp\left[-\frac{(Tc - Tc^0)^2}{2\sigma^2}\right] \quad (4.1)$$

,where σ is a standard deviation and Tc^0 is a mean value of the distribution and these value were set to reproduce the thin film's RT data. When the set temperature exceeds the domain's Tc, the domain turned to metal from insulator, and then, I calculated the total resistance of the random resistor network system using the Kirchhoff's law [16] at each temperature and resistivity of each domain. To reproduce the resistivity behavior at low temperature, I assumed the Arrhenius type temperature dependence of resistivity for insulator domain.[17] Figure 4.3 shows the comparison between experimentally obtained RT and calculated ones. RT of the thin film is well reproduced at 30 × 30 domain matrix. By applying the same parameters used in the calculation, I reproduced RT for the nanowires, and one of the obtained results for 2 × 4 domain matrix is shown in Fig. 4.3. The multistep behavior is well reproduced in the calculation and the largest change of resistivity corresponds to the case where the metallic conduction path was formed between electrodes. Figure 4.4 shows a Perason's correlation coefficient [18] between RT for the nanowire and calculated results at each domain matrix. With decreasing the size of the matrix, the correlation coefficient becomes scattered even in the same domain configuration because each domain's state

which differs in different calculation run becomes more critical in smaller matrix. Even when the outline of the RT shape is well reproduced by the calculation, correlation coefficient is not always high because high correlation coefficient needs the best match of position and degree of resistance change at same time. But total number of resistivity change and degree of the most prominent transition originating from the formation of conductive path between electrodes does not change so much even in the different calculation run. And the highest correlation coefficient obtained at same domain matrix becomes higher with decreasing the size of the matrix, which gives the information about the probable number of domain included in the device. I compared the experimentally obtained RT curve and calculated ones which show the highest correlation coefficient at the given domain matrix as shown in Fig. 4.5. Considering that over one order of resistivity change can be observed at n = 1 - 3 and the number of steps is over 2, 2 × 4 or 3 × 6 domain matrix is probable to well describe the experimental behavior. The device geometry is 200 nm in width and 400 nm in length, so the single domain size is estimated to be around 70 – 100 nm which is comparable with the reported value using nanoimaging techiniques.[3, 19]

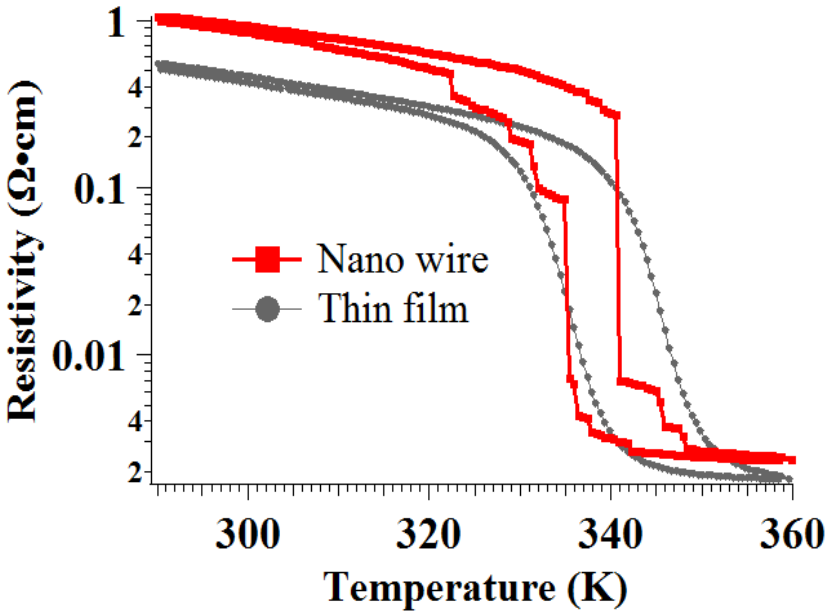

Fig. 4.2 Temperature dependence of resistivity for the VO_2 nanowire (red square with line) and a thin film (gray circle with line)

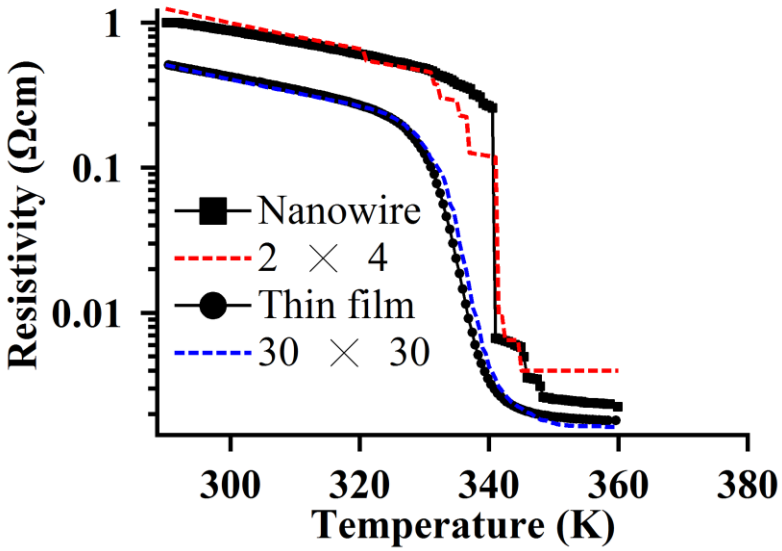

Fig. 4.3 Comparison between experimentally obtained RT and calculated ones using the random resistor network calculation. Experimental data are shown by squre (nanowire) and circle (thin film) and calculated data is shown by red dashed (2 × 4 domain geometry) and blue dashed (30 × 30 domain geometry) line.

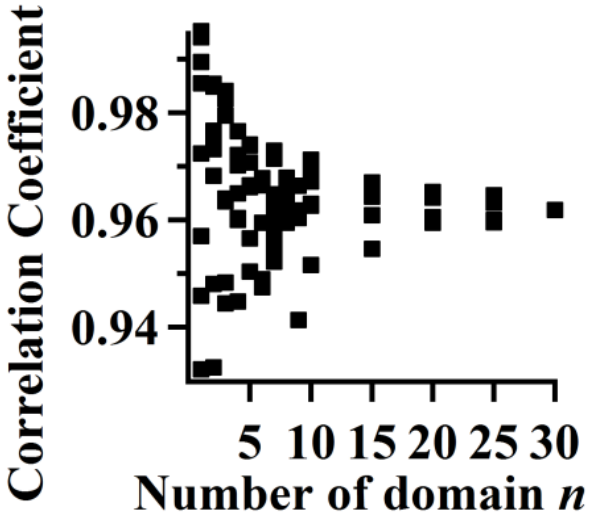

Fig. 4.4 Perason's correlation coefficient between RT for nanowire and calculated result at each domain matrix.

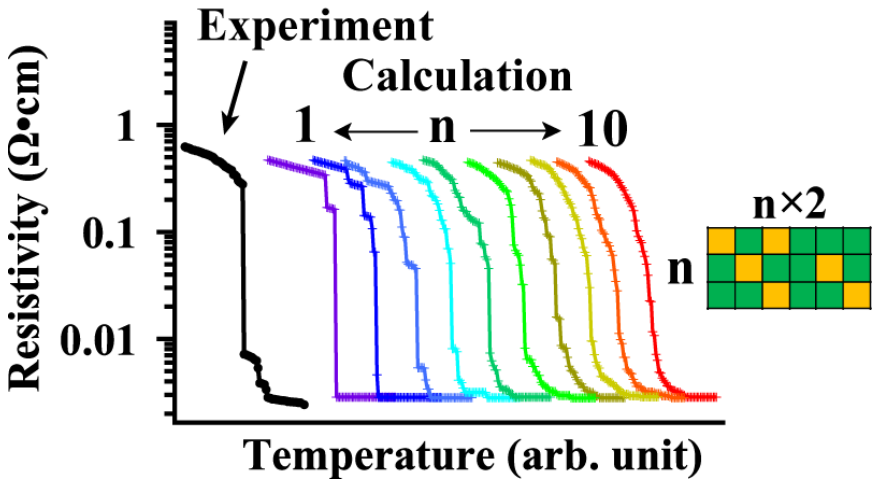

Fig. 4.5 Comparison between experimentally obtained RT for nanowire (black square with line) and simulated RT which shows the highest correlation value at each domain matrix. (colored lines).

Electrical control of multistep MIT is interesting for device application in addition to temperature control. Figure 4.6 shows voltage-induced MIT for the nanowire and thin film sample measured at almost middle temperature point of the hysteresis in RT curve. The nanowire exhibited multistep MIT while the thin film sample shows continuous change of resistivity as observed in temperature-induced case. It is reported that voltage-induced MIT of VO_2 thin films shows 1D-like anisotropic conductive behavior while temperature-induce one is consistent with 2D isotropic percolation model.[11] To investigate the nano-confinement effects to the conductive behavior in nanowires, I compared the resistivity change induced by voltage and temperature for the two devices with different wire width. Figure 4.7(a) shows a temperature dependence of resistivity for the nanowires with a width of 200 nm (device A, left) and 700 nm (device B, right). The values of T_c^0 defined by Eq. 4.1 were set to reproduce the RT curves. Figure 4.7(b) shows resistivity as a function of temperature rise ΔT (blue, top axis) and applied electric power per unit volume p (red, bottom axis) for device A (left) and device B (right) at each stage temperature normalized by the T_c^0. I show the resistivity change in a same range of ΔT and p for the same device based on the results that the local temperature linearly increases with increasing Joule heating in VO_2-based devices.[20] I compared the two curves in the region before the electric breakdown [21] to focus on the resistivity change induced by the single domain MIT. It is observed that the two curves matches well at low temperature insulator region (T / T_c < 0.93) and high temperature metallic region (T / T_c > 1.03). Now, I pay attention to the temperature region from T / T_c = 0.99 - 1.03 where the both phases coexist. In the device B, the resistivity changes more drastically in voltage-induced case than in temperature induced one due to the different conductive behavior as mentioned above. On the other hand, in the device A, the difference between the two curves is suppressed. This seems to be caused by the nano-confinement effect of the nanowire whose conductive behavior becomes 1D-like even in the temperature induced case [10] as shown in Fig. 4.7(c). My results indicate that the dimensionality of domain configuration plays an important role in the electrical control of the multistep MIT of nanowires. To compare the performance of my device with other VO_2 two-terminal devices, Fig. 4.8(a) and (b) shows the on/off ratio per temperature change and electric-power change, respectively..

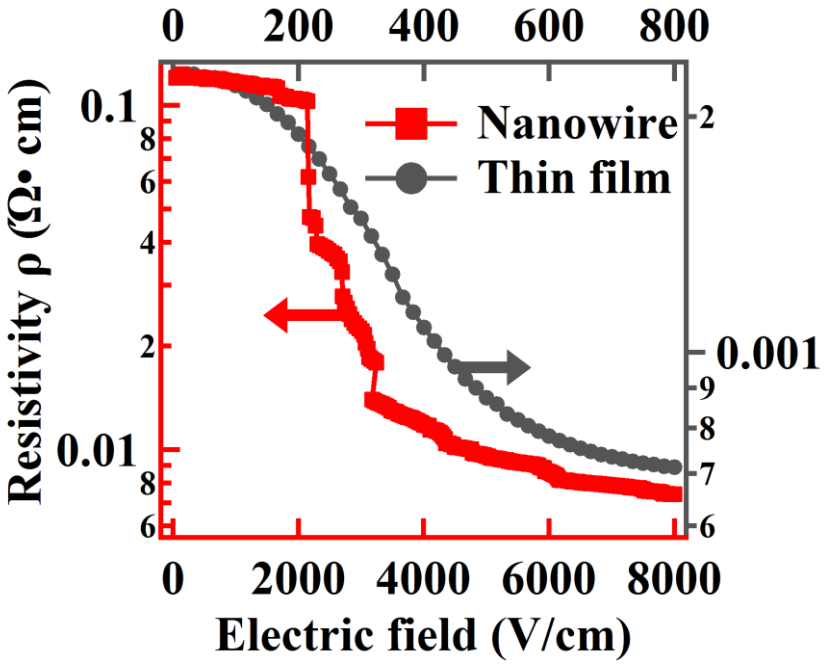

Fig. 4.6 Voltage-induced MIT for VO_2 nanowire (red square with line) and thin film (gray circle with line). Multistep resistivity change can be observed only in the nanowire.

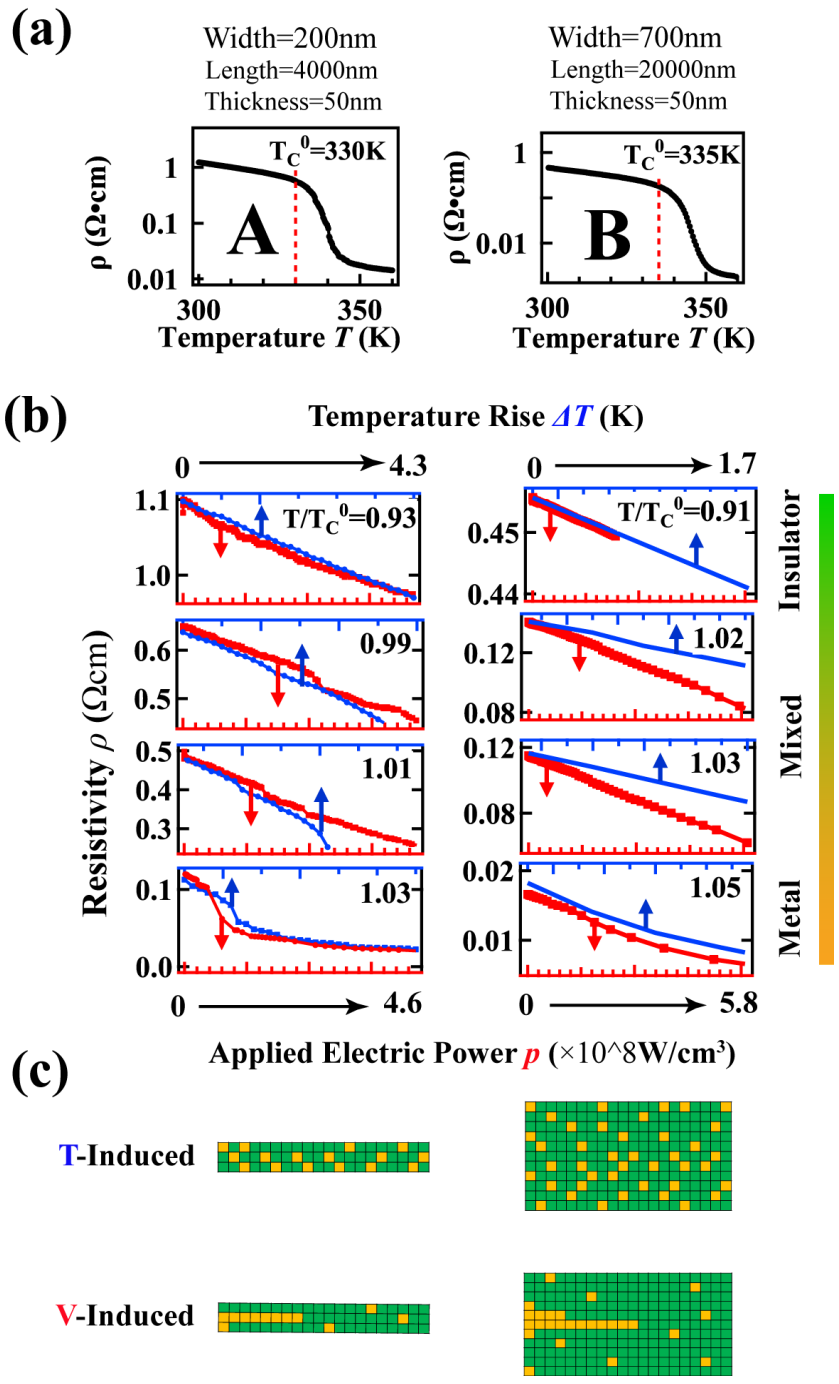

Fig. 4.7 (a) Temperature dependence of resistivity for the nanowire with a width of 200 nm (left, device A) and 700 nm (right, device B). (b) Electrical resistivity as a function of temperature (blue, top axis) and applied electric power per unit volume (red, bottom axis) at each stage temperature for the device A (left) and B (right). (c) Schematic illustration of different conductive behavior between temperature-induced case (up) and voltage-induced case (down) for device A (left) and device B (right)

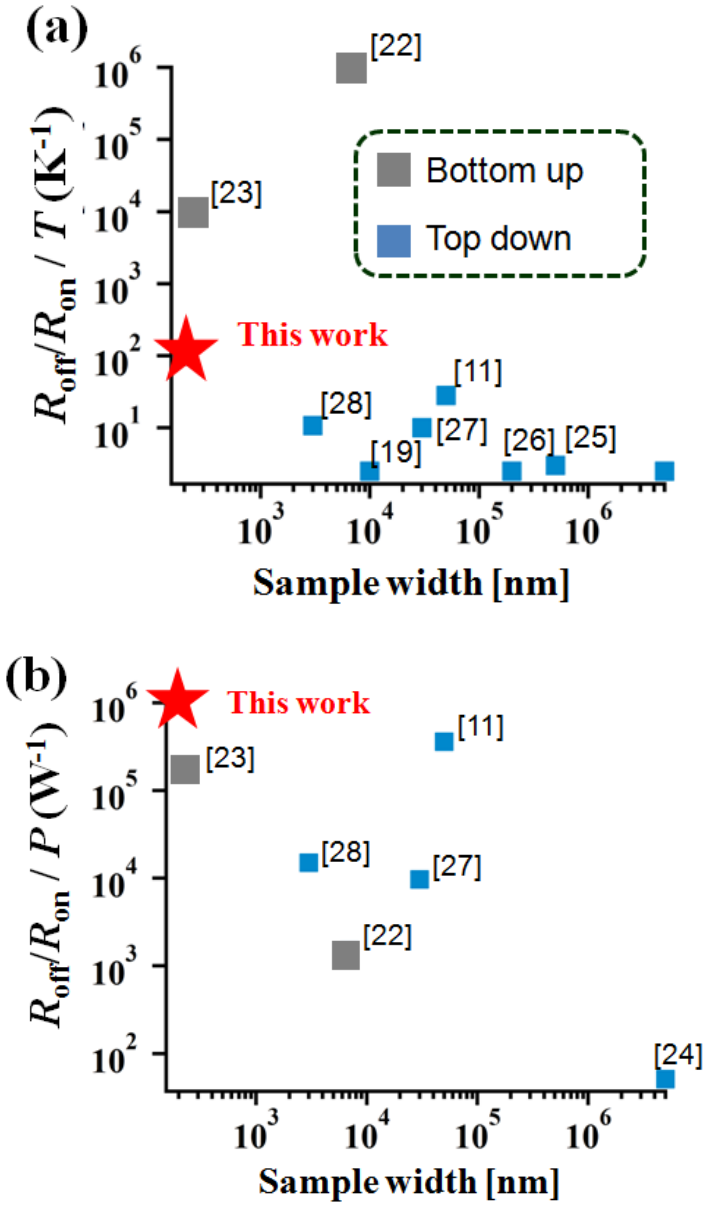

Fig. 4.8 Degree of the resistance change (On/Off ratio) triggered by (a) temperature and (b) electric power for VO_2 two-terminal devices. Among the thin-film-based nanowires, my device shows the highest On/Off ratio with low energy consumption. In addition, my device has an advantage in high controllability of size, shape and position in large area compared with nanowires which are synthesized by using bottom up method like vapor transport method.

4.4 Conclusion

In conclusion, I observed temperature- and voltage-induced multistep MIT in VO_2 nanowires fabricated on Al_2O_3 (0001) substrates by using nanoimprint lithography. The nanowires with 200 nm width shows temperature-induced multistep MIT which include nearly two orders of resistivty change at 0.5 K temperature step. These multstep resistivity jumps can be understood as a single domain's transition in the confined nanostructure, and single domain size is estimated to be 70 – 100 nm. I found the temperature-induced isotropic cunductive behavior becomes similar to the voltage-induced anisotropic one in the nanowire.

4.5 References

[1] F. J. Morin, *Phys. Rev. Lett.* **3** (1959) 34

[2] J. B. Goodenough, *J. Solid State Chem.* **3** (1971) 490

[3] M. M. Qazilbash *et al.*, *Science* **318** (2007) 1750

[4] A. Sharoni, J. Ramírez, I. Schuller, *Phys. Rev. Lett.* **101** (2008) 026404

[5] K. Kawatani, H. Takami, T. Kanki, H. Tanaka, *Appl. Phys. Lett.* **100** (2012) 173112

[6] S. C. Chae *et al.*, *Appl. Phys. Lett.* **95** (2009) 093508

[7] S. Meister, D. T. Schoen, M. A. Topinka, A. M. Minor, Y. Cui, *Nano Lett.* **8** (2008) 4562

[8] H. T. Kim *et al.*, *New J. Phys.* **6** (2004) 52

[9] G. Stefanovich, A. Pergament, D. Stefanovich, *J. Phys. Condens. Matter.* **12** (2000) 8837

[10] H. Takami *et al.*, *Appl. Phys. Lett.* **101** (2012) 263111

[11] T. Kanki, K. Kawatani, H. Takami, H. Tanaka, *Appl. Phys. Lett.* **101** (2012) 243118

[12] H. Ueda, T. Kanki, H. Tanaka, *Appl. Phys. Lett.* **102** (2013) 153106

[13] P. Stoliar *et al.*, *Adv. Mater.* **25** (2013) 3222

[14] M. S. S. Challa, D. P. Landau, K. Binder, *Phys. Rev. B* **34** (1986) 1841

[15] V. A. Klimov *et al.*, *Tech. Phys.* **47** (2002) 1134

[16] J. P. Straley, *Phys. Rev. B* **15** (1977) 5733

[17] C. Chen *et al.*, *J. Appl. Phys.* **110** (2011) 023707

[18] B. G. Hane, K. Jager, H. G. Drexler, *Electrophoresis* **14** (1993) 967

[19] J. Kim, C. Ko, A. Frenzel, S. Ramanathan, J. E. Hoffman, *Appl. Phys. Lett.* **96** (2010) 213106

[20] A. Zimmers *et al.*, *Phys. Rev. Lett.* **110** (2013) 056601

[21] A. Shekhawat, S. Papanikolaou, S. Zapperi, J. P. Sethna, *Phys. Rev. Lett.* **107** (2011) 276401

[22] Q. Gu, A. Falk, J. Wu, L. Ouyang, H. Park, *Nano Lett.* **7** (2007) 363

[23] A. Tselev *et al.*, *Nano Lett.* **11** (2011) 3065

[24] G. Adam, *Appl. Phys. Lett.* **19** (1971) 115

[25] T. Driscoll *et al.*, *Appl. Phys. Lett.* **95** (2009) 043503

[26] Y. W. Lee *et al.*, *Appl. Phys. Lett.* **92** (2008) 162903

[27] N. Manca *et al.*, *Adv. Mater.* **25** (2013) 6430

[28] L. Pellegrino *et al.*, *Adv. Mater.* **24** (2012) 2929

CHAPTER 5

Thermoelectric control of reversible metal-insulator transition of single electronic domain in VO_2 nanowires.

Phase separation in strongly correlated electron materials naturally forms electronic phase boundary contacting with different type of physical characteristics such as metallic and insulating phases. This unique interface provides a new route to manipulate the correlated electron phases. Here I demonstrate electric bias-control of MIT using thermoelectric effects at the interface of metal and insulator domains in VO_2 nanowire-based two terminal devices on Al_2O_3 (0001) substrates. This operation shows entirely reversible and memristive switching between metallic and insulating states of a domain. The single domain's MIT event is enough observable in the VO_2 nanowire with 120 nm in width. Furthermore, one dimensional domain configuration in the VO_2 nanowire enable to control the thermoelectric cooling and heating to induce the MIT.

5.1 Introduction

Electronic phase transition in strongly correlated electron systems has been attracting much attention due to its drastic change of physical properties by external stimuli such as electrical, optical, structural, chemical, magnetic and thermal effects [1-6]. In the vicinity of the phase transition point, some of these materials show mixed electronic phases [2, 7-10]. The electronic phases spatially separate with puddle or stripe shapes, spontaneously forming electronic interface at the boundary of different type of phases in a material. This unique interface should provide new opportunity for development of fascinating functionalities, which is entirely different from the conventional rigid hetro-junction composed of two different materials [5, 11-13].

VO_2 is one of the typical example which shows a first order phase transition between high temperature metallic state and low temperature insulating one with drastic change of resistance at 340 K.[14, 15] In the vicinity of the MIT temperature, VO_2 shows mixed electronic phases consisting of metal and insulator domains whose size ranges from several micro- to nanometers.[7, 16] When the sample size is reduced to the single domain's one, the first order phase transition of individual domains can be observed as multistep change of resistivity.[17] Thus, VO_2 micro- or nanostructure have full potential to control the single domain's MIT.[18-20] Against easy control of the insulator-to-metal (I-to-M) transition by the self-Joule heating due to an electric

bias,[21] the control of metal-to-insulator (M-to-I) transition remains a challenging and longstanding issue. To induce the M-to-I transition, it is necessary to cool down temperature or to control a number of carriers [22] in VO_2. Recently, reversible transition between M-to-I and I-to-M was demonstrated by using three terminal devices in VO_2 thin films with an ionic liquid gate by accumulating a large number of carriers [23, 24] and/or inducing oxygen atom migration [25]. However, complex chemical phenomena [25] and low speed operation [23] of the ionic liquid-based devices hamper its application to the next generation solid-state-devices. Here I demonstrate more speedy and handy reversible control of the MIT by an electric bias using simple two-terminal nano-wire devices. Thermoelectric effect including Peltier effect is one of the promising candidates to reversibly control the MIT. The Peltier effect has fully potential to exert cooling and heating action through the electronic interface in contact with two electronic phases which have different Seebeck coefficient [26]. The Seebeck coefficient of metallic and insulating phase in VO_2 is widely different [27, 28], thus large Peltier effect that can induce the MIT is expected at the interface.

First I suggest the theoretical model for electric current-induced M-to-I as well as I-to-M transition by using the thermoelectric effect at the interface between metallic and insulating phases in VO_2. Figure 5.1(a) shows a schematic model for the thermoelectric effect at the metal-insulator domain boundary. In the equilibrium state, the heat balance can be described as follows [29];

$$-\boldsymbol{Q_P} + \boldsymbol{Q_D^I} + \boldsymbol{Q_D^M} + \boldsymbol{Q_J^I}/\mathbf{2} + \boldsymbol{Q_J^M}/\mathbf{2} + \boldsymbol{Q} = \mathbf{0}, \tag{5.1}$$

$$\boldsymbol{Q_P} = \boldsymbol{\Pi_{IM} iA} = (\boldsymbol{S_I} - \boldsymbol{S_M})\boldsymbol{T_B^{IM} iA}, \tag{5.2}$$

$$\boldsymbol{Q_D^j} = \boldsymbol{\lambda^j \frac{A}{L}(T_S - T_B^{IM})} \quad , \text{ j = I or M}, \tag{5.3}$$

$$\boldsymbol{Q_J^j} = \boldsymbol{\rho^j i^2 LA} \quad , \text{ j = I or M}, \tag{5.4}$$

$$\boldsymbol{Q} = \boldsymbol{qA}. \tag{5.5}$$

$\boldsymbol{Q_P}$ is the heating value absorbed by the endothermic Peltier effect. $\boldsymbol{Q_D^I}$ and $\boldsymbol{Q_D^M}$ are the heating values diffusing into metal and insulator domain, respectively, which is generated by the difference between an ambient temperature and the temperature altered by the Peltier effect at the interface ($\boldsymbol{T_S - T_B^{IM}}$). $\boldsymbol{Q_J^I}$ and $\boldsymbol{Q_J^M}$ is the heating value generated by the Joule effect at insulator and metal domains, respectively. $\boldsymbol{Q}$ is the

heating value diffusing into the air and substrates. $\boldsymbol{\Pi_{IM}}$ is the Peltier coefficient at metal-insulator domain boundary. i is the current density and A represents the cross section area of the interface. S_I and S_M are the Seebeck coefficients of insulating and metallic states in VO_2, whose values used in this calculation are 400 μV/K and 18 μV/K, respectively [27]. T_S is the ambient temperature measured by a thermocouple mounted in a sample stage. $\boldsymbol{\lambda^I}$ and $\boldsymbol{\lambda^M}$ are the heat conductivity for insulating and metallic states, respectively. L is the length of the domains. $\boldsymbol{\rho^I}$ and $\boldsymbol{\rho^M}$ are the resistivity for insulating and metallic states, respectively. q is the heating value absorbed from the ambience per unit cross section. Using the Eqs. 5.1 - 5.5 and the experimentally identified condition, that is, $S = S_I >> S_M$, $\boldsymbol{\rho = \rho^I >> \rho^M}$, $\boldsymbol{\lambda = \lambda^I \cong \lambda^M}$, I can obtain the temperature difference, $\boldsymbol{T_B^{IM} - T_S}$, at the interface between insulating and metallic domains as shown in Fig. 5.1(b) as a function of current density as a following simplified form;

$$\boldsymbol{T_B^{IM} - T_S = \frac{1}{Si+\frac{2\lambda}{L}}\left(q - ST_S i + \frac{\rho L}{2} i^2\right)}. \quad (5.6)$$

The second term of Eq. 5.6 represents the Peltier effect-induced temperature change whose positive or negative sign depends on the current direction, while the third term represents the Joule heat-induced temperature increase whose sign is constantly positive. Owing to the Peltier cooling in the second term, the temperature at the interface can decrease down to the M-to-I transition temperature in a domain. This is the basic concept of thermoelectric control of M-to-I transition. In the case of the interface at insulator-insulator domains as shown in right illustration of Fig. 5.1(b), on the other hand, Peltier effect disappears and the difference between the T_S and the temperature of the insulator-insulator interface ($\boldsymbol{T_B^{II} - T_S}$) can be described as follow;

$$\boldsymbol{T_B^{II} - T_S = \frac{L}{2\lambda}\left(q + \rho L i^2\right)}. \quad (5.7)$$

Thus, I can establish reversible metal-insulator switching using Eq. 5.6 and 5.7. Figure 5.1(c) shows illustration of first order MIT in a single domain. The scenario for the reversible MIT control is simple, that is, whether the interface temperature changes by the thermoelectric effect can approach down to the M-to-I transition temperature (T_L) and up to the I-to-M one (T_H) from the T_S. Figure 5.1(d) shows theoretical curves of temperature modulation when applying current bias i in the case of the insulator-metal interface (red curve) in Eq. 5.6 and the

insulator-insulator interface (blue curve) in Eq. 5.7, assuming the adiabatic process (q = 0) which gives the most effective temperature-drop by the Peltier cooling effect. Given T_S is set to be within a temperature hysteresis in a single domain as shown in Fig. 5.1(c). In Fig. 5.1(d), the initial state of the domain is metal (Point ①), $\boldsymbol{T_B^{IM} - T_S}$ decreases along the red curve down to the ②, reaching the T_L, with increasing i crossing the interface from insulating to metallic phases. Then, M-to-I transition is invoked and the theoretical curve that I focus on moves to the ③ on the blue curve. Even when i returns to zero at the ④, insulator states is maintained. When i increases to the direction from right to left in Fig. 5.1(b), $\boldsymbol{T_B^{II} - T_S}$ increases up to the ⑤ at the T_H, invoking I-to-M transition. Then the curve that I focus on moves to the red curve again and the state returns to the initial ① at zero current. A series of this process by controlling current density and the direction leads to the reversible and memristive resistive switching as shown in Fig. 5.1(e). Experimentally to obtain this controllability of the MIT in a single domain by the current bias, one dimensional domain-configuration should be required.

5.2 Experimental

As it was revealed in chapter 4, the single domain's size of VO_2 on Al_2O_3 (0001) substrate was estimated to be 70 – 100 nm [17], thus, VO_2 nano-wires having a width of approximately the comparable size of domains would be necessary to observe the single domain's behavior. The fabrication procedure and measurement method in the nano-wires has been well described in chapter 3 and 4.

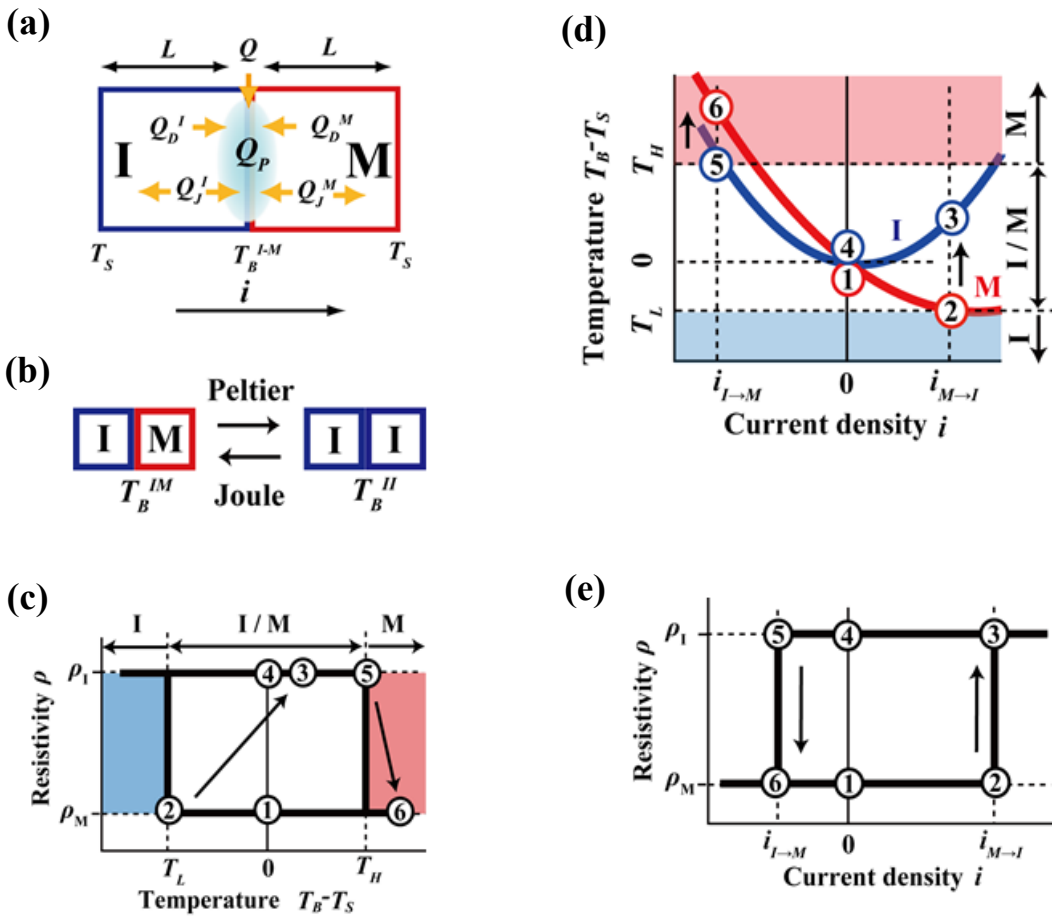

Fig. 5.1 Theoretical model for the current control of metal-to-insulator and insulator-to-metal transition by using thermoelectric effect at an interface between metallic and insulating domain of VO_2. (a) Schematic model of thermoelectric effect at an interface between metallic and insulating phases. (b) The two states switched by Peltier cooling effect from I-M to I-I domain configuration and reversely changed by Joule heating effect. (c) Temperature dependence of resistivity of the single domain. (d) Current density dependence of a temperature change of the interface for I-M (red) and I-I (blue) states. (e) Current density dependence of resistivity for the switched domain.

5.3 Results and Discussion

Figure 5.2 shows a temperature dependence of resistivity in a VO_2 nano-wire having 120 nm in width (red square) and thin film (blue circle). The inset shows a scanning electron microscope image of the nanowire. First order MIT of each individual domain can be observed in the nanowire.[17] Figure 5.3 shows a resistive behavior when applying a current bias in the lower resistive side within the hysteresis in the cooling process in three nanowire devices (D1 – D3) (colored dots with lines) and in a thin film (black line), respectively. Discrete and large resistance increases are observable by applying current bias in VO_2 nano-wires within the temperature hysteresis region. This notable behavior cannot be explained by the conventional Joule heat [21] or electric breakdown model [30], and not observed in the thin film and out of the hysteresis region (See Fig. 5.4). Thus, this resistance increase can be attributed to the Peltier-cooling-induced M-to-I transition of a single domain.

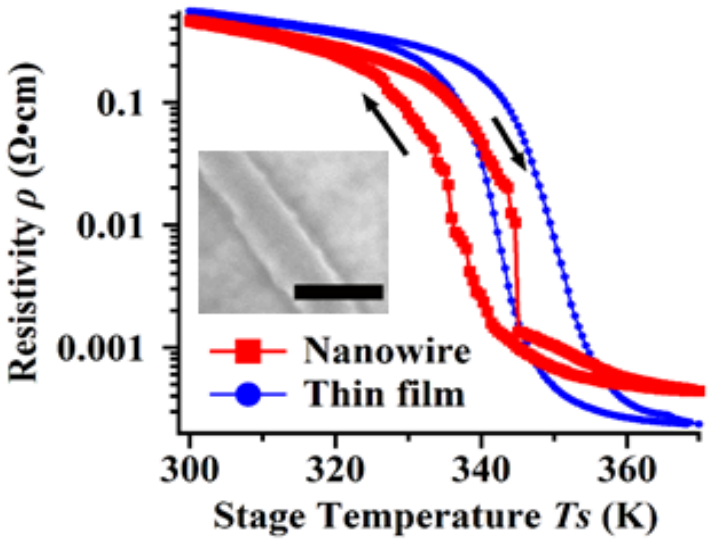

Fig. 5.2 Temperature dependence of resistivity for a nanowire (red square) and a thin film (blue circle). Inset shows a SEM image of the measured nanowire. Scale bar is 200 nm

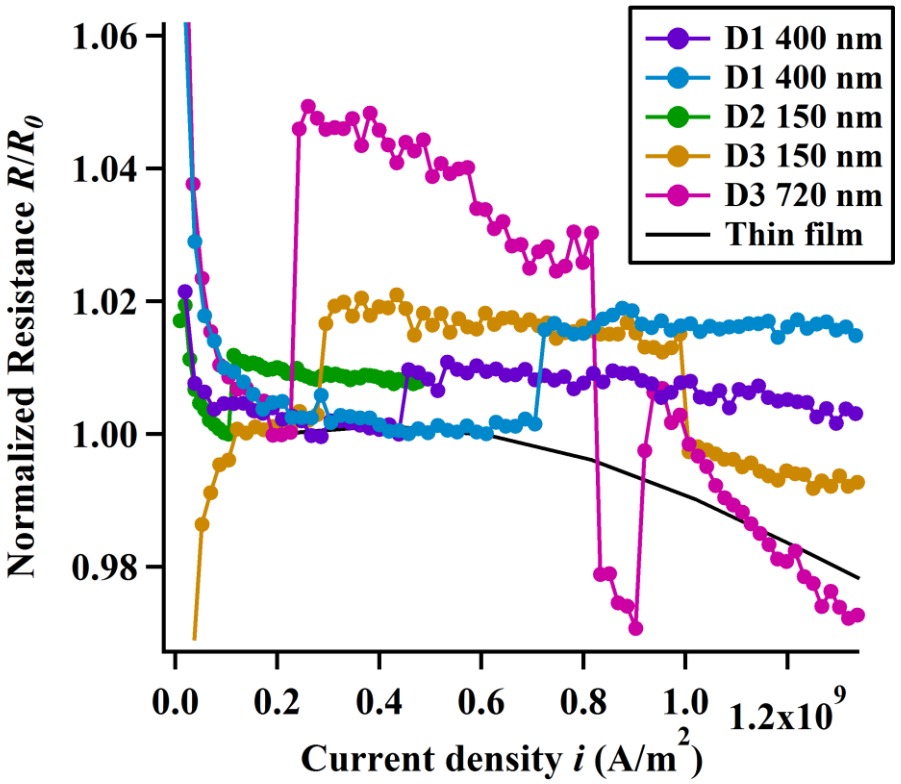

Fig. 5.3 Current density dependence of normalized resistivity for nanowires (colored dot with lines) thin film (black line) within the hysteresis in the cooling process. Device geometries of device 1, device 2, device 3 (D1, D2, D3) is 400, 150, 720 nm in width, 2.5, 2.7, 1.6 μm in length, 70, 70, 80 nm in thickness, respectively.

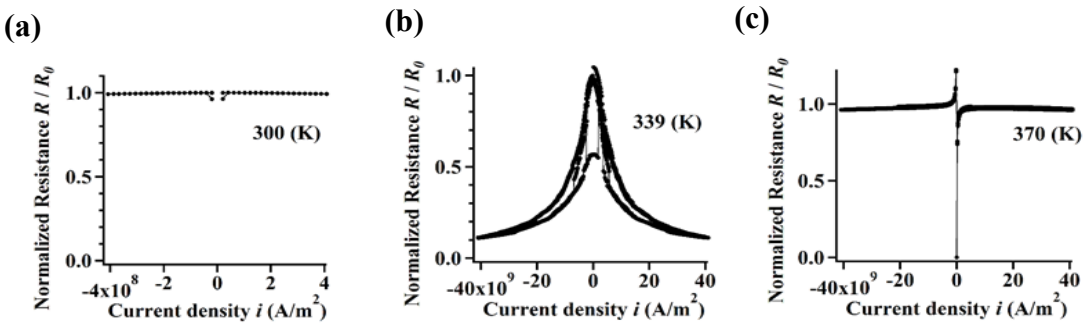

Fig. 5.4 Current density dependence of normalized resistance at 300 K (a), 339 K (b) and 370 K (c). Multistep MIT can be observed only in the hysteresis region in Fig. 5.2.

Figure 5.5(a) shows a current density dependence of resistance for a nanowire. Initially, the resistive state starts from a lower metallic state at the ①. When i increases, the resistance discretely jumps from the ② to the ③ at $i = 1.8\times10^9$ A/m^2. This resistance state is kept even at the zero bias at the ④. This process corresponds to the theoretical points from ① to ④ in Fig. 5.1(c), (d), and (e). Resistance decrease below $i = 1\times10^9$ A/m^2 is extrinsic behavior which may be due to the thermoelectric voltage induced by the local temperature difference in the nanowire. Inset shows the result for the backward current scan after the forward current scan as shown in the main graph. At $i = -5.2\times10^9$ A/m^2, discrete resistivity drop was observed as theoretically predicted in Fig. 5.1(e). This resistivity state was kept at zero bias although the resistivity behaves out of the theory on the way from the ⑥ to ①, which seems to be caused by an uncontrollable thermoelectric effect originating from the complex shape and configuration of domains, which may give unpredictable current distribution in the nanowire [7, 16]. Figure 5.5(b) shows the time dependence of resistance state derived from the result of the inset in Fig. 5.5(a). It can be clearly seen that the non-volatile and reversible MIT was achieved only by tuning the current. To quantitatively justify my theoretical model, Fig. 5.5(c) shows the graph derived from Eq. 5.6 and 5.7 by substituting the parameters obtained from my experiment and previously reported data. The used value of the parameters are $\rho = 0.1$ Ωcm, $L = 50$ nm, $\lambda = 3.5$ W/mK [31], $S = 400$ μV/K [27], $T_S = 340$ K. [32]. $i_{M\rightarrow I}$ and $i_{I\rightarrow M}$ is set to be the same value observed in the inset of Fig. 5.5(a). According to the Fig. 5.5(c), the local temperature at the interface of metal-insulator domains decreases by -1.3 K at ② and increased by 9.4 K at ⑤, meaning the temperature hysteresis window of the switched domain is about 10 K, which is approximately a comparable value considering the hysteretic character of VO_2 [33]. The reproducibility of the thermoelectric control was guaranteed by other measurements (See Fig. 5.6).

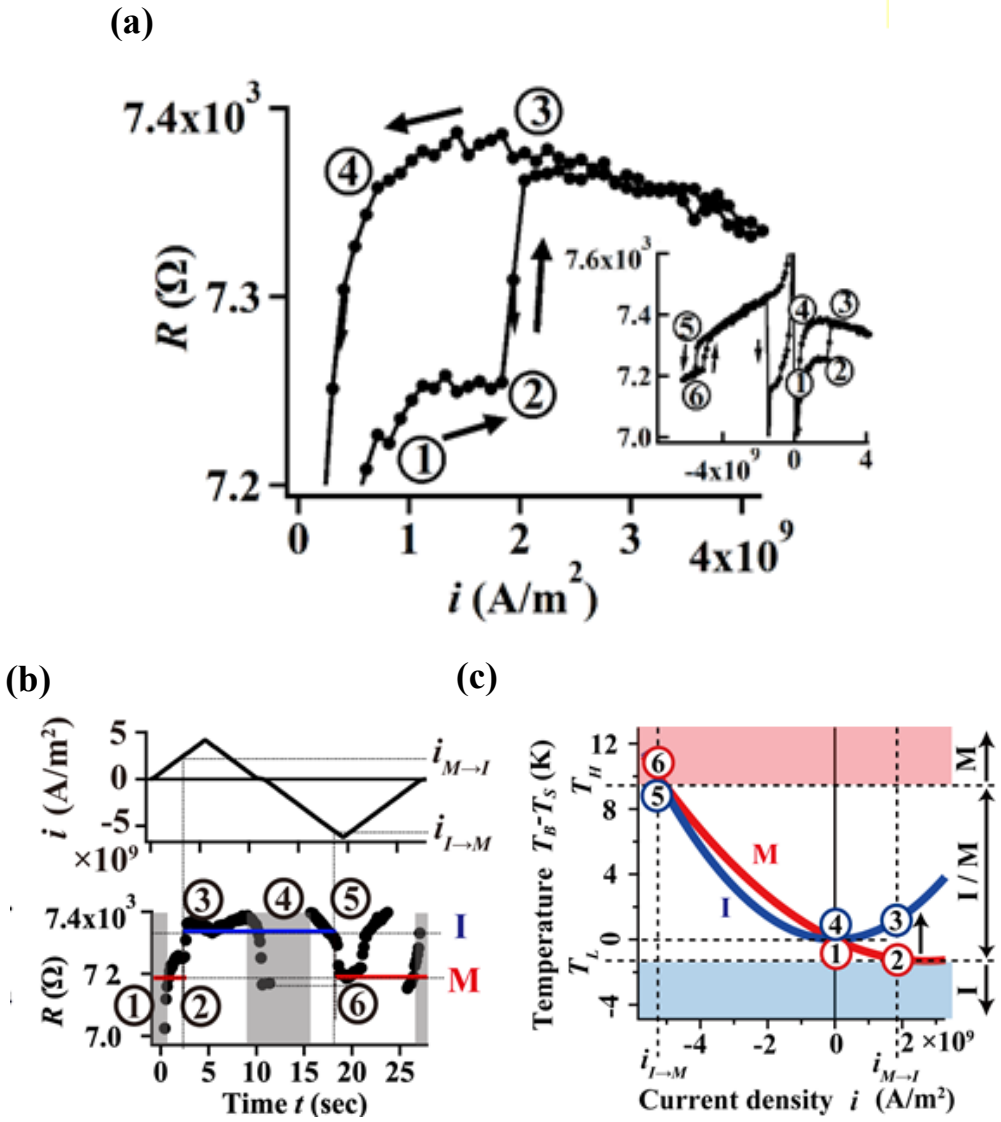

Fig. 5.5 Non-volatile metal-to-insulator transition driven by the current sweep. (a) Current density dependence of resistance for a 120 nm-wide nanowire. Inset shows the result for forward (also shown in main graph) and backward scan of current. (b) Time dependence of resistance derived from the result of the inset of Fig. 5.5(a). Shaded areas corresponds to the low voltage region which seems to be strongly affected by the thermoelectric voltage. (c) Quantitative estimation of the boundary temperature as a function of current density. $i_{M\rightarrow I}$ is set to be the current at ② and $i_{I\rightarrow M}$ is set to be the current at ⑤ in the inset of Fig. 5.5(a).

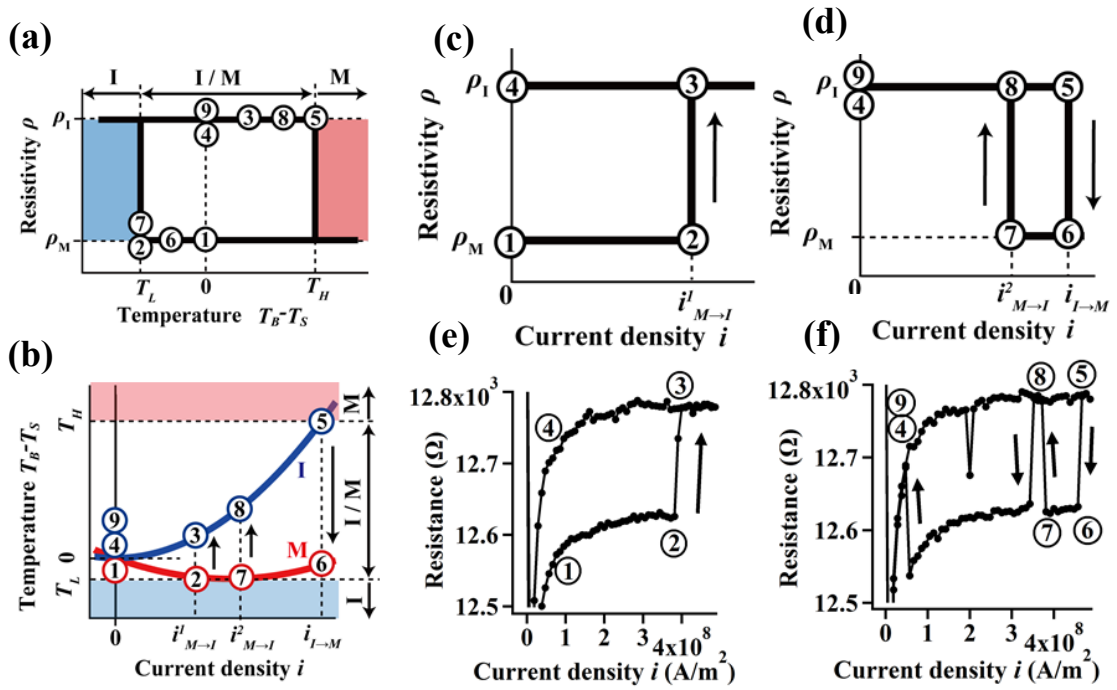

Fig. 5.6 Demonstration for the M-to-I and I-to-M transition by tuning the current flowing in the same direction. (a) Temperature dependence of resistivity for the controlled single domain. (b) Current density dependence of interface temperature. Each number corresponds to the same number's state as shown in Fig. 5.6(a). (c, d) Theoretically estimated current density dependence of resistivity for the single domain in first (c) and second (d) current sweep with same sweep direction. (e, f) Experimentally obtained current density dependence of resistance for a VO_2 nanowire in first (e) and second (f) current sweep. The device has 150 nm in width, 2.7 μm in length and 70 nm in thickness. Theoretically predicted resistance behavior was experimentally demonstrated except for the resistance fluctuation on the way from ⑧ to ⑨ in Fig. 5.6(f).

In my scenario, another two kinds of resistance behavior can be predicted, the one is oscillation mode as shown in the case 1 of Fig. 5.7(a) and the other is no-transition mode as shown in the case 2 of Fig. 5.7(a). In the former case, T_S is set as ① to locate ② (minimum point of red curve) in the insulating states and ③ in the metallic states, respectively. When the M-to-I transition occurs at ②, Joule heating starts to occur resulting in the temperature increase above the T_H. Then, I-to-M transition occurs at ③ and it returns to M state at ② where the M-to-I transition occurs again. These process should be repeated and can be seen experimentally as the resistance oscillation. In the latter case, when *Ts* is set as ① to locate ② within the temperature hysteresis, the M-to-I transition does not occur. To experimentally prove this scenario, I appropriately set the T_S. Figure 5.7(b) shows the resistance behavior when applying current bias at the T_S in the two cases. Theoretically predicted resistance oscillation was clearly observed at *Ts* = 339 K (blue) and 340 K (green), and these oscillation disappeared at *Ts* = 341 K (orange). The resistance oscillation is observable only when inducing the Peltier cooling effect by a current direction crossing metal-to-insulating domains. The reverse direction current cannot induce the oscillation mode (see Fig. 5.8). Thus the thermoelectric effect significantly acts on a single domain MIT in VO_2 nanodevices. This result will lead the new way to control of electronic phases in correlated electron materials.

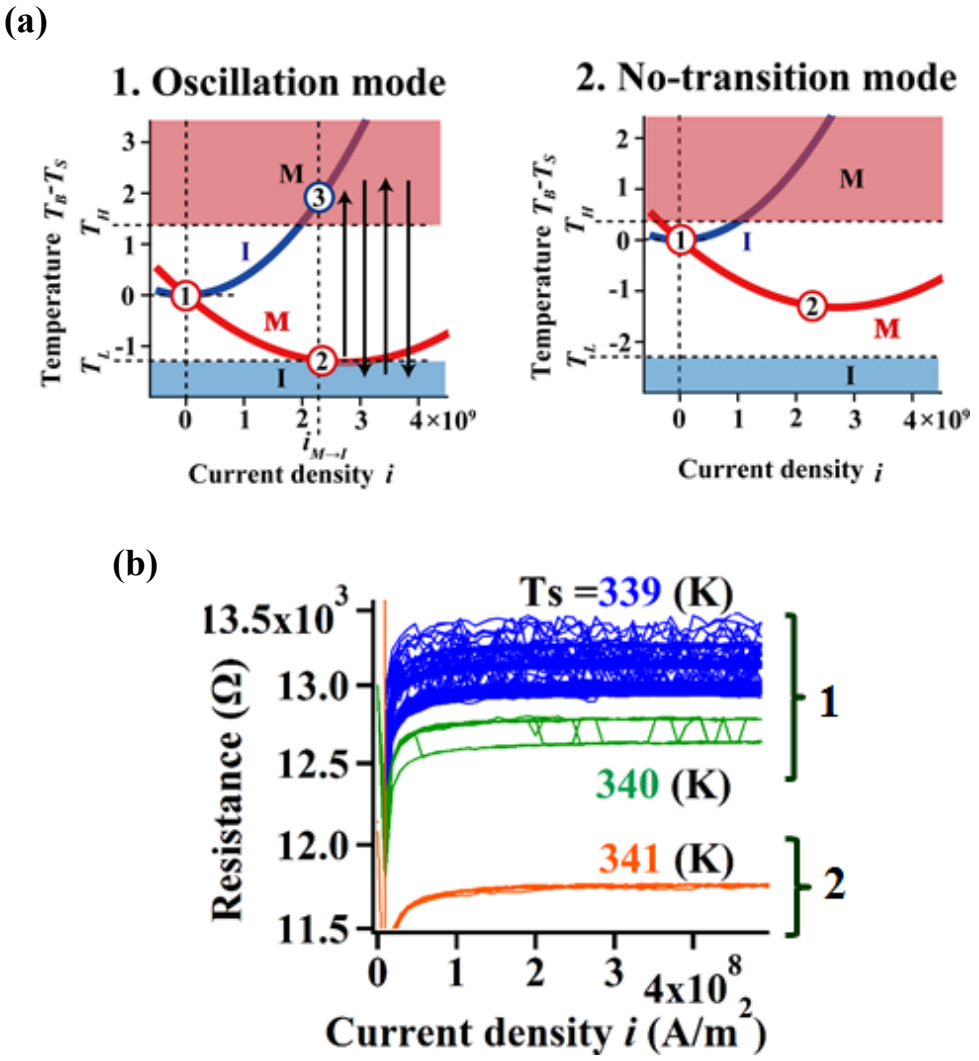

Fig. 5.7 Temperature influence for the resistance oscillation (a) Current density dependence of the interface temperature for oscillation mode (case 1) and no-transition mode (case 2). (b) Current density dependence of resistance for T_S is 339 K (blue) and 340 K (green) and 341 K (orange).

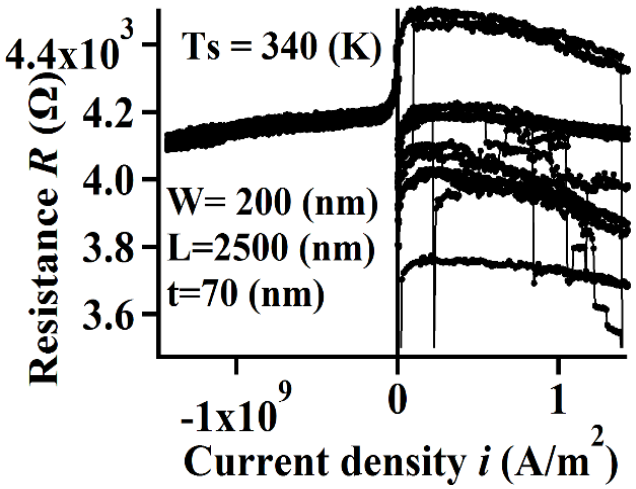

Fig. 5.8 Current density dependence of resistance for different current sweep direction. In the forward current sweep, resistance shows the unstable and discrete fluctuation which disappears in the backward current sweep.

5.4 Conclusion

In conclusion, I electrically controlled metal-to-insulator transition of a nano-scale domain by using Peltier cooling effects at an interface between metallic and insulating electronic phases in the coexistence states in VO_2 nano-wire-based two-terminal devices. The electronic phase interface is natually formed in the coexistence state in strongly correlated electron materials. I theoritically and experimentally found that this unique interface provides a new route to manipurate reversible metal-insulator transition.

5.5 References

[1] M. Imada, A. Fujimori, Y. Tokura, *Rev. Mod. Phys.* **70** (1998) 1039

[2] E. Dagotto, *Science* **309** (2005) 257

[3] P. Limelette *et al.*, *Science* **302** (2003) 89

[4] A. Lanzara *et al.*, *Nature* **412** (2001) 510

[5] H. Takagi, H. Y. Hwang, *Science* **327** (2010) 1601

[6] M. Jaime *et al.*, *Appl. Phys. Lett.* **68** (1996) 1576

[7] M. M. Qazilbash *et al.*, *Science* **318** (2007) 1750

[8] M. Uehara, S. Mori, C. H. Chen, S. W. Cheong, *Nature* **399** (1999) 560

[9] M. Vershinin *et al.*, *Science* **303** (2004) 1995

[10] J. T. Park *et al.*, *Phys. Rev. Lett.* **102** (2009) 117006

[11] A. Ohtomo, D. A. Muller, J. L. Grazul, H. Y. Hwang, *Nature* **419** (2002) 378

[12] C. H. Ahn, K. M. Rabe, J. M. Triscone, *Science* **303** (2004) 488

[13] G. J. Snyder, E. S. Toberer, *Nat. Mater.* **7** (2008) 105

[14] F. J. Morin, *Phys. Rev. Lett.* **3** (1959) 34

[15] J. B. Goodenough, *J. Solid State Chem.* **3** (1971) 490

[16] J. Kim, C. Ko, A. Frenzel, S. Ramanathan, J. E. Hoffman, *Appl. Phys. Lett.* **96** (2010) 213106

[17] H. Takami, T. Kanki, H. Tanaka, *Appl. Phys. Lett.* **104** (2014) 023104

[18] A. Sharoni, J. Ramírez, I. Schuller, *Phys. Rev. Lett.* **101** (2008) 026404

[19] H. Ueda, T. Kanki, H. Tanaka, *Appl. Phys. Lett.* **102** (2013) 153106

[20] J. Wei, Z. H. Wang, W. Chen, D. H. Cobden, *Nat. Nanotechnol.* **4** (2009) 420

[21] A. Zimmers *et al.*, *Phys. Rev. Lett.* **110** (2013) 056601

[22] H. T. Kim *et al.*, *New J. Phys.* **6** (2004) 52

[23] M. Nakano *et al.*, *Nature* **487** (2012) 459

[24] N. F. Quackenbush *et al.*, *Nano Lett.* **13** (2013) 4857

[25] J. Jeong *et al.*, *Science* **339** (2013) 1402

[26] F. J. DiSalvo, *Science* **285** (1999) 703

[27] J. Cao, W. Fan, H. Zheng, J. Wu, *Nano Lett.* **9** (2009) 4001

[28] C. N. Berglund, H. J. Guggenheim, *Phys. Rev.* **185** (1969) 1022

[29] D. M. Rowe, *Thermoelectrics handbook : macro to nano*. (CRC/Taylor & Francis, Florida, 2006), pp. 1-6.

[30] A. Shekhawat, S. Papanikolaou, S. Zapperi, J. P. Sethna, *Phys. Rev. Lett.* **107** (2011) 276401

[31] H. Wen *et al.*, *Phys. Rev. B* **88** (2013) 165424

[32] W. Martienssen, H. Warlimont, *Springer Handbook of Condensed Matter and Materials Data*. (Springer, Berlin Heidelberg, 2005), p. 438.

[33] M. Gurvitch, S. Luryi, A. Polyakov, A. Shabalov, *J. Appl. Phys.* **106** (2009) 104504

CHAPTER 6

General conclusion

I realized and electrically controlled huge MIT originating from the MIT of the spatially confined single electronic phase by fabricating VO_2 nanostructures.

In chapter 3, I have developed NIL combined with PLD to realize VO_2 nanowires. Systematically size-controlled nanowires were fabricated in large area around 3 × 3 mm^2 on single crystal Al_2O_3 (0001) and TiO_2 (001) substrates. By optimizing the fabrication condition, I achieved to fabricate 30 nm-width wire. Furthermore, I investigated size-effect of dimensionality of the VO_2 system from the view point of domain geometry and electric properties of VO_2 microwires on TiO_2 (001) substrates which shows giant electronic domain whose size is around several or several tens of micrometers. With reducing the width of the microwires, I found the dimensionality of domain configuration changed from 2D to 1D at threshold width of 15μm which corresponds to the domain size. By combing optical observation and electric measurement, I clarify the strong relationship between domain geometry and electric properties. I found the conduction properties of the VO_2 on TiO_2 (001) microwires also changed from 2D pecolation to 1D serial resistor model, which shows an important role of the domain in transport characteristic of VO_2. In chapter 4, I observed multistep MIT with discrete change of resistivity as a function of temperature and voltage in VO_2 nanostructure on Al_2O_3 (0001) single crystal substrate. Especially for the nanowire with 200 nm in width and 400 nm in length, nearly two orders of magnitude change of resistivity originating from single domain's MIT was observed. I performed two dimensional random resistor network calculation to elucidate the origin of the sharp and huge transition. Simulation results showed that the degree of resistance change at each temperature step of 0.5 K rapidly increase with decreasing the width of the nanowires. These results indicate that multistep MIT observed in VO_2 nanowires is attributed to the transition of single electronic domain. By comparing the experimental data and calculating one, I estimated a single domain size to be around 70 - 100 nm which is comparable with previously estimated size observed by using nanoimaging technique. In addition, I demonstrated the voltage-induced multistep MIT as well as temperature-induced one, and temperature-induced isotropic cunductive behavior becomes similar to the voltage-induced anisotropic one with decreasing the width of nanowires. Then, I found these giant multistep MIT originated from spatially confined nanoelectronic domain by fabricating VO_2 nanostructures. In chapter 5, I demonstrated thermoelectric control of single domain's M-to-I for the first time as well as I-to-M transition in VO_2 nanowire. By tuning the flowing current passing through the metal-insulator domain boundary, I was able to control the M-to-I and I-to-M transition

as well as the oscillation between the two states. These results pave the way to the artificial control of single domain's MIT with large change of physical properties toward the non-volatile memory application.

Through a series of experiments in this thesis, I demonstrated the importance of fabricating oxide nanostructures to enhance and electrically control the non-linear physical properties with spatially inhomogeneous electronic phase. This work will bring about the breakthrough in oxide nanoelectronics toward artificial control of single electronic phase with fruitful functionalities.

CHAPTER 7

Appendix

7.1 High temperature-coefficient of resistance at room temperature in W-doped VO_2 thin films on Al_2O_3 substrate and their thickness dependence

The temperature coefficient of resistance (TCR) in $V_{1-x}W_xO_2$ (VWO) with various W-doping levels and thicknesses were investigated on Al_2O_3 (0001) single crystal substrates. The VWO thin films with an appropriate doping level (x = 0.015) showed high TCR over 10 %/K just at room temperature (300 K), which was larger than that in other reported high TCR materials. Moreover, no significant change of the TCR property was found based on their thickness dependence, meaning effective enhancement of the sensing performance for bolometric application.

7.1.1 Introduction

Vanadium dioxide (VO_2) has electronically attractive property, and shows orders-of-magnitude changes in resistivity at around 340 K. These changes are accompanied by a structural deformation between the monoclinic insulating phase at low temperature and the rutile metallic phase at high temperature [1]. From a practical point of view, the abrupt change of resistivity in this material is applicable to uncooled bolometers [2-4]. As one of the performance indexes, the temperature coefficient of resistance (TCR), defined as $(1/\rho)(d\rho/dT)$, is applied [5]. The TCR value of VO_2 is usually over 70 %/K. However, the maximum value of TCR is obtained only in a high temperature region around 340 K. Moreover, the first-order phase transition makes it inconvenient for application in practical devices because of the narrow temperature range of the high TCR. In order to obtain practical bolometric applications working at a wide range around room temperature (RT), VO_x with oxygen vacancy is usually employed. However, the decrease of T_{MI} due to the vacancies is accompanied by a serious decrease of TCR [6].Therefore, it is strongly desired to effectively decrease the metal-insulator transition temperature (T_{MI}) to make the transition occur at RT while suppressing the dramatic decrease of TCR. Dopant-control into mother VO_2 materials is one of the promising methods. It is known that T_{MI} is reduced by doping transition-metal elements such as W, Mo and Nb [7-10]. Among the various kinds of dopants, W would be a most effective dopant to reduce T_{MI} on a per atomic percent base.

It is expected that a high TCR would remain at around RT because the origin of the stability of metallic states is due to an increase of carriers with minimal structural damage [11], suppressing electron scattering, and a crystal inhomogeneity in comparison with VO_x.

In this session, I investigate the TCR properties of $(V,W)O_2$ thin films with various W-doping levels and report that the maximum TCR was obtained at RT. In addition, we report that high TCR properties are not affected by the film thickness on Al_2O_3 (0001) substrates, which is contrary to usual cases of thin film properties.

7.1.2 Experimental

The $V_{1-x}W_xO_2$ (hereafter denoted as VWO) thin films were deposited on Al_2O_3 (0001) single crystal substrates using a pulsed laser deposition (PLD) technique (ArF excimer: λ=193 nm). The target employed was a sintered VWO pellet prepared by a conventional solid reaction process. V_2O_3 and WO_3 powders were mixed and calcined in air at 410 °C for 11 hours. The samples were then reground and sintered at 410 °C for 20 hours. The fabrication condition of VWO films was at a substrate temperature of 360 °C in an O_2 gas pressure of 1.0 Pa. The film thickness was varied from 43 to 320 nm, measured by nanoscale hybrid AFM (VN-8000, KEYENCE, Japan). The crystallinity was examined by X-ray diffraction measurements (RINT2000, Rigaku, Japan), and the electronic properties were measured using a four-probe method with a Physical Property Measurement System (PPMS, Quantum Design, Japan).

7.1.3 Results and discussion

Figure 7.1.1 shows XRD patterns of VWO films with various doping levels. A peak at 2θ = 41.7° indicates reflection from a (0001) sapphire substrate and a peak at 2θ = 40.0° corresponds to the reflection from the (020) peak of VWO. Only (020) peaks were observed, indicating that the VWO thin films were largely *b*-axis oriented without other directions. There was no discernible change in the XRD spectra among undoped and W-doped (x = 0.01, 0.015, 0.02) VO_2 thin films.

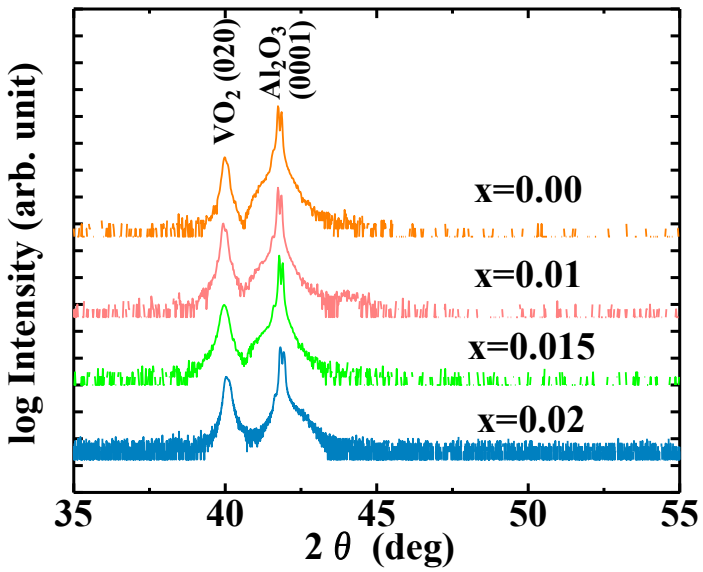

Fig. 7.1.1 XRD spectra of VWO thin films on (0001) sapphire substrates deposited at 360 °C and 1.0 Pa. Doping concentrations are x = 0, 0.01, 0.015, and 0.02,

Figure 7.1.2(a) shows the temperature dependence of resistivity for the VWO thin films. T_{MI} was effectively shifted from 340 K for the VO_2 thin film to 322 K, 309 K, and 300 K for the VWO thin films with x = 0.01, 0.015, and 0.02, respectively. Resistivity in the insulating state in the low temperature region was one-order reduced by the doping at per 1 at%, while resistivity in the metallic state in the high temperature region did not change significantly, suppressing resistive increase due to electron scattering by defects in comparison with oxygen vacant VO_x. We defined T_{max} as an average value of inflection points of the RT curve during the phase transition accompanied by the hysteresis. The reduction rate of T_{max} against W-content x (dT_{max}/dx) was about 23 K/% as shown in Fig. 7.1.2(b), which is consistent with other reports [12, 13].

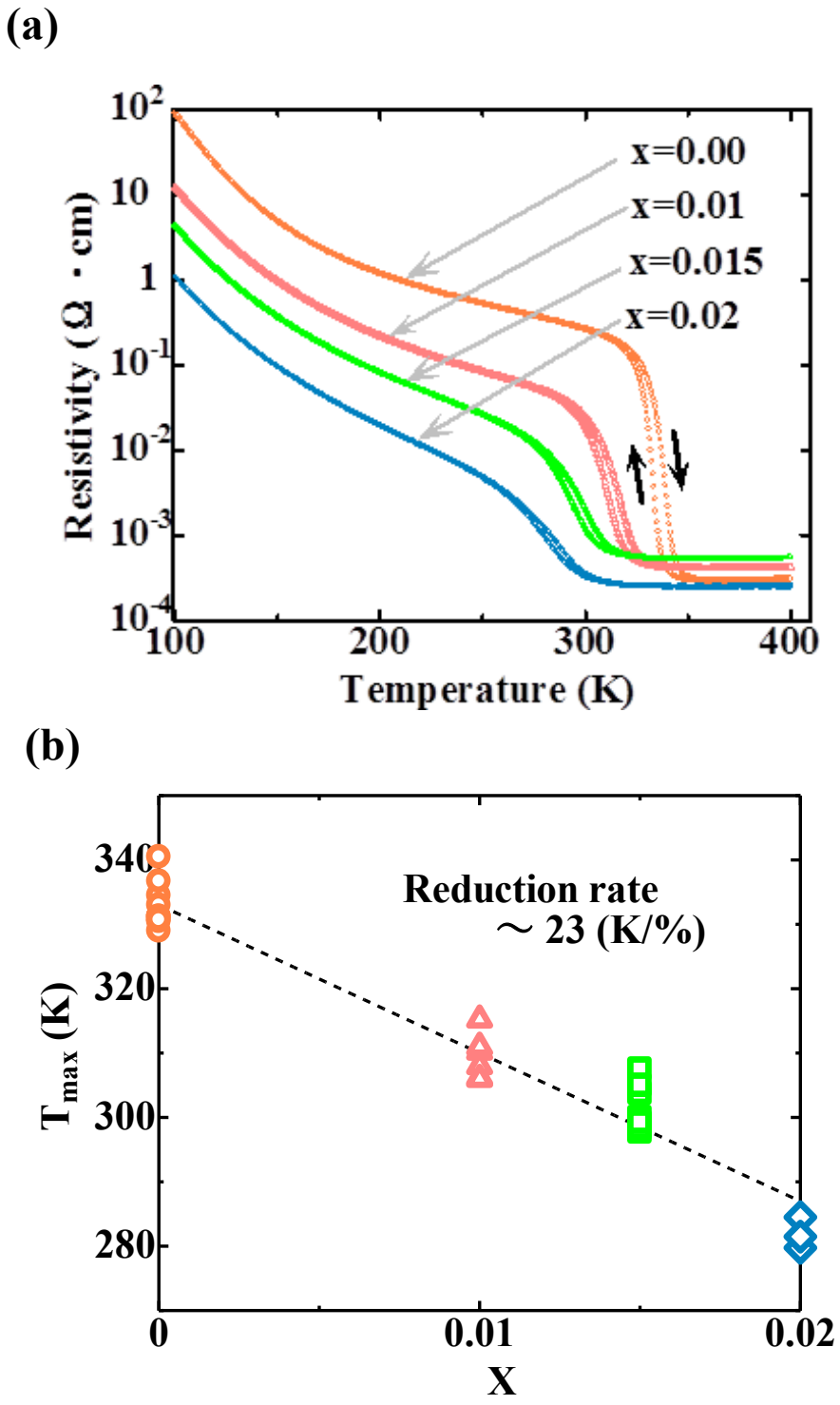

Fig. 7.1.2 (a) Characteristics of MIT for different W-doped VO_2 thin films. (b) T_{max}-reduction rate against W-content *x*.

We can appropriately decrease the T_{max} to room temperature in the sample for x = 0.015. Figure 7.1.3 shows the temperature dependence of |TCR| for VWO films in Fig. 7.1.2(a). The TCR_{max}, defined as the average of two TCR curves with the hysteresis, were -74.8 %/K at T_{max} = 337 K, -24.1 %/K at 315 K, -12.0 %/K at 298 K, and -7.8 %/K at 284 K for the films of x = 0, 0.01, 0.015, and 0.02, respectively.

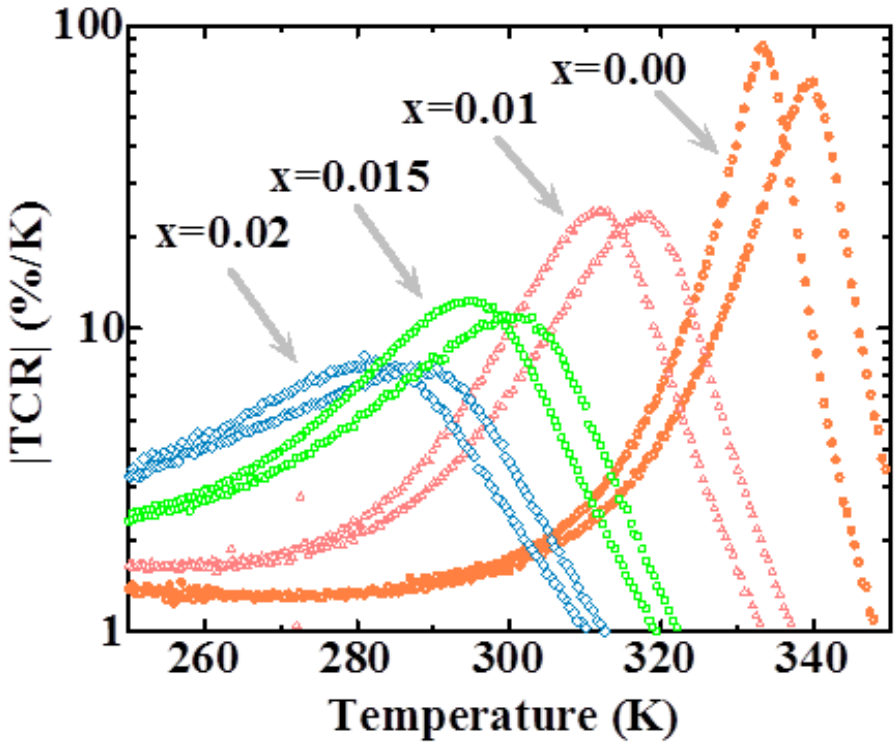

Fig. 7.1.3 Temperature dependence of |TCR| in VWO films with a doping concentration of 0 at% (circle), 1 at% (triangle), 1.5 at% (square) and 2 at%

These TCR values are larger than those in the other materials [6, 8, 14-19], as shown in Fig. 7.1.4(a). Notably, the x = 0.015 film exhibited high $|TCR_{max}|$ values over 10 %/K near room temperature. It is considered that the stability of resistivity in the metallic state as shown in Fig. 7.1.2(a), caused by suppressing ionic defects in crystal structure due to W-dopant, would contribute to the production of the high TCR.

Furthermore, film thickness is an important parameter for bolometers. The performance index for bolometers can be defined as $\boldsymbol{|TCR| \times \sqrt{tchickness} \times \sqrt{n/\gamma}}$, where n is the carrier density and γ is the Hooge parameter [20]. This index is roughly proportional to the signal-to-noise ratio of the bolometer when the sizes of the sensor area are equivalent. It is known that VO_2 on TiO_2 [21, 22] and (La,Ba)MnO_3 on $SrTiO_3$ [18] are bolometric oxide materials working at RT. Their T_{max} are controllable by strain effect using lattice mismatch between the film and the substrate. The strain effect is available only for extremely thin films. Thus it is difficult to obtain high sensor performance in thinner films. On the other hand, in the VWO with x = 0.015 thin films, almost no significant change of the T_{max} and TCR_{max} was found based on their thickness dependence from 70 nm to 270 nm as shown in Fig. 7.1.4(b) and the high TCR survives even in thicker films, which is better for the bolometric performance.

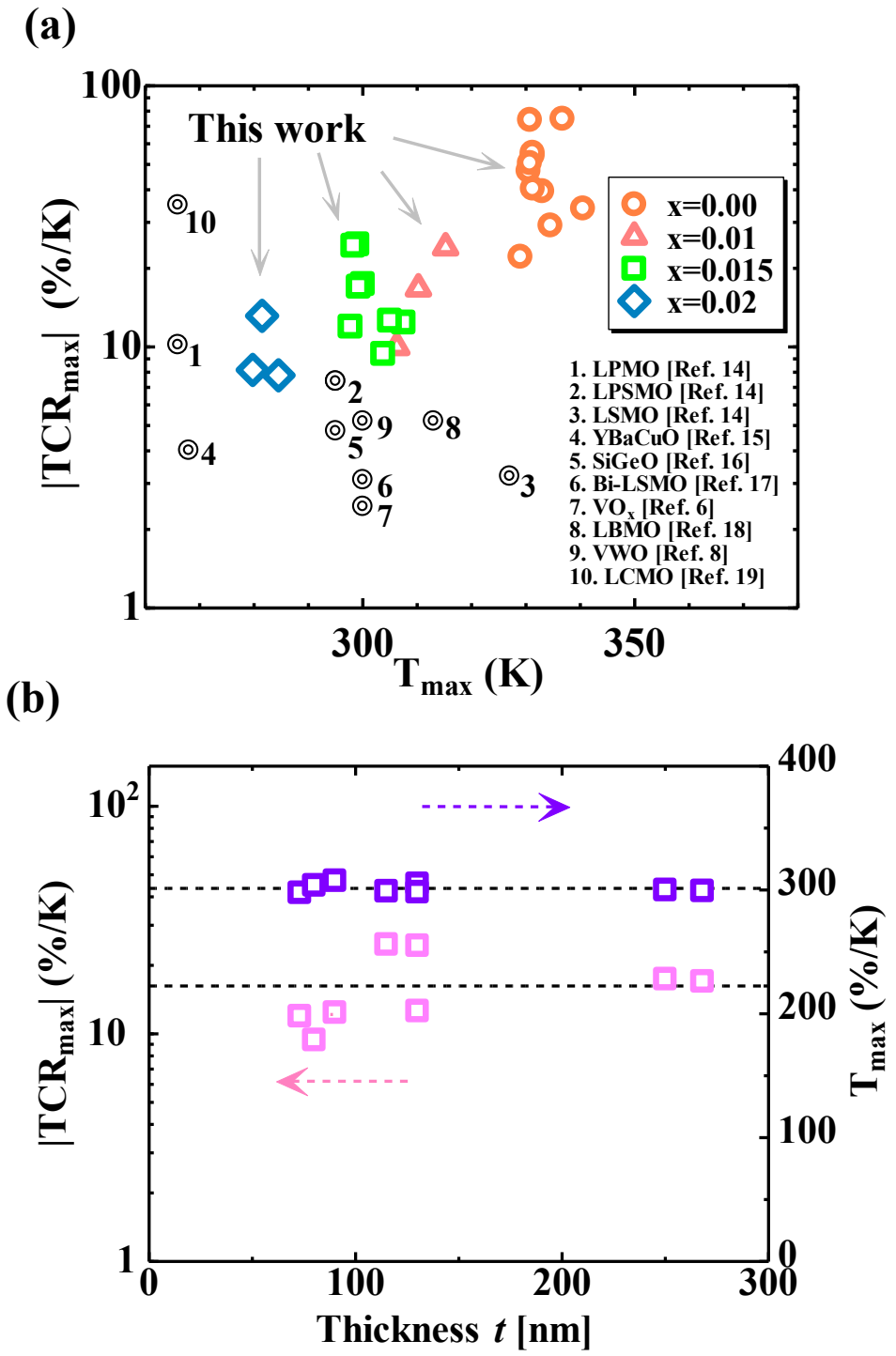

Fig. 7.1.4 (a) $|TCR_{max}|$ as a function of T_{max} for VWO films and other various oxide materials showing high TCR from reference literature (see Refs. [6, 8, 14-19]). Thick circles (x = 0), triangles (x = 0.01), squares (x = 0.015), and diamonds (x = 0.02) represent $|TCR_{max}|$ values determined in this study. The dashed line is provided as a visual aid. (b) Thickness dependence of $|TCR_{max}|$ and T_{max} for x = 0.015 samples.

7.1. 4 Conclusions

I investigated TCR properties of VWO thin films with various W-doping levels and thicknesses. The decrease of T_{MI} was controlled with the high rate of $dT_{MI}/dx \sim 25$ K/% by doping W into VO_2. Especially in the case of VWO for appropriate doping level (x = 0.015) thin films, T_{max} is controlled to RT and showed high TCR over 10 %/K near room temperature. Furthermore, there is no change in TCR in connection with thickness dependence in the wide range from 70 nm to 270 nm, which has full potential for the realization of higher bolometric performance.

7.1.5 References

[1] J. B. Goodenough, *J. Solid State Chem.* **3** (1971) 490

[2] C. H. Chen, X. J. Yi, X. R. Zhao, and B. F. Xiong, *Sens. Actuators* **90** (2001) 212

[3] L. A. L. de Almeida *et al.*: *Appl. Phys. Lett.* **85** (2004) 3605

[4] V. Y. Zerov et al., *J. Opt. Technol*. **66** (1999) 387

[5] Y. H. Han et al., *Thin Solid Films* **425** (2003) 260

[6] N. Fieldhouse, S. M. Pursel, R. Carey, M. W. Horn, and S. S. N. Bharadwaja, *J. Vac. Sci. Technol*. **A 27** (2009) 951

[7] C. Batista, R. Ribeiro, J. Carneiro, and V. Teixeira, *J. Nanosci. Nanotechnol*. **9** (2009) 4220

[8] M. Pan *et al., J. Cryst. Growth* **265** (2004) 121

[9] I. Takahashi, M. Hibino, and T. Kudo, *Jpn. J. Appl. Phys.* **40** (2001) 1391

[10] K. Shibuya, M. Kawasaki, and Y. Tokura, *Appl. Phys. Lett.* **96** (2010) 022102

[11] H. Takami, T. Kanki, S. Ueda, K. Kobayashi, and H. Tanaka, *Appl. Phys. Express* **3** (2010) 063201

[12] M. Tazawa, P. Jin, and S. Tanemura, *Appl. Opt.* **37** (1998) 1858

[13] C. Kim, J. S. Shin, and H. Ozaki, *J. Phys*. *Condens. Matter.* **19** (2007).

[14] A. Lisauskas, S. I. Khartsev, and A. Grishin, *Appl. Phys. Lett.* **77** (2000) 3302

[15] P. C. Shan *et al*., *J. Appl. Phys.* **80** (1996) 7118

[16] M. A. Rana and D. P. Butler: *IEEE Sens. J.* **7** (2007) 1413.

[17] K. Hayashi, E. Ohta, H. Wada, H. Higuma, and S. Miyashita, *Jpn. J. Appl. Phys.*

Part 1 **40** (2001) 5281

[18] H. Touyama, H. Tanaka, T. Kawai, and M. Kanai, *Appl. Phys. Lett.* **87** (2005) 102504

[19] S. I. Khartsev and A. M. Grishin, *Mat. Res. Soc. Symp. Proc.*, (2001), p. F7. 12. 1. 12

[20] F. N. Hooge, *Phys. Lett. A* **29** (1969) 139

[21] K. Nagashima, T. Yanagida, H. Tanaka, and T. Kawai, *J. Appl. Phys.* **101** (2007)

[22] Y. Muraoka and Z. Hiroi, *Appl. Phys. Lett.* **80** (2002) 583

7.2 Electronic structure of W-doped VO_2 thin films with giant metal-insulator transition investigated by hard X-ray core-level photoemission spectroscopy

I use bulk-sensitive hard X-ray core-level photoemission spectroscopy to investigate the electronic structure of W-doped VO_2 (VWO) thin films exhibiting a high temperature coefficient of resistance, above −10 %/K at room temperature. According to the W 4d core-level spectra, the chemical state of doped W takes only a 6+ valence state, which suggests the introduction of V^{3+}. The satellite structure of the V $2p_{3/2}$ main peak, which corresponds to the metallic-coherent screened states, was enhanced for VWO compared with VO_2 indicating that electron doping plays an important role in the control of metal-insulator transition.

7.2.1 Introduction

Vanadium dioxide (VO_2) has electronically attractive properties, showing orders of magnitude changes in resistivity at metal-insulator transition temperature (T_{MI}), around 340 K. This change is caused by a structural deformation between the monoclinic insulating phase at low temperature and the rutile metallic phase at high temperature [1]. A Mott–Hubbard or Peierls transition mechanism has been discussed in relation to these phenomena [2, 3]. From a practical viewpoint, the abrupt change of resistivity in this material is applicable to uncooled bolometers [4-6]. The temperature coefficient of resistance (TCR), defined as $(1/\rho)(d\rho/dT)$, has been applied as a performance index [7]. The TCR value of VO_2 is usually over 70 %/K, however, the maximum value of TCR (TCR_{max}) is obtained only at a fixed and narrow high temperature of around 340 K. This makes it inconvenient for the application in practical devices working at room temperature. Dopant control of mother VO_2 materials is a promising method for obtaining a high TCR, with a wide range, around room temperature. It is known that T_{MI} is reduced by doping transition metal elements such as W, Mo, and Nb [8]. Among these various dopants, W is most effective for reducing T_{MI} [8]. Recently, I realized a TCR above −10 %/K at room temperature in W-doped VO_2 (VWO) thin film. Information on the electronic structures and chemical states of W-doped VO_2 are important for

understanding the origin of its excellent functionality, but only a few controversial results have been reported [9-11]. In this study, I report the electronic structure and chemical states of VWO thin films investigated by hard X-ray core-level photoemission spectroscopy (HX-PES), and compare it with VO_2 film. HX-PES reveals the true bulk electronic structure up to a depth of about 10 nm [12], although conventional PES is surface sensitive, and sometimes yields contradictory results concerning the bulk physical properties.

7.2.2 Experimental

VWO thin films were deposited on Al_2O_3 (0001) single-crystal substrates using a pulsed laser deposition technique (ArF excimer: λ = 193 nm). The targets were a sintered vanadium oxide pellet (V_2O_5), for VO_2, and a tungsten-mixed vanadium oxide pellet for VWO, prepared by a conventional solid-state reaction process. To make the V_2O_5 pellet, high-purity V_2O_3 powder was calcined in air at 410 °C for 11 h. The powder was then reground and sintered at 410°C for 20 h. To make the VWO pellet, high-purity V_2O_3 and WO_3 powders were first thoroughly ground together in the appropriate stoichiometric amounts, and then the same process was applied to the mixed powder. The fabrication of the films was performed at a substrate temperature of 360°C in O_2 at a gas pressure of 1.0 Pa. The film thicknesses were from 110 to 182 nm, as measured by nanoscale hybrid atomic force microscope (VN-8000, KEYENCE, Japan). The film structures were examined using X-ray diffraction measurements (RINT2000, Rigaku, Japan). The electrical properties were measured using a four-probe method with a physical property measurement system (PPMS, Quantum Design, Japan). The HX-PES experiments were performed at BL15XU of SPring-8, and the HX-PES spectra were taken at hv = 5.95 keV. The valence band spectra were measured in the metal phase at 360 K. The total energy resolution was 223 meV, which was evaluated from the Fermi cutoff of an evaporated Au thin film. The binding energy (E_B) was calibrated from the Fermi cutoff of the Au film.

7.2.3 Results and discussion

I systematically modulate T_{MI} by changing a W concentration for VWO thin films as shown in Fig. 7.2.1. Reduction rate of T_{MI} is 19.5 K/at.% which has good agreement with the value previously reported [13].

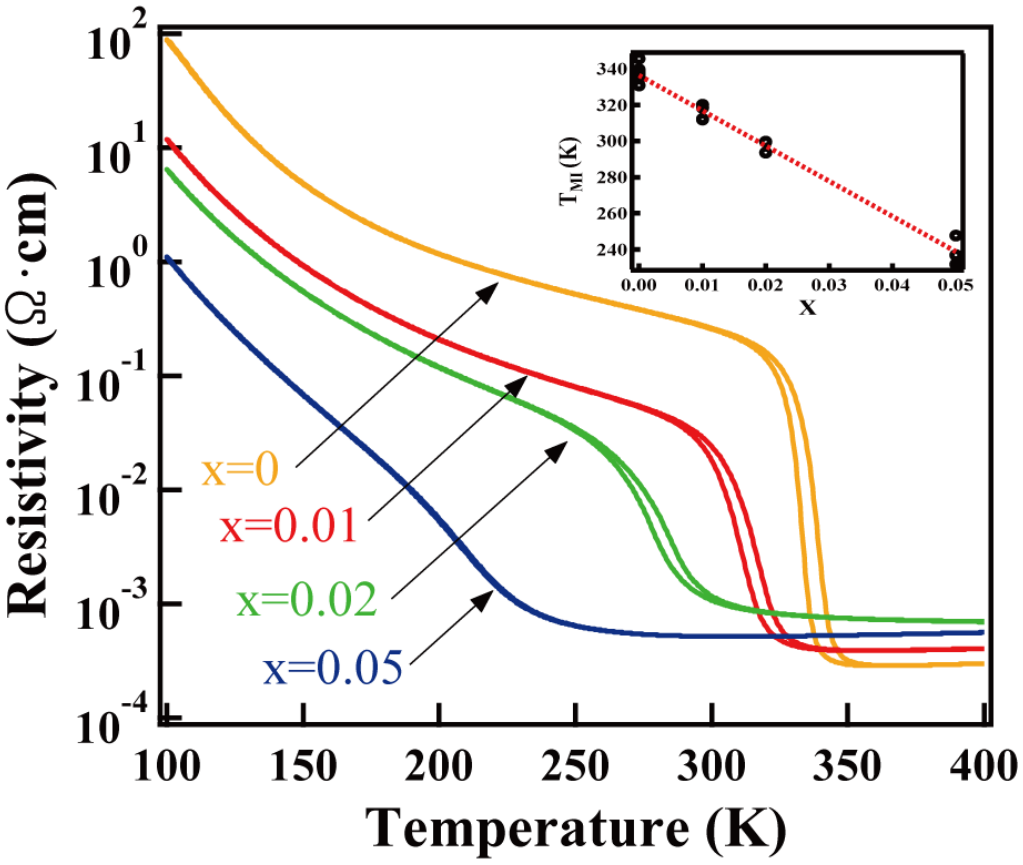

Fig. 7.2.1 Temperature dependence of resistivity for VO_2 and VWO films. Inset shows the x dependence of the metal-insulator transition temperature (T_{MI}).

Figure 7.2.2(a) shows W 4d core level spectrum in VWO film, including a fitting curve of two Lorentzians, L(x) convoluted with a Gaussian, G(x) as a resolution function of the experiment after subtracting the integral type background.

$$I(E_B) = \int_{-\infty}^{\infty} L(E_B - t)G(t)dt \tag{7.2.1}$$

, where, $$L(x) = \frac{1}{\pi}\frac{\Gamma}{(x - x_0)^2 + \Gamma^2} \quad ,$$

$$G(y) = \frac{1}{\Gamma'\sqrt{2\pi}} \exp(\frac{(y - y_0)^2}{2\Gamma'^2}) .$$

The single fitting curve of equation (7.2.1) well agrees with experimental spectrum with x_0 = 246.9 eV, HWHM (Γ) = 2.1 eV for the peak of $2p_{3/2}$, and x_0 = 229.7 eV, HWHM (Γ) = 2.0 eV for the peak of $2p_{1/2}$. The HWHM ($\sqrt{2\ln 2}\Gamma'$) of the Gaussian function is 112 meV. The binding energy at the peak of $4d_{5/2}$ is 246.9 eV, reflecting that the valence of doped W is 6^+. Namely, the chemical state of doped W in VO_2 takes 6^+ valence state [11]. It indicates that V^{4+} ions neighboring doped W^{6+} change to be V^{3+} to keep the charge neutrality as shown in Fig. 7.2.2(b) [10]. Namely,

$$[V^{4+}]_{1-2x}[V^{3+}]_{2x}[W^{6+}]_xO_2 \tag{7.2.2}$$

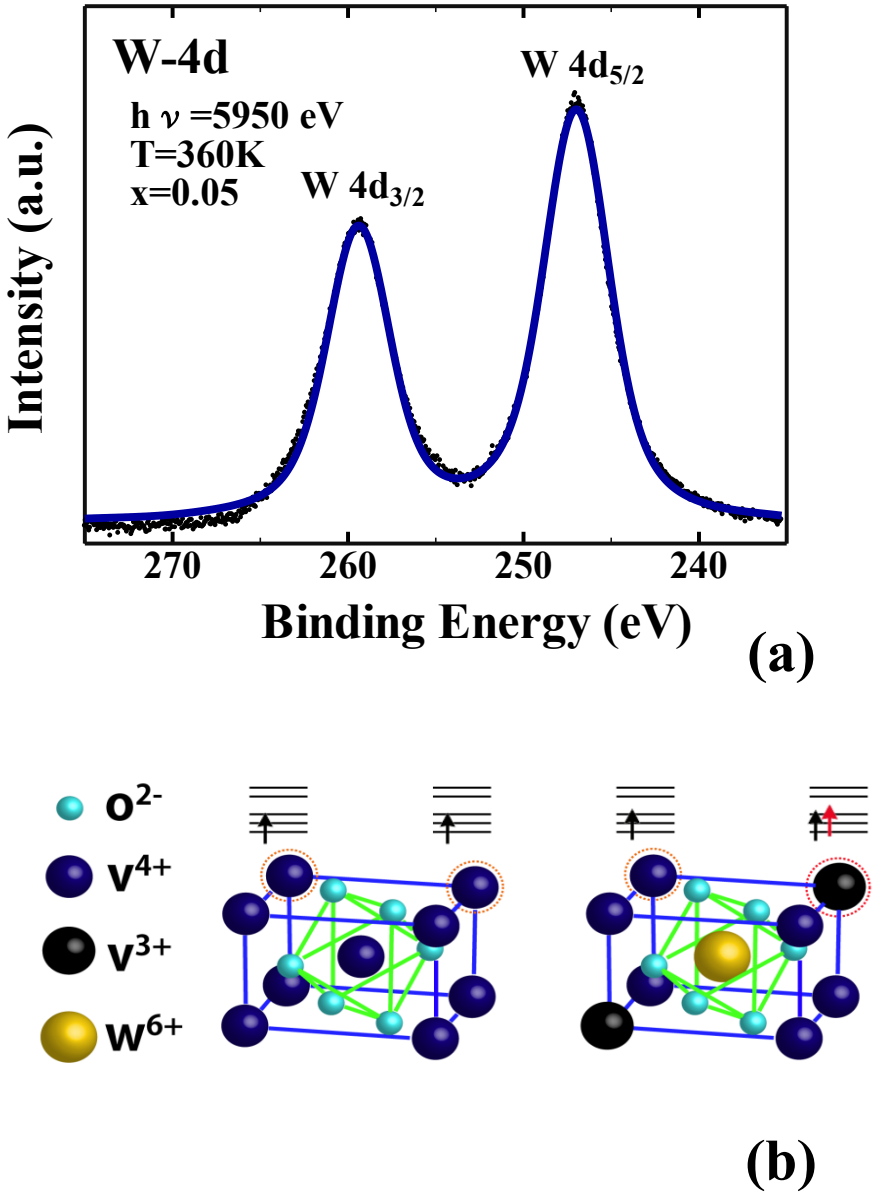

Fig. 7.2.2 (a) W 4d core-level spectrum at 360 K at *hv* = 5.95 keV. (b) The schematic illustration of the W-doping effect on VO_2 system. W-doping results in the electron doping by changing the valence state of some V ions from 4+ to 3+.

To clarify this experimentally, Fig. 7.2.3 shows the V 2p core-level spectra of the VO_2 and VWO films normalized to the integrated intensity after subtracting the integral-type background. A satellite shoulder structure was observed at E_B of 514 eV on the lower binding energy of the V $2p_{3/2}$ main peak for every sample, which was explained by well-screened states due to electrons in the vicinity of E_F, as observed only in the metallic vanadates [14, 15] and manganites [12, 16], and only through the use of HX-PES. This shoulder intensity, I_s, is related to the density of state of the cohered metallic band around E_F, $D(E_F)$ [12], as expressed by $\boldsymbol{I_S \propto D(E_F)}$.

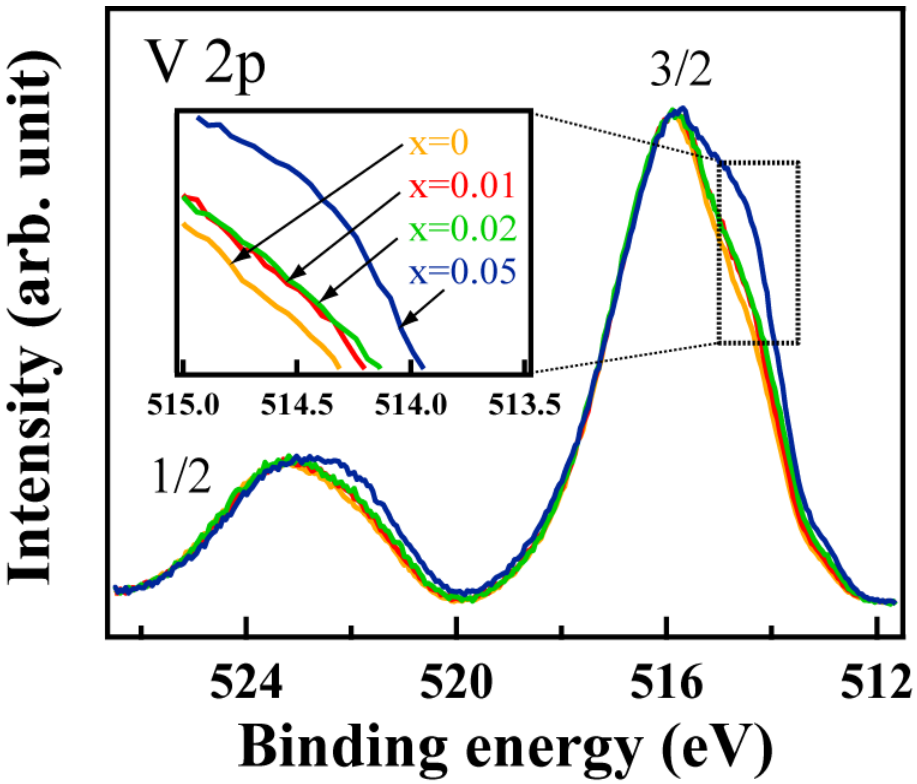

Fig. 7.2.3 V 2p core-level spectrum at 360 K at $h\nu$ = 5.95 keV for various doping concentration. The shoulder structures which are called the well-screened feature are magnified in the inset.

For the VWO film, I_s is enhanced notably compared with the VO_2 film, indicating the enhancement of the carrier density and suggesting the presence of V^{3+} ($3d^2$) ions, though the detection of V^{3+} in core-level spectra is difficult because the chemical shift of V $2p_{3/2}$ between V^{4+} and V^{3+} is only 0.15 eV [17]. This effect breaks the half-filled insulating state (V^{4+}-V^{4+} ($3d^1$ –$3d^1$)) electron configuration.

Figure 7.2.4 shows a schematic illustration of energy levels of VO_2.

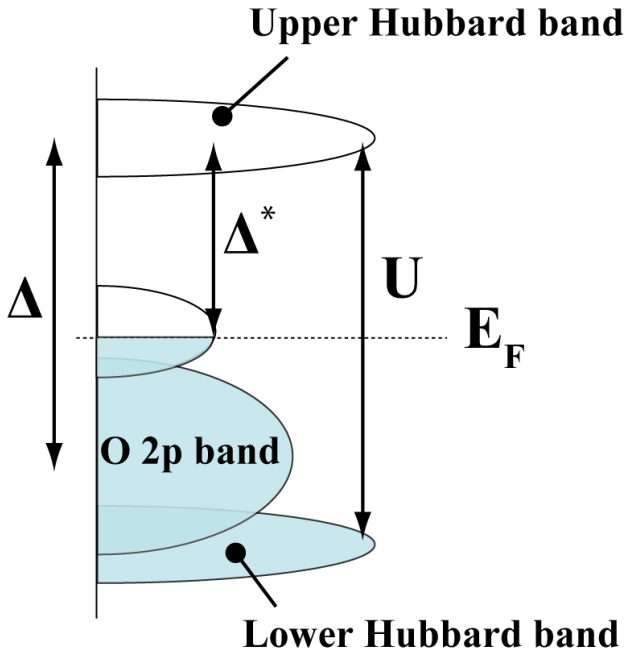

Fig. 7.2.4 Schematic illustration of energy levels for VO_2 in metallic phase.

To analyze the *x* dependence of the well-screened feature, we performed a cluster model calculation, and extract the intensity of the hybridization (V*) between a coherent state at Fermi level and a V 3d as performed by Eguchi *et al.* [3]. The well-screened feature cannot be reproduced without introducing the hybridization parameter *V** in the Hamiltonian [18],

$$\boldsymbol{H = H_1 + H_2}\ , \tag{7.2.3}$$

$$\begin{aligned}\boldsymbol{H_1} = &\sum_{\Gamma,\sigma} \boldsymbol{\varepsilon_{3d}}(\Gamma)\boldsymbol{d^{\dagger}_{\Gamma,\sigma} d_{\Gamma,\sigma}} + \sum_{m,\sigma} \boldsymbol{\varepsilon_{2p}}\, \boldsymbol{p^{\dagger}_{m,\sigma} p_{m,\sigma}} + \sum_{\Gamma,\sigma} \boldsymbol{\varepsilon_{p}}(\Gamma)\boldsymbol{a^{\dagger}_{\Gamma,\sigma} a_{\Gamma,\sigma}} \\ &+ \sum_{\Gamma,\sigma} \boldsymbol{V}(\Gamma)\left(\boldsymbol{d^{\dagger}_{\Gamma,\sigma} a_{\Gamma,\sigma} + d_{\Gamma,\sigma} a^{\dagger}_{\Gamma,\sigma}}\right) + \boldsymbol{U_{dd}} \sum_{(\Gamma,\sigma)\neq(\Gamma',\sigma')} \boldsymbol{d^{\dagger}_{\Gamma,\sigma}\, d_{\Gamma,\sigma} d^{\dagger}_{\Gamma',\sigma'} d_{\Gamma',\sigma'}} \\ &- \boldsymbol{U_{dc}}(\boldsymbol{2p}) \sum_{\Gamma,m,\sigma,\sigma'} \boldsymbol{d^{\dagger}_{\Gamma,\sigma}\, d_{\Gamma,\sigma}}\left(\boldsymbol{1 - p^{\dagger}_{m,\sigma'} p_{m,\sigma'}}\right) + \boldsymbol{H_{multiplet}} \\ \boldsymbol{H_2} = &\textstyle\sum_{\Gamma,\sigma} \boldsymbol{\varepsilon_c}(\Gamma)\boldsymbol{c^{\dagger}_{\Gamma,\sigma} c_{\Gamma,\sigma}} + \sum_{\Gamma,\sigma} \boldsymbol{V^{*}}(\Gamma)\left(\boldsymbol{d^{\dagger}_{\Gamma,\sigma} c_{\Gamma,\sigma} + d_{\Gamma,\sigma} c^{\dagger}_{\Gamma,\sigma}}\right).\end{aligned} \tag{7.2.4}$$

The first term H_1 of the total Hamiltonian, H represents the standard cluster model [19]. In addition to the usual cluster model (H_1 term), C states that are responsible for a screening effect described by the H_2 term in Eq. (7.2.3). These states represent the doping-induced states which develop into a metallic band at E_F. $\boldsymbol{\varepsilon_{3d}}(\Gamma)$, $\boldsymbol{\varepsilon_{2p}}$, $\boldsymbol{\varepsilon_{p}}(\Gamma)$, and $\boldsymbol{\varepsilon_{c}}(\Gamma)$ represent the energies of the V 3d, V 2p, and O 2p ligand states and the doping-induced states at E_F, respectively. The indices m and σ are the orbital and spin states. $V(\Gamma)$, U_{dd}, and $-U_{dc}$(2p) are the hybridizations between the V 3d and O 2p ligand states, on-site repulsive Coulomb interaction between the V 3d states and the attractive 2p core-hole potential, respectively. The spin-orbit interactions for V 2p and 3d states are also included in the $H_{multiplet}$. An effective coupling parameter for describing the interaction strength between the central V 3d orbital and the coherent band, $V^{*}(\Gamma)$ is introduced analogous to the hybridization $V(\Gamma)$.

In my real experiment, a simplified cluster calculation is applied to reproduce the photoemission spectra, and extract the V^{*} which reproduce the relative intensity of the well-screened feature of the photoemission spectra for x = 0-0.05 as shown in the inset of Fig. 7.2.4. Thus, we obtain a x dependence of $(V^{*})^2$, and find that $(V^{*})^2$ almost linearly increases with increasing W-doping concentration.

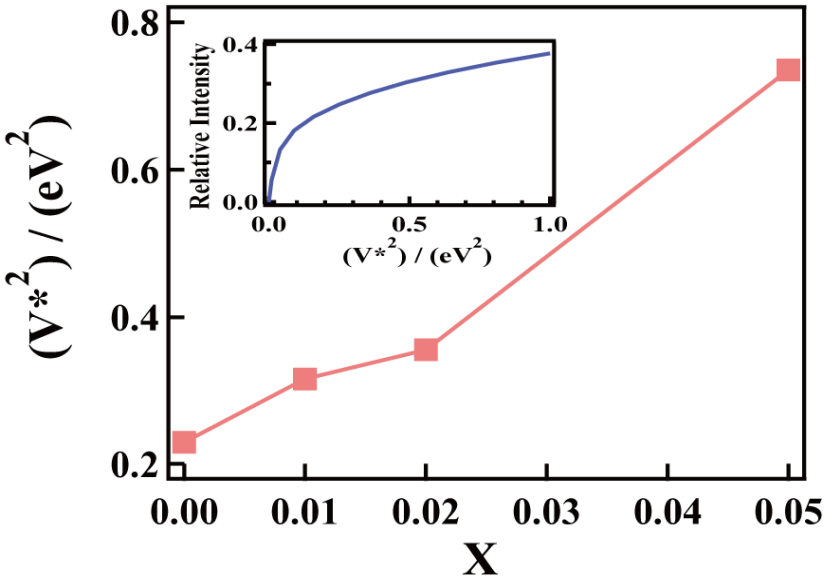

Fig. 7.2.4 The relationship between intensities of square of hybridization V^* and W-doping concentration x. The inset shows a relationship between relative intensity of the spectra and the parameter $(V^*)^2$ used in the simplified cluster calculation.

On the other hand, the chemical pressure effect, caused by the difference in the ionic radii between W^{6+} and V^{4+}, can affect T_{MI}, if the hydrostatic pressure effect on VO_2 is considered [20]. In this case, the hydrostatic pressure could be converted to a change of lattice parameters using the following equations [21]:

$$\Delta P_a = -\frac{\Delta a(x)}{a(x)} \cdot \frac{1}{\chi_{1R}} \quad , \tag{7.2.5}$$

$$\Delta P_c = -\frac{\Delta c(x)}{c(x)} \cdot \frac{1}{\chi_{2R}} \quad , \tag{7.2.6}$$

where ΔP represents the hydrostatic pressure, and $\boldsymbol{\chi_{1R}}$ and $\boldsymbol{\chi_{2R}}$ are the compressibility coefficients along the a- and c-axis, respectively. In the case of W doping experiments, the lattice parameters $a(x)$ and $c(x)$ depend on the doping concentration of W, giving the following equations for the tetragonal form [21];

$$a(x) = \sqrt{2} d_{V-O}[1 + \sin\left(\frac{\phi}{2}\right)] \tag{7.2.7}$$

$$c(x) = \sqrt{2} d_{V-O} \cos\left(\frac{\phi}{2}\right) \quad , \tag{7.2.8}$$

where x is the doping ratio, $d_{V\text{-}O}$ is the metal-oxygen distance, and ϕ is the O-V-O

angle (= 90°) in the (110) plane. The $d_{V\text{-}O}$ within $x < 0.33$ can be accurately evaluated by:

$$d_{V-O} = (1-3x)\cdot d_{V^4} + 2x\cdot d_{V^3} + x\cdot d_{W^6} \quad , \tag{7.2.9}$$

where d_{V^4} , d_{V^3} , and d_{W^6} are the distances from O to V^{4+}, V^{3+}, and W^{6+}, respectively. According to the table of effective ionic radii by Shannon [22], the ion radii are 0.58 and 0.60 Å for V^{4+} and W^{6+}, respectively. By applying Eqs. (7.2.5) - (7.2.9), and using the parameters shown in the reference [21], to our sample (x = 0.01), we could estimate the ΔP of 0.3 GPa in tension. This ΔP corresponds to a T_{MI} change of only 0.24 K by chemical pressure, based on following experimental relationship [20]:

$$\Delta T_{MI} = 0.8 \times \Delta P \quad \text{(K)} \tag{7.2.10}$$

This ΔT_{MI} by chemical pressure is negligibly small compared with our experimental one ($\Delta T_{MI} \sim 20$K) shown in Fig. 7.2.1.

As a result, the increase in carrier from W-doping into VO_2 is a dominant effect for changing T_{MI}, rather than chemical pressure caused by different radii between W and V ions.

7.2.4 Conclusions

In summary, I used HX-PES to examine the electronic structure and chemical state of VWO thin film exhibiting a high TCR, over −10 %/K at room temperature. We found that the valence of doped W becomes 6+, suggesting the existence of V^{3+}. I also experimentally detected enhancement of the metallic well-screened feature in the V $2p_{3/2}$ core-level spectrum for VWO and found that the intensities of hybridization between coherent state at Fermi level and V 3d are enhanced by W-doing concentration, indicating that electron doping is an effective mechanism for controlling the metal-insulator transition in the $(V_{1-x}W_x)O_2$ system.

7.2.5 References

[1] Goodenough.Jb, *J. Solid State Chem.* **3** (1971) 490

[2] R. M. Wentzcovitch, W. W. Schulz, and P. B. Allen, *Phys. Rev. Lett.* **72** (1994) 3389

[3] R. Eguchi *et al., Phys. Rev. B* **78** (2008) 075115

[4] C. H. Chen, X. J. Yi, X. R. Zhao, and B. F. Xiong, *Sens. Actuators* **90** (2001) 212

[5] L. A. L. de Almeida, *Appl. Phys. Lett.* **85** (2004) 3605

[6] V. Y. Zerov, *J. Opt. Technol.* **66** (1999) 387

[7] Y. H. Han *et al. Thin Solid Films* **425** (2003) 260

[8] I. Takahashi, M. Hibino, and T. Kudo, *Jpn. J. Appl. Phys.* **40** (2001) 1391

[9] T. D. Manning, I. P. Parkin, M. E. Pemble, D. Sheel, and D. Vernardou, *Chem. Mater.* **16** (2004) 744

[10] C. Tang, *Phys. Rev. B* **31** (1985) 1000

[11] A. Romanyuk, R. Steiner, L. Marot, and P. Oelhafen, *Sol. Energy Mater. Sol. Cells* **91** (2007) 1831

[12] H. Tanaka *et al.*, *Phys. Rev. B* **73** (2006) 094403

[13] M. Tazawa, P. Jin, and S. Tanemura, *Appl. Opt.* **37** (1998) 1858

[14] S. Suga *et al*., *New J. Phys.* **11** (2009) 103015

[15] T. Miyamachi., *J. Magn. Magn. Mater.* **310** (2007) E252

[16] K. Horiba., *et al. Phys. Rev. Lett.* **93** (2004) 236401

[17] M. Demeter, M. Neumann, and W. Reichelt, *Surf. Sci.* **454** (2000) 41

[18] M. Taguchi et al., *Phys. Rev. B* **76** (2007)

[19] M. Taguchi, T. Uozumi, and A. Kotani, *J. Phys. Soc. Jpn.* **66** (1997) 247

[20] C. N. Berglund and A. Jayarama, *Phys. Rev.* **185** (1969) 1034

[21] J. C. Rakotoniaina *et al., J. Solid State Chem.* **103** (1993) 81

[22] R. D. Shannon, *Acta Crystallogr.* A **32** (1976) 751

7.3 Filling-controlled Mott transition in W-doped VO_2

I use bulk-sensitive hard X-ray photoemission spectroscopy to investigate the modulation mechanism of the metal-insulator transition temperature (T_{MI}) for W-doped VO_2 thin films. Judging from the valence band spectra, the electron carrier is doped and spectral weight of the incoherent part is transferred to the coherent part by doping W. It indicates that the electron doping decreases the effective electron-electron correlation energy and stabilizes the metal phase of VO_2, so we drastically modulated the T_{MI} to room temperature. It is the direct evidence of filling-control of VO_2 and shows that the W-doped VO_2 is the third material which shows the giant physical properties near room temperature following the cuprates of high-*T*c superconductivity and manganites of giant magneto resistance at room temperature.

7.3.1 Introduction

3d transition metal oxides with strongly correlated electron system show giant physical properties, such as high-Tc superconductivity in cuprates [1-6] or giant magneto resistance in manganites [7-11]. These properties are originated from electronic dynamics near metal-insulator transition with strongly correlated electrons, and can be modulated by controlling a band filling by carrier doping which is so called the filling-control [7]. Vanadium dioxide (VO_2) shows a giant metal-insulator transition at 340 K, and the metal-insulator transition temperature (T_{MI}) can be modulated by doping transition metal oxides [12-15]. Especially, W doping into VO_2 is the most effective way to modulate the T_{MI}, and the key effect of the T_{MI} modulation is the electron doping [14, 16-19]. And VO_2 has the potential to realize the filling-control by electron doping because VO_2 is also said to be the strongly correlated electron system [20-23]. However, few studies were carried out to approach an origin of the drastic change of the T_{MI} (21 - 28 K/at. %) because of the lack of information of the intrinsic bulk electronic structure of W-doped VO_2. So we performed bulk-sensitive hard-X-ray photoemission spectroscopy (HX-PES) to investigate the electronic structures of W-doped VO_2 thin films with systematically controlled doping concentration, and found

the direct evidence of the filling control by doped electron, which leads to the change of the effective electron-electron correlation energy (U_{eff}). So I found the VO_2 is the third oxide material with strongly correlated electron system which shows the giant physical property changes by filling-control as well as cuprates and manganites.

7.3.2 Experimental

VWO thin films were deposited on Al_2O_3 (0001) single-crystal substrates using a pulsed laser deposition technique (ArF excimer: λ = 193 nm). The targets were a sintered vanadium oxide pellet (V_2O_5), for VO_2, and a tungsten-mixed vanadium oxide pellet for VWO, prepared by a conventional solid-state reaction process. To make the V_2O_5 pellet, high-purity V_2O_3 powder was calcined in air at 410°C for 11 h. The powder was then reground and sintered at 410°C for 20 h. To make the VWO pellet, high-purity V_2O_3 and WO_3 powders were first thoroughly ground together in the appropriate stoichiometric amounts, and then the same process was applied to the mixed powder. The fabrication of the films was performed at a substrate temperature of 360°C in O_2 at a gas pressure of 1.0 Pa. The film thicknesses were from 110 to 182 nm, as measured by nanoscale hybrid atomic force microscope (VN-8000, Keyence, Japan). The film structures were examined using X-ray diffraction measurements (RINT2000, Rigaku, Japan). The electrical properties were measured using a four-probe method with a physical property measurement system (PPMS, Quantum Design, Japan). The HX-PES experiments were performed at BL15XU of SPring-8, and the HX-PES spectra were taken at $h\nu$ = 5.95 keV in the metal phase at 360 K. The total energy resolution was 223 meV, which was evaluated from the Fermi cutoff of an evaporated Au thin film. The binding energy (E_B) was calibrated from the Fermi cutoff of the Au film.

7.3.3 Results and discussion

I systematically modulate T_{MI} by changing a W concentration for VWO thin films as shown in Fig. 7.3.1. Reduction rate of T_{MI} is 19.5 K/at.% which has good agreement with the value previously reported [24].

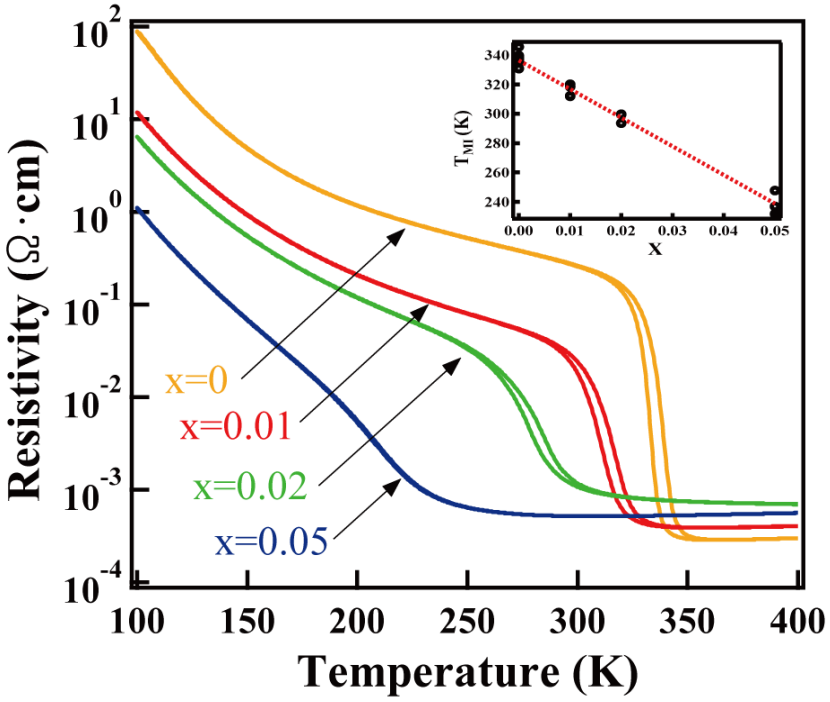

Figure 7.3.1 Temperature dependence of resistivity for VO_2 and VWO films. Inset shows the x dependence of the metal-insulator transition temperature (T_{MI}).

Figure 7.3.2(a) shows valence band spectra normalized by the integrated intensity of V 2p spectra and chemical composition of V after subtracting integral-type background. Figure 7.3.2(b) shows the x dependence of the photoelectron intensity at Fermi level ($I(E_F)$) which is related to DOS(E_F). So it is found that the electron carriers were doped by doping W, and are systematically increased by increasing a doping concentration.

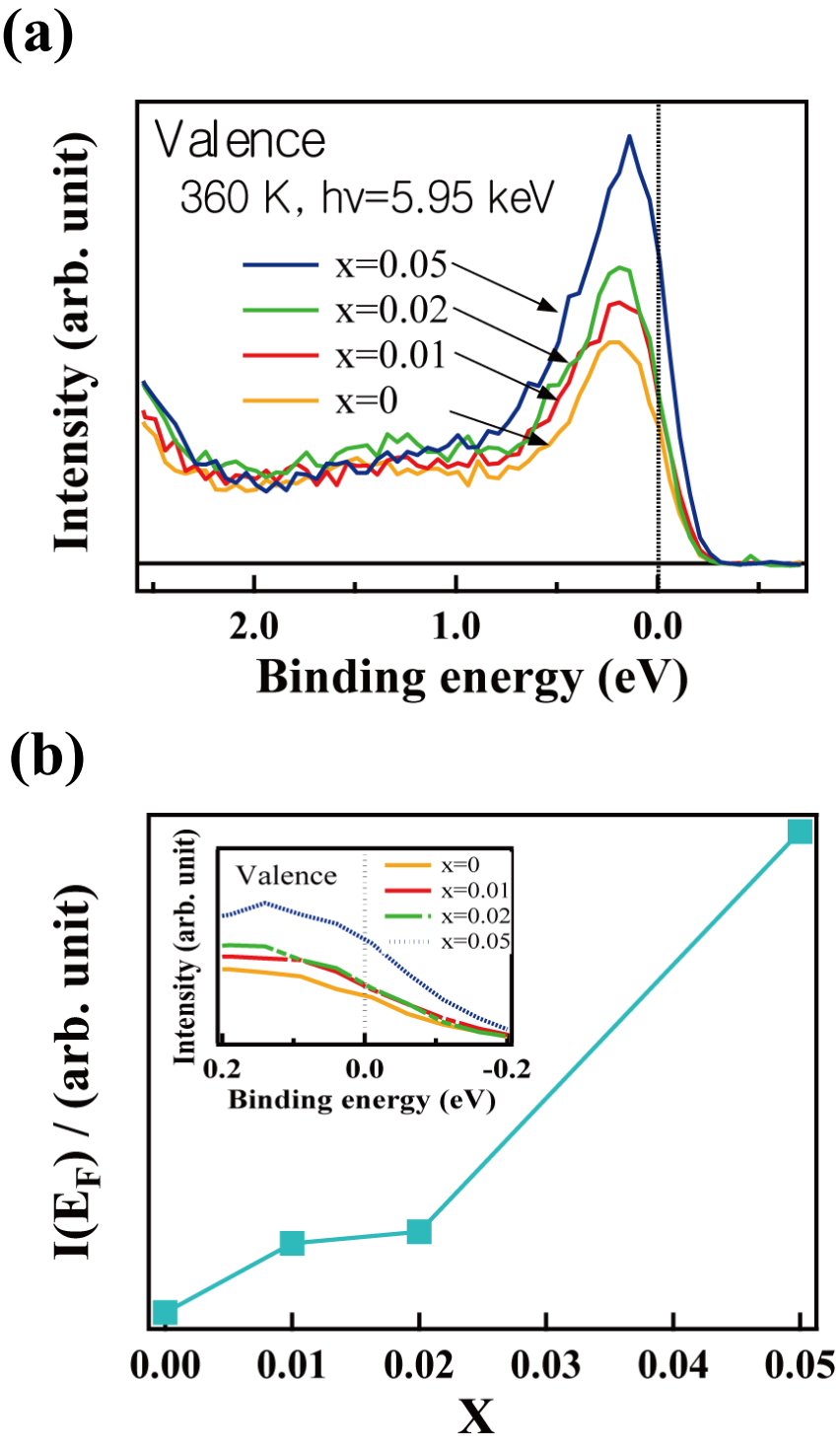

Figure **7.3.2** (a) Valence band spectra of VWO with various doping concentration taken at 360 K at $h\nu$ = 5.95 keV. (b) The relationship between the doping concentration x and the photoelectron intensity at Fermi level ($I(E_F)$).

As already discussed, VO_2 has the potential to realize the filling-control by electron doping because the electron-electron correlation is effective even in the metal region [20]. To investigate the effects of the electron carrier to electron-electron correlation and band filing of VO_2, I analyzed the evolution of the spectral weight of the coherent part and the incoherent part as shown in Fig. 7.3.3. The d-derived photoemission spectra have been decomposed into the coherent (quasiparticle) and incoherent (Hubbard band) parts for the d^1 system [25-27]. The relative spectral weight of the coherent part to the incoherent part is given by z : 1-z, where $\boldsymbol{z \equiv 1/(1-[\partial Re\Sigma(k,\omega)/\partial\omega])_{\omega=E_F,k=k_F}}$ is called the renormalization factor. Here, $\boldsymbol{\Sigma(k,\omega)}$ is the momentum- and energy-dependent self-energy correction to the uncorrelated band structure.

In the case of electron-electron interaction, Green's function of the system is described using the self energy,

$$\boldsymbol{G(k,E) = \frac{1}{E-E^0(k)-\Sigma(k.E)}} \ , \tag{7.3.1}$$

where $\boldsymbol{E^0(k)}$ is the single-particle electron energy with no electron interaction. Equation (7.3.1) is called the Dyson's equation [28].

With (7.3.1), this yields the single particle spectral function,

$$\boldsymbol{A(k,E) = \frac{1}{\pi}\frac{Im\Sigma}{(E-E^0(k)-\mathrm{Re}(k,E))^2+(Im\Sigma)^2}} \ , \tag{7.3.2}$$

If the self-energy is small, it is convenient to decompose the Green's function $G(k,E)$ into a pole part (which yields $G^0(k,E)$ for vanishing Σ) and a term that contains the "rest" ($G_{incoherent}$ of G_{inc}) [29]

$$G(k,E) = \frac{Z_k}{E-(\mathrm{ReE^1}(k)+i(Im\mathrm{E^1}(k))} + (1-Z_k)G_{inc} \ , \tag{7.3.3}$$

or

$$A(k,E) = \frac{1}{\pi}\frac{Z_k\, Im\{\mathrm{E^1}(k)\}}{[E-\{\mathrm{ReE^1}(k)\}]^2+[Im\{\mathrm{E^1}(k)\}]^2} + (1-Z_k)A_{inc} \ , \tag{7.3.4}$$

where Z_k is a normalization constant, E^1 is the electron energy with electron interaction.

Equation (7.3.4) can be used to justify the quasi-particle picture of the electrons in an interacting electron system. The pole part of G yields a spectrum of the electron excitations with a renormalized energy (mass) and a finite width, in just the same way as G^0 yields a spectrum with the single-electron energy $\boldsymbol{E^0(k)}$ (free electron mass) and

infinite lifetime. The electrons in the interacting system are “dressed” by virtual excitations that move with them coherently. These “particles”, made up of the electrons with their cloud of excitations, are called the quasi-particle. The pole part of the Green’s function is often called its coherent part. The remaining part cannot be defined rigorously (this applies to the experimental level; mathematically one can distinguish the coherent and the incoherent part rigorously) because the coherent part already contains low-energy excitations (e.g., electron-hole pairs). This distinguishes Eq. 7.3.4 from the case in which only discrete excitations were possible. In that former case a separation into the main line (~coherent part of the spectrum) and satellite lines (~incoherent part of the spectrum) can (in principle) be performed rigorously.

The coherent state is a main peak observed at E_B =0.25 eV [30-32]. The incoherent state corresponds to the rather flat region expanding in the range of E_B = 0.9- 2.2 eV and it is also said to be the lower Hubbard band [30-32]. Judging from the non-bonding character of the shallow E_B part of ‘O2p’ band, we subtract the O 2p component from the valence band spectra as done by the Ref. [30]. And then, I fit the experimental spectra with various doping concentration (dotted line) by using two Voigt functions multiplied by the Fermi-Dirac distribution obtained at 360 K considering the asymmetric parameter and experimental resolution. The long dashed short dashed red line corresponds to the coherent part, and the long dashed double-short dashed blue line corresponds to the incoherent one. Figure 7.3.3(a) shows the x dependence of integrated intensities of the coherent part (red line) and incoherent one (blue line). It is found that the coherent part increases and the incoherent part decreases by increasing doping concentration. In the Mott-Hubbard systems with d^1 configuration, such as ReO_3, VO_2, $LaTiO_3$, spectral weight is transferred from the incoherent part to the coherent part with decreasing the effective electron-electron correlation energy U_{eff} against band width W [25, 33]. Figure 7.3.4 shows the scenario of the filling-control of VO_2 by doping W. When the electron carriers are doped into VO_2, they break the half-filled d^1-d^1 configuration of VO_2 and U_{eff} decreased, which results in the stabilization of metal phase and T_{MI} is controlled to room temperature.

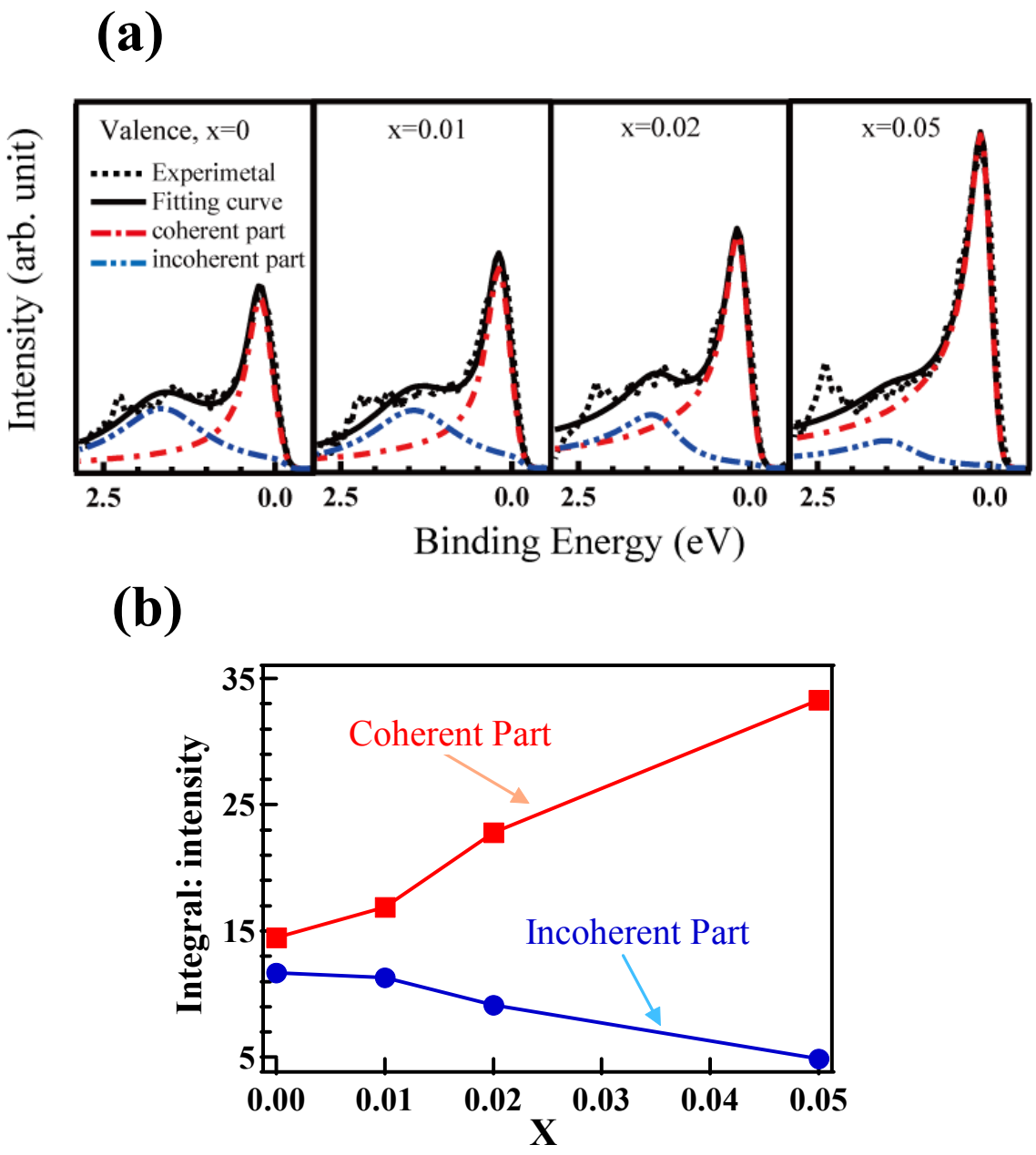

Fig. 7.3.3 (a) Decomposition of the valence band spectra into the coherent part (long dashed short dashed red line) and the incoherent part (long dashed double-short dashed blue line). (b) The relationship between the doping concentration *x* and the integrated photoelectron intensity of the coherent part (red) and the incoherent one (blue).

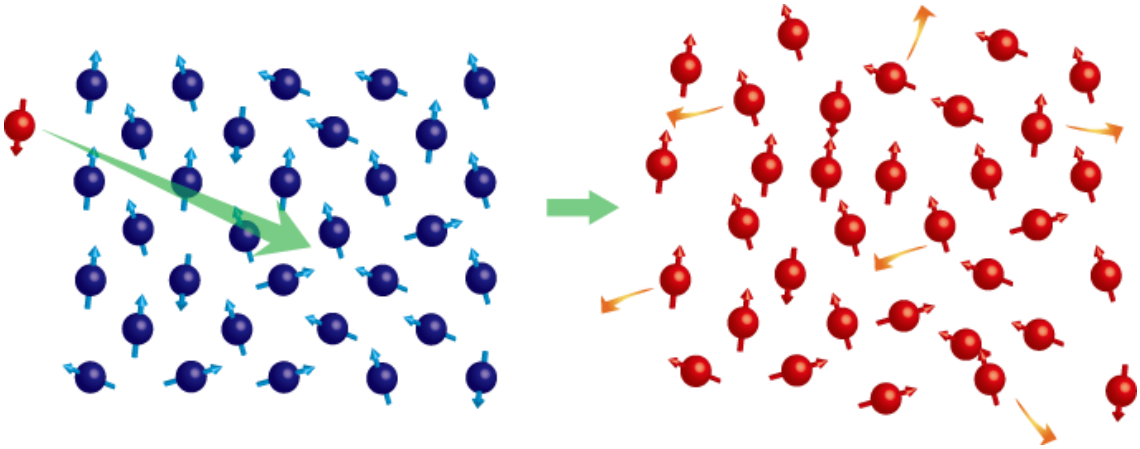

Fig. 7.3.4 A scenario of the filling-control of VO_2 by doping W. The electron introduced by the doped W breaks a half-filling d^1-d^1 configuration of VO_2, which drastically change the electronic states.

7.3.4 Conclusions

In summary, I use bulk-sensitive hard X-ray photoemission spectroscopy to investigate the modulation mechanism of T_{MI} for W-doped VO_2 thin films. Judging from the valence band spectra, the electron carrier is doped and spectral weight of the incoherent part is transferred to the coherent part by doping W. It indicates that the electron doping decreases the U_{eff} and stabilizes the metal phase of VO_2, so the T_{MI} can be drastically controlled to room temperature. It is the direct evidence of filling-control of VO_2 and shows that the W-doped VO_2 is the third material which shows the giant physical properties near room temperature following the cuprates of high-Tc superconductivity and manganites of giant magneto resistance at room temperature.

7.3.5 References

[1] J. G. Bednorz and K. A. Muller, *Z. Phys. B* **64** (1986) 189

[2] C. V. Parker et al., *Nature* **468** (2010) 677

[3] P. Abbamonte et al., *Nat. Phys.* **1** (2005) 155

[4] J. B. Torrance et al., *Phys. Rev. Lett.* **61** (1988) 1127

[5] R. Micnas, J. Ranninger, and S. Robaszkiewicz, *Rev. Mod. Phys.* **62** (1990) 113

[6] J. Hoppler et al., *Nat. Mater.* **8** (2009) 315

[7] Y. Tokura., *J. Phys. Soc. Jpn.* **63** (1994) 3931

[8] A. Urushibara et al., *Phys. Rev. B* **51** (1995) 14103.

[9] P. Schiffer, A. P. Ramirez, W. Bao, and S. W. Cheong, *Phys. Rev. Lett*. **75** (1995) 3336

[10] Y. Moritomo, A. Asamitsu, H. Kuwahara, and Y. Tokura, *Nature* **380** (1996) 11 141

[11] M. B. Salamon and M. Jaime, *Rev. Mod. Phys.* **73** (2001) 583

[12] M. Soltani, M. Chaker, E. Haddad, R. V. Kruzelecky, and J. Margot, *Appl. Phys. Lett.* **85** (2004) 1958

[13] I. Takahashi, M. Hibino, and T. Kudo, *Jpn. J. Appl. Phys. Part 1* **40** (2001) 1391

[14] K. Shibuya, M. Kawasaki, and Y. Tokura, *Appl. Phys. Lett.* **96** (2010) 022102

[15] K. L. Holman et al., *Phys. Rev. B* **79** (2009) 245114

[16] K. Shibuya, M. Kawasaki, and Y. Tokura, *Phys. Rev. B* **82** (2010) 205118

[17] P. Jin and S. Tanemura, *Jpn. J. Appl. Phys. Part 1* **34** (1995) 2459

[18] A. Romanyuk, R. Steiner, L. Marot, and P. Oelhafen, *Sol. Energy Mater. Sol. Cells* **91** (2007) 1831

[19] H. Takami, T. Kanki, S. Ueda, K. Kobayashi, and H. Tanaka, *Appl. Phys. Express* **3** (2010) 063201

[20] M. M. Qazilbash *et al., Phys. Rev. B* **74** (2006) 12

[21] K. Okazaki *et al., Phys. Rev. B* **69** (2004) 165104

[22] S. Biermann, A. Poteryaev, A. I. Lichtenstein, and A. Georges, *Phys. Rev. Lett.* **94** (2005) 026404

[23] H. T. Kim *et al*., *New J. Phys.* **6** (2004) 52

[24] M. Tazawa, P. Jin, and S. Tanemura, *Appl. Opt.* **37** (1998) 1858

[25] A. Fujimori *et al.*, *Phys. Rev. Lett.* **69** (1992) 1796

[26] I. H. Inoue *et al., Phys. Rev. Lett*. **74** (1995) 2539

[27] K. Morikawa *et al., Phys. Rev. B* **52** (1995) 13711

[28] L. Hedin and S. Lundqvist, *Solid State Physics* (Academic Press, New york, 1969)

[29] S. Hufner, *Photoelectron Spectroscopy* (Springer, 2003)
[30] S. Suga, *et al., New J. Phys.* **11** (2009) 103015
[31] R. Eguchi *et al., Phys. Rev. B* **78** (2008) 075115
[32] T. C. Koethe *et al., Phys. Rev. Lett.* **97** (2006) 116402
[33] M. Imada, A. Fujimori, and Y. Tokura, *Rev. Mod. Phys.* **70** (1998) 1039

7.4 Mold treatment

To successfully transfer nanopaterns of a mold into organic resists, the anti-sticking treatment of the mold is important. Without the treatment, organic resists stick to the mold after the pressing process in the NIL, resulting in the destruction of the organic resist pattern. Ideally, the optimal anti-sticking treatment should be selected for every kinds of organic resists by considering the chemical interaction between anti-sticking agent covering over the mold surface and organic resists. Figure 7.4.1 shows the optical microscope image of the mold surface stuffed with the organic resist. Bright-colored material indicated by the yellow circle is organic resists. The used chemical solution for anti-sticking treatment is Optool HD1100TH (DAIKIN, Japan). And the used UV-cured organic resist is TPIR-217 T-3 NL (Tokyo Ohka Kogyo, Japan). Figure 7.4.2 shows the detailed process for mold treatment.

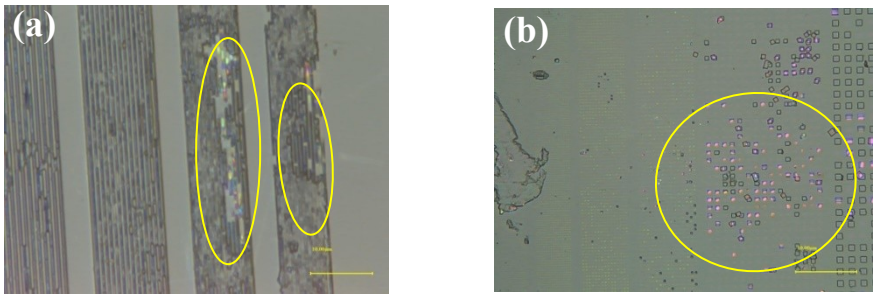

Fig. 7.4.1 Optical microscope image of the mold surface after the nanoimprinting for (a) line –patterned region and (b) box-patterned region. The organic resists stick to the mold surface

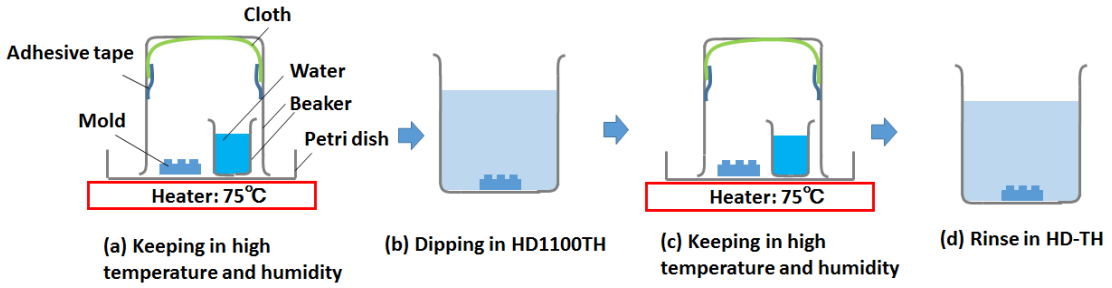

Fig. 7.4.2 The detailed process for anti-stick treatment of the mold used in Fig. 7.4.1. (a) Keeping the mold on the heater at 75 °C with a beaker filled with water covered by a big beaker for 2 hours. The cloth (BEMCOT, AsahiKASEI, Japn) was sticked on the top of the beaker by adhesive tape not for the condensed water drop to fall down to the mold. (b) Dipping in HD1100TH solution for 1 min. (c) Keeping in the same condition as (a) for 1 hour. (d) Rinse in HD-TH solution.

The anti-sticking process as shown in Fig. 7.4.2. is basic one proposed by the product company, DAIKIN. However, the process is not effective with the UV-cured resist used in my experiment as shown in Fig. 7.4.1. To obtain the well-defined nanostructure without destruction of organic resist pattern with smooth release process in the NIL, I optimized the anti-sticking process by using another anti-sticking agent, FAS-13 ((Tridecafuluoro-1,1,2,2,-tetrahydrooctyl) Trichlorosilane, Gelest, USA) as shown in Fig. 7.4.3. Figure 7.4.4 shows the chemical structure of FAS-13.

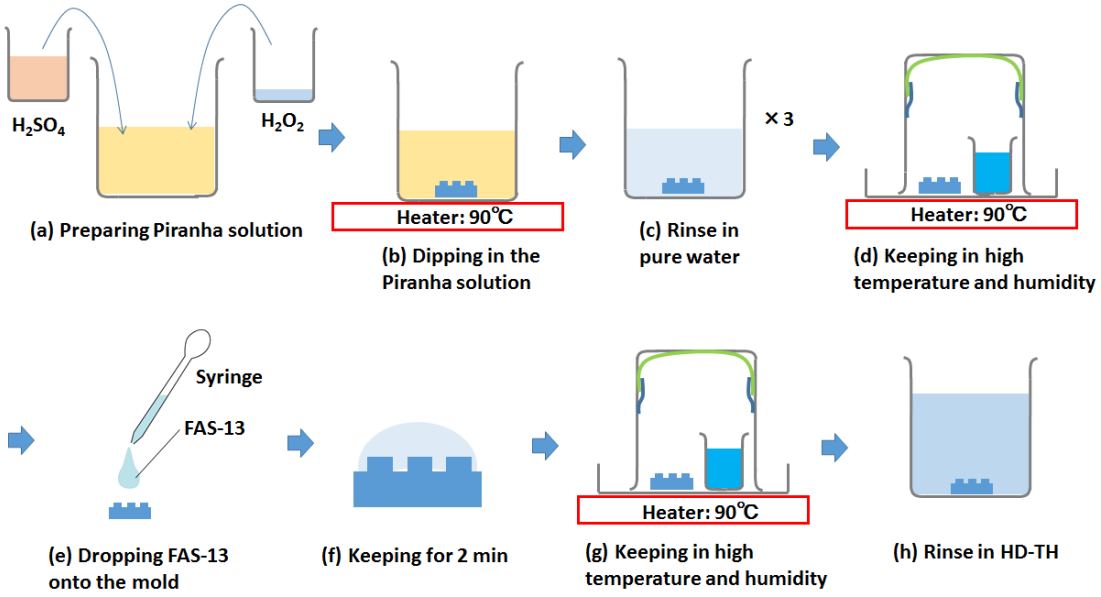

Fig. 7.4.3 The optimized process for anti-stick treatment of the mold used for the NIL with NXR-2030 resist. (a) Preparing the Piranha solution by mixing 30 ml of H_2SO_4 and 10 ml of H_2O_2. (b) Dipping the mold in the Piranha solution heated up to 90 °C for over 1 hours. (c) Rinse in the pure water for 5 min. This process should be repeated by 3 times. (d) Keeping in high temperature and humidity condition as done in Fig. A.1(a) and (c). (e) Dropping the undiluted FAS-13 onto the patterned mold surface using syringe. (f) Keeping the mold suface soaked in the droplet for 2 min. BEMCOT is useful to remove the droplet from the surface. (g) Keeping in high temperature and humidity condition for 1 hour. (d) Rinse in HD-TH solution.

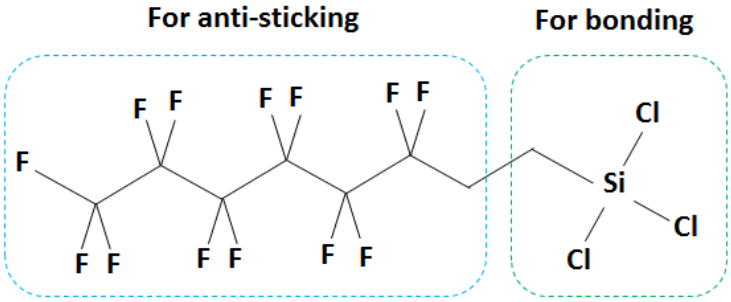

Fig. 7.4.4 Chemical structure of FAS-13. Left part is for ani-sticking function and right part is for bonding with oxide substrates.

By using the mold covered by the FAS-13 layer, I was able to obtained the nanopattern imprinted to organic resist with low destruction rate and smooth release process. Figure 7.4.5 shows the obtained pattern captured in different length scale.

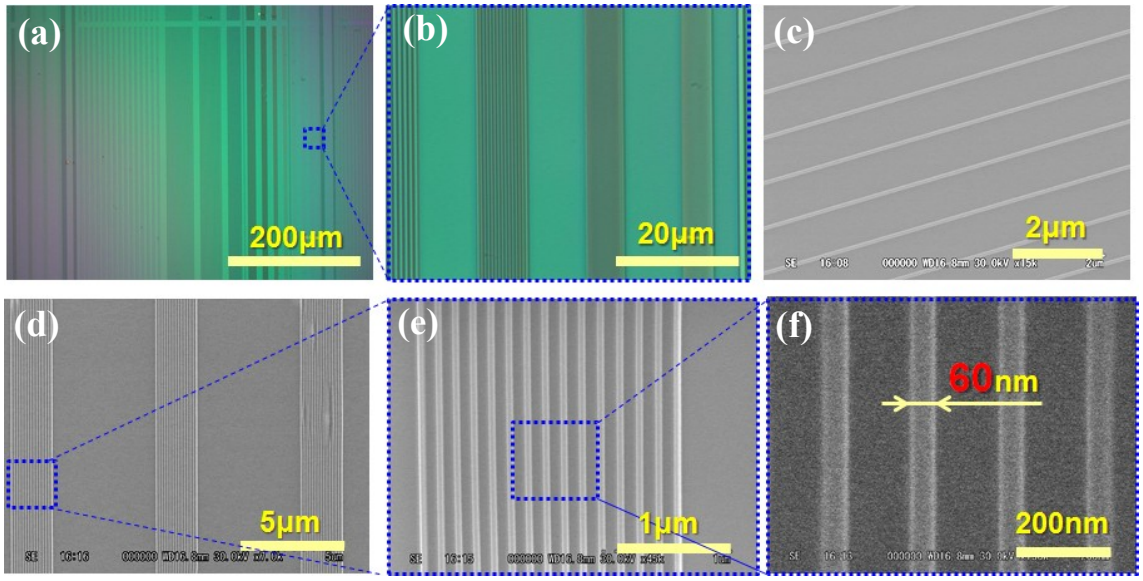

Fig. 7.4.5 Successfully nano-patterened organic resist by using the mold covered by FAS-13 layer. (a) and (b) Optical microscope image (c) – (f) SEM image.

List of publications

[Scientific Journal]

[1]* "Tuning metal-insulator transition by one dimensional alignment of giant electronic domains in artificially size-controlled epitaxial VO_2 wires"
H. Takami, K. Kawatani, H. Ueda, K. Fujiwara, T. Kanki and H. Tanaka
*Appl. Phys. Lett.***101** (2012) 263111

[2]* "Multistep metal insulator transition in VO_2 nanowires on Al_2O_3 (0001) substrates"
H. Takami, T. Kanki and H. Tanaka
Appl. Phys. Lett. **104** (2014) 023104

[3] "Metal-insulator transition with multiple micro-scaled avalanches in VO_2 thin film on TiO_2 (001) substrates"
K. Kawatani, **H. Takami**, T. Kanki and H. Tanaka
*Appl. Phys. Lett.***100** (2012) 173112

[4] "Direct observation of giant metallic domain evolution driven by electric bias in VO_2 thin films on TiO_2(001) substrate"
T. Kanki, K. Kawatani, **H. Takami** and H. Tanaka
*Appl. Phys. Lett.***101** (2012) 243118

[5] "Artificial Three Dimensional Oxide Nanostructures for High Performance Correlated Oxide Nanoelectronics"
H. Tanaka, **H. Takami**, T. Kanki, A.N. Hattori, and K. Fujiwara,
Jpn. J. Appl. Phys. **53** (2014) 05FA10

[6]* "Thermoelectric control of reversible metal-insulator transition in VO_2 nanowires"
H. Takami, T. Kanki and H. Tanaka,
submitted

[Related papers as appendix]

[A.1] “Electronic Structure of W-doped VO_2 Thin Films with Giant Metal-Insulator Transition Investigated by Hard X-ray Core-Level Photoemission Spectroscopy”
H. Takami, T. Kanki, S. Ueda, K. Kobayashi, and H. Tanaka
Appl. Phys. Express **3** (2010) 063201

[A.2] “High Temperature-Coefficient of Resistance at Room Temperature in W-doped VO_2 Thin Films on Al_2O_3 Substrate and Their Thickness Dependence”
H. Takami, K. Kawatani, T. Kanki, and H. Tanaka
Jpn. J. Appl. Phys. **50** (2011) 055804

[A.3] “Filling-controlled Mott transition in W-doped VO_2”
H. Takami, T. Kanki, S. Ueda, K. Kobayashi, and H. Tanaka
Phys. Rev. B **85** (2012) 205111

[A.4]* "Modulation of metal-insulator transition temperature in W-doped VO_2 thin films: toward Mott devices"
H. Takami, K. Kawatani, T. Kanki, S. Ueda, K. Kobayashi, and H. Tanaka
World J. Eng. **8** (2011) 1091

[A.5] "Tunable Strongly Correlated Oxide Semiconductors Revealed by Hard X-ray Photoemission Spectroscopy",
H. Tanaka, **H. Takami**, and K. Kobayashi,
SPring-8 Research Frontiers (2010) 72

[A.6] Identifying valence band structure of transient phase in VO_2 thin film by hard X-ray photoemission
T. Kanki, **H. Takami**, S. Ueda, N. Hattori, K. Hattori, H. Daimon, K. Kobayashi, and H. Tanaka
Phys. Rev. B **84** (2011) 085107

[A.7] "Coherent metallic screening in core-level photoelectron spectra for strongly correlated oxides of $La_{1-x}Ba_xMnO_3$ and $V_{1-x}W_xO_2$"
S. Ueda, **H. Takami**, T. Kanki and H. Tanaka
Phys. Rev. B **89** (2014) 035141

[International Conference]

[1] "Fabrication of epitaxial VO_2 nanostructured thin films using a nanoimprint lithography technique"
H. Takami, K. Kawatani, T. Kanki, and H. Tanaka
18th International Workshop on Oxide Electronics, Napa, the U.S.A . (September 26, 2011)

[2] "Epitaxial VO_2 Nanoline Fabricated by Using a Nanoimprint Lithography Technique"
H. Takami, K. Kawatani, T. Kanki, and H. Tanaka
7th Handai Nanoscience and Nanotechnology International Symposium, Osaka, Japan (November 10, 2011)

[3] "Dimension control of Electronic Phase Configuration Consisting of Metal-Insulator Domains in VO_2 Wires on TiO_2(001) Substrates"
H. Takami, K. Kawatani, H. Ueda, T. Kanki, and H. Tanaka
2012 Materials Research Society Fall Meeting, Boston, the U.S.A. (November 26, 2012)

[4] "Tailor-made VO_2 Nanowires on Al_2O_3 (0001) Substrates for Digitized Metal-Insulator Transition"
H. Takami, K. Kawatani, H. Ueda, K. Fujiwara, T. Kanki, H. Tanaka
2012 Materials Research Society Fall Meeting, Boston, the U.S.A. (November 28, 2012)

[5] "Investigation of digital metal-insulator transition for tailor-made VO_2 nanowires on Al_2O_3(0001) substrates"
H. Takami, K. Kawatani, H. Ueda, K. Fujiwara, T. Kanki, and H. Tanaka
The 13th Japan-Korea-Taiwan Symposium on Strongly correlated Electron Systems, Osaka, Japan (January 15, 2013)

[Domestic Conferences]

[1] “ナノインプリント法による VO_2 ナノ構造体の作製”
高見　英史, 川谷　健一, 神吉　輝夫, 田中　秀和
第 72 回応用物理学会学術講演会,山形大学,2011 年 9 月 1 日

[2] “TiO_2(001)基板上の VO_2 ワイヤーにおける金属 - 絶縁体ドメイン配列の次元性評価”
高見　英史, 川谷　健一, 上田　大貴, 神吉　輝夫, 田中　秀和
第 59 回応用物理学関係連合講演会,早稲田大学,2012 年 3 月 17 日

[3] “Al_2O_3(0001)基板上の VO_2 ナノワイヤーにおける多値金属 - 絶縁体相転移”
高見　英史, 川谷　健一, 上田大貴, 藤原　宏平, 神吉　輝夫, 田中　秀和
第 73 回応用物理学会学術講演会,　松山大学, 2012 年 9 月 12 日

[4] “VO_2 マイクロワイヤーにおける局所的金属 - 絶縁体電子相界面形成とその電気特性”
高見　英史, 神吉　輝夫, 田中　秀和
第 60 回応用物理学会春季学術講演会, 神奈川工科大学, 2013 年 3 月 29 日

[Activity]

“62nd Lindau Novel Laureate Meeting (Physics)”**,** Lindau, Germany, July 1-6 2012.

Acknowledgments

I wish to express my sincere gratitude and appreciation to Professor H. Tanaka of ISIR-Sanken, Osaka University for his continuous encouragement, supports and stimulating discussions.

I deeply express my gratitude to Dr. T. Kanki for lots of his constant encouragement, supports and helpful discussions.

I would like to thank Dr. N. G. Cha and Dr. A. N. Hattori for helpful assistance in nanofabrication process. I would like to thank Dr. K. Fujiwara for his useful suggestion and support for electrical measurements.

I would like to thank Professor S. Matsui and Dr. M. Okada in Laboratory of Advanced Science and Technology for Industry, University of Hyogo for their helpful discussion for nanoimprint lithography.

I would like to thank Dr. K. Nagashima, Dr, K. Oka to give me a helpful advice in my Ph.D work.

I thank Dr. K. Okada and all students in Tanaka Lab. In ISIR of Osaka University for encouraging me day and night. I thank Ms. T. Okumoto for her helpful assistance in office procedure. The experimental assistance of Dr. S. Sakakihara, Ms. M. Sakuma and Ms. F. Iwaki are gratefully acknowledged.

I must express my appreciation to my family for their support and understanding of my study. Finally, I would like to thank Ms. T. Shinoda, my fiancée for her continuous encouragement and affection.